Modeling, Identification, and Application of Multilayer Polypyrrole Conducting Polymer Actuators

by

Thomas W. Secord

Bachelor of Mechanical Engineering
University of Minnesota, 2005

SUBMITTED TO THE DEPARTMENT OF MECHANICAL ENGINEERING
IN PARTIAL FULFILLMENT OF THE REQUIREMENTS FOR THE DEGREE OF
MASTER OF SCIENCE IN MECHANICAL ENGINEERING

AT THE

MASSACHUSETTS INSTITUTE OF TECHNOLOGY

FEBRUARY 2007

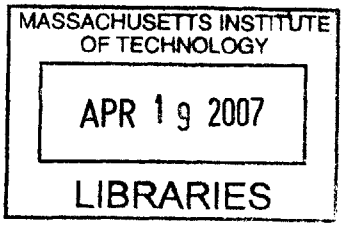

Signature of Author .....
Department of Mechanical Engineering
January 18, 2007

Certified by .....
H. Harry Asada
Ford Professor of Mechanical Engineering
Thesis Supervisor

Accepted by .....
Lallit Anand
Chairman, Department Committee on Graduate Students

Modeling, Identification, and Application of Multilayer Polypyrrole Conducting Polymer Actuators

by

Thomas W. Secord

Submitted to the Department of Mechanical Engineering
on January 18, 2004 in Partial Fulfillment of the Requirements for the
Degree of Master of Science in Mechanical Engineering

Abstract

Experiments were performed using commercially available, self-contained, multilayer polypyrrole (PPy) actuators to develop low-order lumped parameter models of actuator electrical, mechanical, and electromechanical behavior. Experimental data were processed using system identification techniques. Both grey box and black box models were identified. The grey box model consisted of a first order electrical network that was linearly and algebraically coupled to a second order viscoelastic model. The black box model incorporated a third order Box-Jenkins structure and achieved model to data residues comparable to the grey box model. When utilizing validation data, the grey box model showed very good performance for loads in the range of 0.5 to 3 N. Overall, the results of system identification experiments suggested that low order, lumped parameter models were adequate to describe the gross behavior of multilayer actuators.

An online identification scheme was developed for monitoring polymer electrical impedance and thereby monitoring the degradation state of an actuator. This identification was performed successfully using recursive least squares and least squares for a discrete impedance model. Experimental validation data, spanning more than 5 hours of continuous operation, were collected and analyzed.

A final contribution of this research was the application PPy linear actuators to a custom-designed humanoid foot. Four linear conducting polymer actuators were used to obtain multifunctional behavior of the overall foot. Jacobian analysis of stiffness and damping was performed for the design. Simulations illustrated that PPy actuators through the use of appropriate electrical excitation can modulate their stiffness characteristics as a function of time to match a desired force versus length relationship.

Thesis Supervisor: Haruhiko H. Asada
Title: Professor of Mechanical Engineering

Acknowledgements

Simply stated, the umbrella of acknowledgements covers everyone who is responsible for making me the person behind the name on this thesis. Several groups of people come to mind: teachers, professors, friends, and family. Of course, these categories are not mutually exclusive nor are they exhaustive. However, to stay within reasonable length bounds, I will limit my attention to those most central to my last year and a half of research and study.

I must profusely thank my advisor and thesis supervisor, Professor Harry Asada. First of all, thank you for taking me on as a graduate student. I am reminded every day how great an honor it is to be part of your research group. This research project was a perfect fit for me and you recognized it as such. Second, thank you for your sincere concern for all of your graduate students. The amount of time and devotion that you give to your graduate students is staggering. I think that I speak for all of your graduate students when I say that your immense knowledge of mechanical engineering research and practice give us an unrivaled role model. Thank you for your sense of humor; I think it is a rare gift. In short, thank you for helping me develop my strengths, discover my weaknesses, and overcome my limitations.

I must also acknowledge the Department of Mechanical Engineering itself. The fellowship funding I received during my first year of study was a very generous gift. I am amazed by the myriad resources available to students in the mechanical engineering department. Walking through the halls of Building 3 reaffirms my passion for engineering and for this I thank all of Course 2.

I would be remiss if I did not acknowledge the administrative staff in the Department of Mechanical Engineering at MIT. Leslie Regan is truly one in a million. Without Leslie's help, mechanical engineering graduate students would be hard pressed to fulfill departmental and institute requirements. Furthermore, completing this thesis in three regular terms would have been impossible without Leslie's help. To Leslie, and all of the mechanical engineering staff, I extend my sincere thanks.

Next, I should pay tribute to my lab-mates. Devin, you helped me to enjoy system identification and taught me how to tackle tough research problems. Manas, your comedic skills rival your electronics know-how. Kyu-jin, I hope to one day posess a modest fraction of your instrumentation and technology expertise. Binz, thank you for being a sounding board for all questions mathematical. Lael, is there anything you do not know? Josiah, I have never encountered anyone with better mechanical design intuition than yours. Levi, thanks for your patience with my naïve questions. Eric, you can always cheer me up when I am down and impart some unique wisdom in the process. Phil, you are truly an IT expert and a great engineer. Jin-Oh, when I think of academic perfection and a model of modesty, I think of you. Alex, I enjoyed our engaging discussions about control systems. Dr. Ueda, thank you for being such a patient teacher of robotics. I am constantly amazed by the depth and breadth of your knowledge. Chris, what can I say? You have been a friend in every sense of the word. You opened my eyes to so many aspects of science and technology that I will always be

in your debt. To all of you, I am proud to know such intelligent and talented people. My time in the D-Lab has been an outstanding experience.

I sincerely thank Professor Kim Stelson and Professor Sue Mantell, my undergraduate advisors at the University of Minnesota. Without their help, friendship, encouragement, and tutelage my pursuit of graduate study would have been impossible. They wrote my letters of recommendation, they taught me the do's and don'ts of technical writing, and, most importantly, they taught me that regardless of what you expect in your research, mother nature ultimately decides whether or not your conclusions are valid.

My pursuit of graduate study in engineering would not have been possible without my family. I especially thank my parents Mike and Eileen. It is they who supported me throughout all of my pursuits. As engineers, they have been my role models. As parents, they have been my constant source of pride. Without them, none of what follows would exist and I therefore dedicate much of this thesis to them. To my brother and sister I also owe a debt of gratitude. Molly and John, you have given me a sense of purpose and friendship. Thank you.

Finally, I thank my wife, Erin. She has been my rock and my confidant. Erin, you have wisdom beyond your years, beauty beyond comprehension, patience beyond saintliness, and love beyond what I thought possible of anyone. Your willingness to read and skillfully edit rough drafts of this thesis serves as a reminder of how much you truly love me. I cannot begin to express my gratitude to you in a paltry paragraph. This thesis, my work, and my heart truly belong to you now and forever.

Contents

List of Figures

List of Tables

List of Abbreviations[†]

PZT	lead zirconate titanate
SMA	shape memory alloy
CP	conducting polymer
PAN	polyacrylonitrile
PPy	polypyrrole
DEM	diffusive elastic metal
IPMC	ionomeric polymer-metal composite
PID	proportional, intregral, and derivative
PI	proportional and intregral
LVDT	linear variable differential (*or* displacement) transformer (*or* transducer)
VI	virtual instrument
DMA	dynamic mechanical analyzer
SISO	single input, single output
ARX	autoregressive with exogenous input
ARMAX	autoregressive, moving average with exogenous input
OE	output error

[†] Note that the abbreviations are listed in the order of first appearance.

BJ	Box-Jenkins
SS	state space
AIC	Akaike information criterion
LS	least squares
RLS	recursive least squares
PP	peak to peak
MTP	metatarsal-phalangeal
TM	tarsal-metatarsal

List of Symbols[‡]

$F(s)$	Laplace transform of voice coil force, N
$V(s)$	Laplace transform of voice coil voltage, V
R	voice coil or DC motor resistance, Ω
K	voice coil or DC motor back emf constant, N·m/A or V·s
L	voice coil inductance, H
$V(t)$	voltage applied to voice coil, V
$E(t)$	error from reference force to measured force in digital feedback loop, N
R_1	resistance parameter in linear electrical model, Ω
R_2	resistance parameter in linear electrical model, Ω
C	capacitance parameter in linear electrical model, F
$i(t)$, $I_s(t)$	current supplied by galvanostat and applied to polypyrrole actuator, A
α	displacement to charge ratio, mm/C
x_e	electrochemical displacement in actuator mechanical model, mm
x_m	force induced displacement in actuator mechanical model, mm
x_T	total displacement in actuator mechanical model, mm
k_1	stiffness parameter in actuator mechanical model, N/mm
k_2	stiffness parameter in actuator mechanical model, N/mm
b_1	damping parameter in actuator mechanical model, N·s/mm *or* discrete impedance pole parameter

[‡] Note that the symbols are listed in the order of first appearance.

b_2	damping parameter in actuator mechanical model, N·s/mm
$f(t)$	tensile force applied to actuator, N
τ_{creep}	time constant for creep as determined by Kelvin viscoelastic model, s
x_0	elastic actuator displacement induced from a step load, mm
F_0	magnitude of step load applied to actuator, N
$\dot{x}_{T,ss}$	steady state creep rate, mm/s
Q	polymer charge, C
x_{b1}	displacement of b_1 damping element in actuator mechanical model, mm
x_{b2}	displacement of b_2 damping element in actuator mechanical model, mm
$H_e(s)$	transfer function relating electrical input to electrochemical strain, mm/A
$H_m(s)$	transfer function relating force input to mechanical strain, mm/N
$V_{PPy}(z)$	voltage difference between actuator electrodes: z domain form, V
$V_{PPy}(s)$	voltage difference between actuator electrodes: Laplace transform, V
b_0	discrete impedance pole parameter
a	discrete impedance zero parameter
T_s	sampling period for data collection or control, s
$G_F(q,\theta)$	discrete transfer function from force to mechanical displacement
$G_I(q,\theta)$	discrete transfer function from current to electrochemical displacement
$H(q,\theta)$	discrete transfer function from white noise to colored disturbance
θ_i	parameter vector for black box models $i = 1, 2, 3$
$B_i(q)$	numerator polynomial of black box transfer function
$F_i(q)$	denominator polynomial of black box transfer function
$C(q)$	numerator polynomial of black box noise transfer function
$D(q)$	denominator polynomial of black box noise transfer function
$e(t)$	Gaussian white noise time series
$\mathcal{M}^*$	Box-Jenkins model structure
R_u	covariance of input
$\mathbf{R}_n$	covariance matrix of size n
Z	impedance, Ω *or* data set used in black box identification
$\varphi(t)$	data vector used in LS and RLS formulation
$\hat{\theta}$	parameter estimate used in LS and RLS formulation

P	covariance matrix in LS formulation
P_t, P_{t-1}	covariance matrices in RLS formulation
P_0	initial covariance matrix in RLS formulation
Φ	matrix of data vectors $[\varphi(1)\ \varphi(2)\ \ldots\ \varphi(N)]$
B	matrix incorporating measured output data in LS formulation
$y(t)$	generic measured output at each time step during an RLS identification
α_f	forgetting factor used to modify covariance update law in RLS
k	positive integer
m	positive integer
n	positive integer
ω	angular frequency of galvanostat current input, rad/s
ε	percentage weight of data point after designated time window has elapsed in RLS identification, %
δZ	impedance increment used to derate voltage saturation limits, Ω
δV_{der}	voltage saturation derating increment, V
V_{max}	initial voltage saturation limit, V
V_{sat}	derated voltage saturation limit such that $\lvert V_{max} - V_{sat} \rvert = n(\delta V_{der})$, V
$T_{recovery}$	time allotted to enable polymer voltage to return to allowable level, s
T_f	time window assigned to forgetting factor, s
J	rotor inertia in DC motor, kg·m^2
$\Theta(s)$	Laplace transform of angular displacement of rotor in DC motor, rad
$\mathbf{J}$	Jacobian matrix
$\delta\boldsymbol{\theta}$	infinitesimal displacement in joint space or actuator space, deg
$\delta\mathbf{x}$	infinitesimal displacement is Cartesian space (task space), mm
θ_A	rotation of ankle from reference configuration, deg
θ_{TM}	rotation of tarsal-metatarsal joint from reference configuration, deg
θ_{MTP}	rotation of metatarsal-phalangeal joint from reference configuration, deg
k_i	ith actuator stiffness in simplified Maxwell model, N/mm
c_i	ith actuator compliance in simplified Maxwell model ($c_i \triangleq k_i^{-1}$), N/mm
b_i	ith actuator damping in simplified Maxwell model, N·s/mm
$\mathbf{C}_x$	compliance matrix in Cartesian space

$\mathbf{C}_\ell$	compliance matrix in actuator space
$\mathbf{D}_x$	damping matrix in Cartesian space
$\mathbf{D}_\ell$	damping matrix in actuator space
$\mathbf{J}_{\ell\to\theta}$	Jacobian matrix that maps actuator velocities to joint angular velocities
$\mathbf{J}_{\theta\to x}$	Jacobian matrix that maps joint angular velocities to Cartesian velocity
ℓ_i	bone section lengths in humanoid foot, $i = 1, 2, 3$; mm
$\ell_{i,0}$	initial length of ith actuator in humanoid foot, $i =$ "*po*", "*an*", ...; mm
r_i	joint to actuator attachment radii, $i =$ "*po*", "*an*", ...; mm
β_i	reference configuration angles of the humanoid foot, $i =$ "*pf*", "*df*", ...; deg
γ_i	angles defining actuator reference configuration, $i =$ "*po*", "*an*", ...; deg
$L(s)$	Laplace transform of actuator length, mm

Chapter 1
Introduction

1.1 Engineering Actuators and Artificial Muscles

In robotics applications, direct current (DC) motors are perhaps the most versatile and widely used of all engineering actuators. They provide high angular velocity, low torque rotary motion. Therefore, in practical usage, DC motors are commonly outfitted with gear trains and other power transmission elements. From a bio-robotics perspective, DC motors are not well suited to the linear low velocity tasks that muscles and artificial muscles must provide. More specifically, mammalian skeletal muscle can provide sustainable stresses of approximately 0.1 MPa and strain rates in excess of 50 $\%s^{-1}$ [1]. These figures serve as the benchmark for artificial muscle actuators.

The term artificial muscle will be used in this document to indicate an actuator that was constructed using a smart material or smart structure and can provide a large linear strain along a single line of action and correspondingly small strains in the remaining orthogonal directions. This definition is consistent with the role of skeletal muscles in mammals. The governing physics of the smart materials that comprise artificial muscles can differ widely. In general, smart materials respond to external mechanical, thermal, electrical, or chemical stimuli. Common examples include piezoelectric ceramics (PZT), shape memory alloys (SMA), conducting polymers (CP), and chemically constricting polymers such as polyacrylonitrile (PAN).

1.2 Polypyrrole Conducting Polymers as Artificial Muscles

Artificial muscles based on polypyrrole (PPy) have shown particular promise as a biomimetic actuator. Self contained actuators have shown stress capacities in excess of 5 MPa, which is more than 10 times the stress capacity of mammalian skeletal muscles [2]-[5]. PPy actuators using large molecule electrolytes can produce large strains (>12%) and strain rates ($10\%s^{-1}$) under certain conditions [2]. Consequently, actuators using

these materials are becoming commercially available [6]. As evidenced in [2]-[6], Japanese research teams have carried out much of the development of self contained actuators. The 12-layer and 5-layer actuators available from [6] were the test specimens for the current research. A picture of a 12-layer actuator is shown in Figure 1-1. The actuator shown in Figure 1-1 provides a reasonable compromise between speed of response ($\approx$ 0.5 $\%s^{-1}$ strain rate) and force capacity ($\approx$ 3N maximum load) [6].

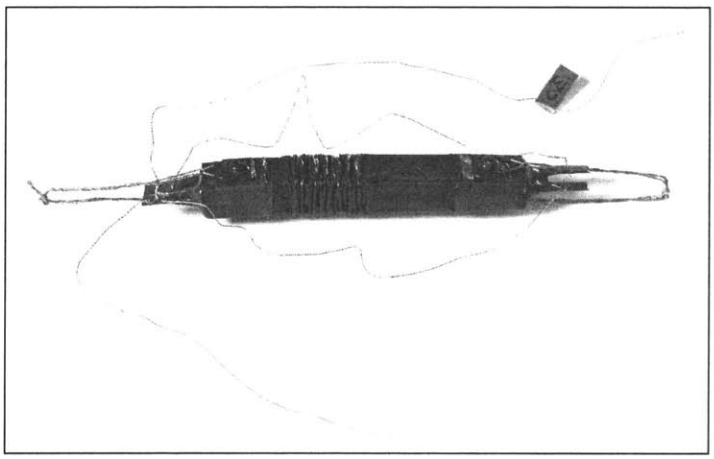

Figure 1-1: 12-Layer Polypyrrole Actuator Available from Eamex Corp. [6]

1.3 Polypyrrole Operating Principle

Polypyrrole is a moderate molecular weight polymer that possesses a conjugated backbone structure of alternating single and double covalent bonds. This structure allows for limited electron delocalization, which in turn accounts for the conductivity of PPy. Analogous to semiconductors, PPy does not possess a great deal of inherent conductivity but can be made conductive with a doping process. Unlike semiconductor doping, however, the PPy dopants do not substitute for or replace any of the polymer atoms. The actuators used in this study were polymerized onto a metallic backbone called a jabara and doped using $CF_3SO_3^-$ [3]. The jabara facilitates uniformity of the applied potential throughout the polymer and provides additional structural rigidity to each actuator layer.

As discussed in [7] and summarized in [8], when a potential is applied to a PPy conducting polymer cell, ions in an electrolyte solution move to their respective electrodes and set up two double layer capacitances. The resulting compact layer of charge on a PPy electrode drives the diffusion of ions into the polymer. The diffusion process is shown schematically in Figure 1-2.

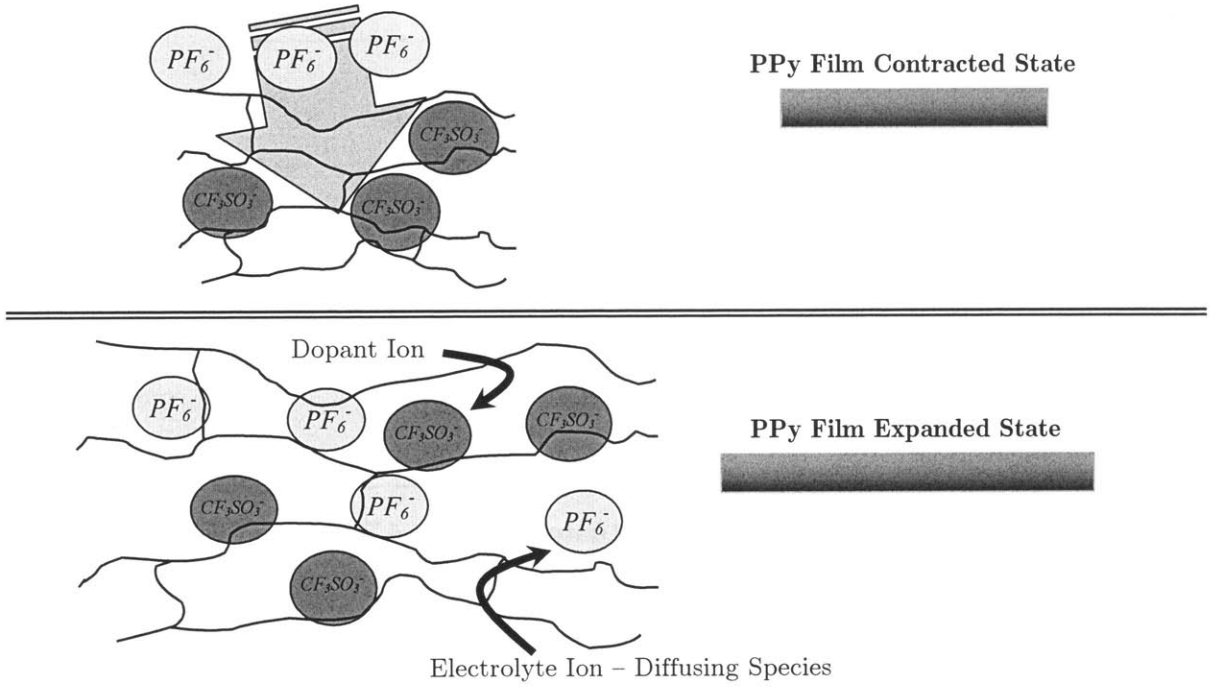

Figure 1-2: Diffusion of Electrolyte Anions into PPy Polymer Chains

When ions enter the porous polymer, the polymer increases in volume in accordance with the diffusing ion radius [7]. For a thin film this volume change manifests primarily as a length change. Also, the diffusing ion species can interact with polymer chains and cause conformational changes which lead to chain straightening. The foregoing operating principles have been successfully exploited to design artificial muscle actuators that are the subject of current research. A schematic of a mesoscale actuator electrochemical cell is shown in Figure 1-3.

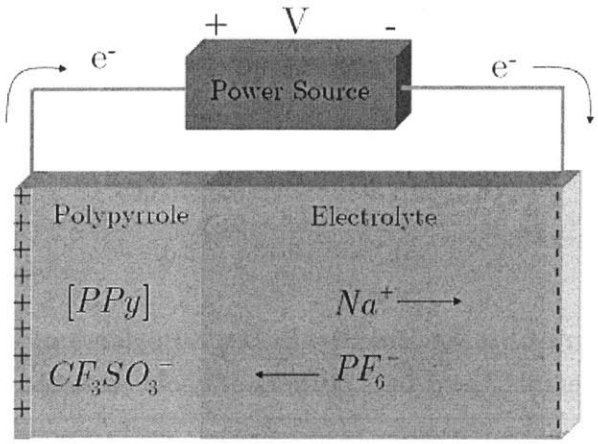

Figure 1-3: PPy Polymer Actuator Electrochemical Cell

As shown in Figures 1-2 and 1-3, when an oxidizing potential is applied to the electrochemical cell, delocalized electrons inside the polymer film tend to flow towards the cathode of the cell (the site where reduction occurs) while a charge equivalent ion flow occurs in the electrolyte. As an electron moves out of the porous polymer anode, an anion from the electrolyte enters the polymer. However, it should be noted that the flow of ions into the polymer is driven by the concentration gradient formed by the double layer capacitance at the interface of the polymer and the electrolyte and not by a need to balance charge inside the polymer [7]. The double layer capacitance, which is not shown in Figures 1-2 or 1-3, is formed quickly as a result of an applied potential.

1.4 Polypyrrole Actuator Limitations

Despite promising characteristics as actuators, the limitations of PPy artificial muscles must be addressed. The deficiencies of CP actuators based on PPy include slow speed of response, limited stroke, and susceptibility to degradation.

1.4.1 Small Strain and Strain Rate

Stroke and speed of response limitations arise from the nature of the material and the ion diffusion process by which the actuators change length. Maximal actuator bandwidth and stroke are therefore fixed performance measures for a given material and

actuator design. Table 1-1 shows a comparison of strain and strain rate capabilities for various active materials. The values listed in Table 1-1 are adapted primarily from [1] and [9], which are survey papers written by members of the Bio-Instrumentation Laboratory at MIT.

Table 1-1: Comparison of Strain and Strain Rate Performance of Various Active Materials Used in Artificial Muscle Actuators

Active Material	Strain Capability (%)	Strain Rate ($\%s^{-1}$)	Sources
Polypyrrole Ionic CP	2	1	[9]
Piezoelectric Ceramic	< 0.1	> 10	[1]
Dielectric Elastomers	20 - 380	> 100	[9]
Shape Memory Alloy	5	3	[1],[9]

Note that Table 1-1 belies the capabilities of certain actuator materials because other metrics such as lifecycle, efficiency, power density, mass density, and cost have not been considered. It is encouraging to note, however, that several actuator technologies with large strains and strain rates are being investigated as viable artificial muscles.

1.4.2 Degradation

It is suggested that permanent degradation of PPy occurs during successive electrical cycling due to nucleophilic attacks on the oxidized CP chains, thereby interrupting the conjugated backbone structure [10]. Another possible degradation mechanism includes crosslinking between adjacent oxidized CP chains thereby creating isolated islands of material that disallow ion diffusion and reduce overall actuation [10]. The most common scenario for permanent degradation occurs when potentials well above 1 V are applied to the actuator for extended periods [11]. Permanent degradation appears as an increase in PPy electrical impedance. Hence, an online method for determining impedance is a crucial to monitoring degradation. This online monitoring

provides the necessary information for preventing degradation and implementing a feedback loop.

The degradation of PPy actuator performance is more difficult to measure and quantify directly than is the small stroke and slow speed of response characteristics. Variation in actuator use leads to large variability in the actuator's lifecycle. In a standard feedback control loop designed for maximum bandwidth, an actuator is subjected to large voltage transients during a sudden change in the reference input. Large voltage inputs can also occur as a result of integrator windup during periods of non-zero steady state error. If the reference input is aggressive, the limited stroke and viscoelastic nature of PPy will quickly lead to the actuator saturating at an extreme of its force or displacement capacity. The present investigation focuses on the detection and monitoring of degradation throughout the actuator lifecycle in either open loop or closed loop control.

1.5 Literature Review

Conducting polymers have been studied extensively from a material science perspective since the mid 1970's. The materials science of PPy actuators will not be reviewed in depth as numerous researchers have laid the groundwork for understanding the nature of CP materials. The nature of their actuation and conductivity through the use of various dopants has been extensively explored. Some representative references include [3], [5], [7], and [12]. Recent materials science research has focused on optimizing the performance of PPy CP actuators as in [2] and [5]. A concise overview of the intervening history of conducting polymers is given in [13]. Recent research has focused on developing PPy as an actuator material. This research thrust can be divided into two main areas: system level modeling and control.

1.5.1 System Level Modeling

System level modeling is defined in terms of its assumptions. A typical assumption is that distributed behavior can be approximated as discrete interconnected

elements or "lumps". Furthermore, simple system level models typically assume a time invariance of system parameters and linearity of governing differential equations. These assumptions yield systems of ordinary differential equations with constant coefficients, whose couplings arise from linearizing the constitutive relations of the governing physics.

An early contribution to the system level modeling of PPy linear actuators comes from Della Santa, De Rossi, and Mazzolidi [14], who presented lumped parameter modeling using a viscoelastic mechanical model coupled with a strain generating element to reflect the actuator motion during electrical stimulation.

The work presented by John Madden, a member of the Bio-Instrumentation laboratory at MIT, represents another crucial step towards a tractable model for use in control of PPy actuators. The Diffusive Elastic Model (DEM) developed in [7] describes the continuum electrical properties of PPy in an electrolyte solution. Madden's results are presented in terms of a transcendental transfer function of admittance arising from the solution to Fick's diffusion equation. A linear constitutive equation that describes the electromechanical coupling was also proposed in [7], wherein charge is directly proportional to polymer strain. A noteworthy conclusion of Madden's continuum modeling work is that the electrical admittance of a single PPy film exhibits first order behavior over a wide band of frequencies.

Madden's modeling work was extended and clarified by Bowers [15], who formulates a linear reticulated model describing the ion diffusion process and the viscoelastic properties of PPy. Moreover, Bowers poses a quadratic constitutive relationship between charge and strain and a theory for symmetric coupling between electrical and mechanical domains. Specifically, Bowers presents a solid mechanics argument based on the approximate volumetric invariance of PPy (that is, the Poisson's ratio of $\nu \approx 0.5$). He proposes that such invariance accounts for the unidirectional nature of the electromechanical coupling between the electrical and mechanical behavior in PPy films.

1.5.2 Control

Literature surrounding the control of linear PPy actuators has been limited to single films suspended in an electrolyte solution. More generally, research of feedback control for conducting polymers has been predominantly limited to bilayer or trilayer bending actuators under a position control scheme. For example, a position feedback loop for a trilayer actuator has been implemented using CP materials for both actuation and sensing [17]. Control of linear PPy actuators has been examined by [15] and [18] with the most extensive treatment given by [15]. Bowers [15] discusses PID control for a first order plant model of the actuator and the use of adaptive control to track sinusoidal displacements. Similarly, [18] presents control of displacement based on a simple lumped electrical circuit model and online current measurements. A combined force and displacement control scheme (mechanical compliance control) has not been discussed for PPy linear actuators but has been implemented in [19] for an ionic polymer-metal composite (IPMC) bending actuator. Finally the early stages of this research devised a state-space model based controller that used estimated charge as a means for actuator protection. A description of this work can be found in [20].

1.6 Contributions

The overall contributions of the present research are lumped parameter modeling of self-contained multilayer actuators, online impedance identification, and application of PPy actuators to a humanoid foot.

1.6.1 Lumped Parameter Modeling of Multilayer Actuators

From a modeling standpoint, the present work seeks to extend the results found in [15] by using multilayer actuators rather than single films. Furthermore, a systems-level approach is used rather than using first principle partial differential equation solutions or high order reticulated approximations.

For multilayer actuators, a successful model must capture three key behaviors. First, the actuator model must account for the charge accumulation in the polymer

films as a result of applied electrical excitation. This work will use current inputs provided by a galvanostat, which departs from previous work in the field that emphasizes voltage inputs. Furthermore, a method is described for real-time identification of the electrical model. Second, the model must account for the viscoelastic behavior of the polymers in response to applied loads. The low order model used in this work places only moderate requirements on the persistent excitation of mechanical inputs and allows for numerical stiffness and damping parameters to be uniquely identified. Finally, the model must account for the coupling between the mechanical and electrical domains, which provides the constitutive relationship for the actuator. The relationship used in this work was first proposed in [7], but only for a single film actuator. This work will show that the relationship in [7] may be extended to multilayer actuators for certain ranges of electrochemical displacement.

In addition to the technique outlined above, parameters of a Box-Jenkins discrete black box model were also identified. Black box modeling is a previously undocumented approach to describing actuator behavior. Given the complex behavior of multilayer actuators, *a priori* knowledge of the governing physics does not dictate an obvious lumped parameter model. For example, even assumed viscoelastic behavior does not entail any specific model based on a spring-dashpot network. The presence of complicated physics provides suitable basis for the selection of a black box model. The enumeration of black and grey box models is addressed in Chapter 3. The data used to validate the black and grey box models were collected using the test equipment described in Chapter 2.

1.6.2 Online Impedance Identification and Degradation Prevention

It has been observed that degradation of PPy is the result of a repeated oxidative process that is exacerbated by large voltages applied to the polymer device [10]. Although the cause of degradation is known, there is a dearth of research surrounding the quantification and slowing of degradation. Thus, the current work is the first quantification of degradation through online identification of electrical model

parameters. By employing the electrical model mentioned in Section 1.6.1, recursive least squares with a forgetting factor is used to identify a discrete impedance model. Then, using Tustin's bilinear approximation, the discrete model parameters are converted to physically meaningful continuous resistance and capacitance parameters. With real-time estimates of impedance, a method is proposed for slowing the degradation of actuator performance. This method consists of de-rating voltage saturation limits based on incremental increases in impedance. In short, an increase in impedance is countered with a reduction in the allowable voltage range for the device. The complete description of impedance identification and degradation prevention is provided in Chapter 4.

1.6.3 Applications to a Humanoid Foot

To date, humanoid robotics has focused heavily on interaction with the surrounding environment through the use of high degree of freedom hands. One such hand is described in [21]. However, the role of muscle-like actuators in achieving balance and effective walking is still being developed. The article "How Animals Move", appearing in *Science* [22], adeptly summarizes the multiple functions of muscles in mammalian locomotion. As the article illustrates, muscles not only generate displacement and force but also store potential energy and dissipate energy at various times throughout locomotion. In robotics the need for such multifunctional behavior is especially apparent in humanoid and prosthetic feet. Such a need prompted the third major contribution of the present research: application of PPy actuators to a humanoid foot.

A four degree of freedom foot was designed based on simplifications of models presented in biomechanics literature (for example [23]). A model was created in SolidWorks software and then realized using a Dimension SST rapid prototyping machine. The four degree of freedom anthropomorphic foot is driven by two antagonistic pairs of PPy conducting polymer actuators. The kinematic and static analyses required to quantify the desired compliance and damping with respect to

applied ground reaction forces were also performed. Numerical simulations illustrate the main features of the design. The design and analysis of the humanoid foot can be found in Chapter 5.

1.7 References

[1] Hunter I. and Lafontaine S., "A comparison of muscle with artificial actuators", in *Tech. Dig. IEEE Solid State Sensors Actuators Workshop*, 1992, pp. 178–185.

[2] Hara S., Zama T., Takashima W., and Kaneto K., "Free-standing polypyrrole actuators with response rate of 10.8%s^{-1}", *Synthetic Metals*, Vol 149, pp. 199-201, 2005.

[3] Zama T., Hara S., Takashima W., and Kaneto K., "Comparison of Conducting Polymer Actuators Based on Polypyrrole Doped with BF_4^-, PF_6^-, $CF_3SO_3^-$, and ClO_4^-", *Bull. Chem. Soc. Jpn.*, Vol 78, pp. 506-511, 2005.

[4] Hara S., Zama T., Takashima W., and Kaneto K., "Artificial Muscles Based on Polypyrrole Actuators with Large Strain and Stress Induced Electrically", *Polymer Journal*, Vol 36, (2): pp. 151-161, 2004.

[5] Kaneto K., Nakashima M., and Takashima W., "Improvement of electrochemical deformation of conducting polymers, strain, force, and response", *Proceedings of the SPIE 11th Annual Symposium on Smart Structures and Materials: Electroactive Polymer Actuators and Devices*, Yoseph Bar-Cohen, Ed., pp. 190-198, SPIE, Bellingham WA, 2004.

[6] http://www.eamex.co.jp/denshi_hp/english/denshi_idex_e.htm.

[7] Madden J., *Conducting Polymer Actuators*, Ph.D. Thesis, MIT, Cambridge, MA, 2000.

[8] Bowers T., *Modeling, Simulation, and Control of a Polypyrrole-Based Conducting Polymer Actuator*, S.M. Thesis, MIT, Cambridge, MA, 2004.

[9] Madden J., et. al., "Artificial Muscle Technology: Physical Principles and Naval Prospects", *Journal of Oceanic Engineering*, Vol 29, (2): pp 706-728, 2004.

[10] Otero T., Marquez M., and Suarez I., "Polypyrrole: Diffusion Coefficients and Degradation by Overoxidation", *J. Phys. Chem.*, B, Vol 108, pp. 15429-15433, 2004.

[11] Madden J., Madden P., and Hunter I., "Conducting polymer actuators as engineering materials", *Proceedings of the SPIE Annual Symposium on Smart Structures and Materials: Electroactive Polymer Actuators and Devices*, Yoseph Bar-Cohen, Ed., pp. 176-177, Bellingham, WA: SPIE Press, 2002.

[12] Wallace G., et. al., *Conductive Electroactive Polymers, Intelligent Material Systems*, 2nd ed, Boca Raton, FL: CRC Press, 2003.

[13] Bar-Cohen Y., Ed., *Electro Active Polymers (EAP) as Artificial Muscles, Reality Potential and Challenges*, Bellingham, WA: SPIE Press, 2001.

[14] Della Santa A., De Rossi D., and Mazzolidi A., "Characterization and modeling of a conducting polymer muscle-like linear actuator", *Smart Materials and Structures*, Vol 6, pp. 23-24, 1997.

[15] Bowers T., Anquetil P., Hunter I., and Hogan N., "Analysis and Modeling of Electro-Mechanical Coupling in an Electroactive Polymer-Based Actuator", *Materials Research Society Symposium Proceedings*, Vol 785, D.5.6.1-D.5.6.6, 2004.

[16] Bowers T., Anquetil P., Hunter I., and Hogan N., "Analysis and Modeling of Electro-Mechanical Coupling in an Electroactive Polymer-Based Actuator", *Materials Research Society Symposium Proceedings*, Vol 785, D.5.6.1-D.5.6.6, 2004.

[17] Madden P., *Development and Modeling of Conducting Polymer Actuators and the Fabrication of a Conducting Polymer Based Feedback Loop,* Ph.D. Thesis, MIT, Cambridge, MA, 2004.

[18] Qi B., Lu W., and Mattes B., "Control System for Conducting Polymer Actuators," *Smart Structures and Materials EAPAD*, Vol 4695, pp. 359-366, 2002.

[19] Richardson R.C., et. al., "Biologically inspired control for artificial muscles", *Proceedings of the SPIE Annual Symposium on Smart Structures and Materials:*

Electroactive Polymer Actuators and Devices, Yoseph Bar-Cohen, Ed., pp. 315-322, SPIE, Bellingham WA, 2002.

[20] McCombie D., Secord T., and Asada H., "Modeling and Observer Design for Polypyrrole Conducting Polymer Actuators", *Proceedings of the IEEE / RAS-EMBS International Conference on Biomedical Robotics and Biomechatronics*, Pisa, Italy, 2006.

[21] Cho K. and Asada H., "Multi-Axis SMA Actuator Array for Driving Anthropomorphic Robot Hand", *Proceedings of the IEEE International Conference on Robotics and Automation*, Barcelona, Spain, April 2005.

[22] Dickinson M., et. al., "How Animals Move", *Science*, Vol 288, pp. 100-106, 2000.

[23] Salathe E. and Arangio G., "A Biomechanical Model of the Foot: The Role of Muscles, Tendons, and Ligaments", *Journal of Biomechanical Engineering.* Vol 122, pp. 281-287, 2000.

Chapter 2
Experimental Apparatus

2.1 Vertical Test Stand

Testing of linear polypyrrole actuators requires three components: 1) application of axial forces, 2) measurement of displacement, and 3) application of electrical excitation. The first two requirements were met using the vertical test stand described in this section and the test apparatus described in Section 2.2. The third requirement was achieved using a potentiostat-galvanostat described in Section 2.3.

A vertical test stand was constructed for preliminary isotonic experiments. This test stand is shown in Figure 2-1.

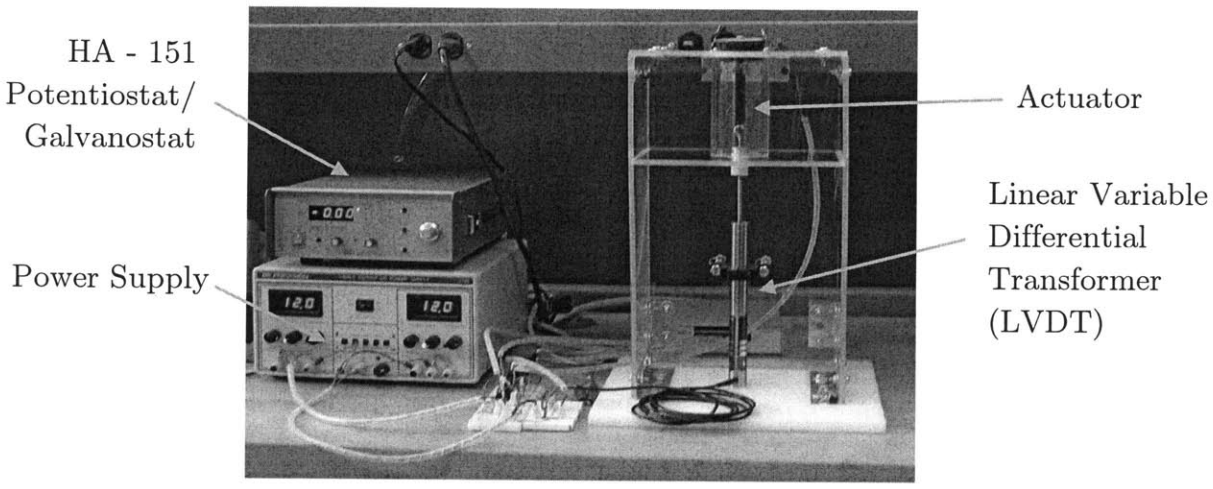

Figure 2-1: Vertical Test Stand

The test stand shown in Figure 2-1 was constructed using polycarbonate panels with steel joining inserts. The actuator resided vertically in the stand and actuation displacement measurements were taken using a RDP Group DCTH 1000 linear variable differential transformer (LVDT). Each experiment was performed using discrete weights applied to the LVDT core resulting in isotonic testing. This apparatus was primarily used to gather data pertaining to the electrical behavior of the actuators wherein time-varying mechanical loads were not needed. To gather meaningful data pertaining to the

mechanical and electromechanical behavior of the actuators, a new test apparatus was required. The new test apparatus allowed for high-speed, time-varying force application. The revised test apparatus forms the central topic in this chapter and is described in the following sections.

2.2 Development of an Actuator Dynamic Mechanical Analyzer

A dynamic mechanical analyzer (DMA) is an apparatus that is capable of applying time-varying force inputs to a material or device while simultaneously measuring the resulting displacement. The design of a DMA test apparatus was motivated by both qualitative and quantitative specifications as listed in Section 2.2.1. An overview of the design is provided in Section 2.2.2. and a description of the force control system is outlined in Section 2.2.3.

2.2.1 Performance Specifications

The key target performance specifications for the DMA are listed in Table 2-1.

Table 2-1: Target Specifications for Dynamic Mechanical Analyzer Test Apparatus

Performance Metric	Value	Units	Rationale
Force bandwidth	5	Hz	This value is above the anticipated breakpoint frequency for mechanical behavior and allows for moderate digital sampling speed during implementation.
Force Measurement Resolution	0.05	N	Measurements of force are in the range of 1-2 N and this resolution gives <2.5% precision error.
Maximum Applied Force	3	N	The actuators permanently deform under forces larger than approximately 3N.
Minimum Applied Force	0	N	Comprehensive models of the actuator mechanical behavior must include forces that approach zero.
Maximum Displacement Stroke	10	mm	The maximum actuator displacement is approximately 7 mm.
Displacement Measurement Resolution	0.05	mm	Measurements of displacement are in the range of 1-2 mm and this resolution gives <2.5% precision error.
Adjustability	High	NA	The vertical test stand did not allow for adjustability or easy use. Thus, improvement in adjustability was necessary.

2.2.2 Design Overview

Prior to construction, a solid model of the test apparatus was created in SolidWorks. The test stand solid model is shown in Figure 2-2 and the physical realization is shown in Figure 2-3.

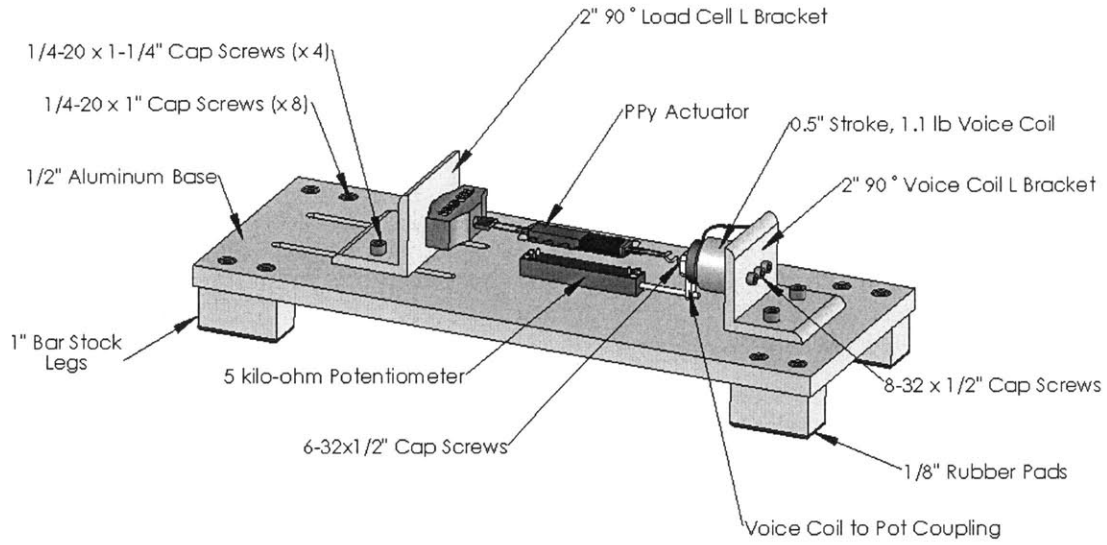

Figure 2-2: Solid Model of Experimental Test Apparatus

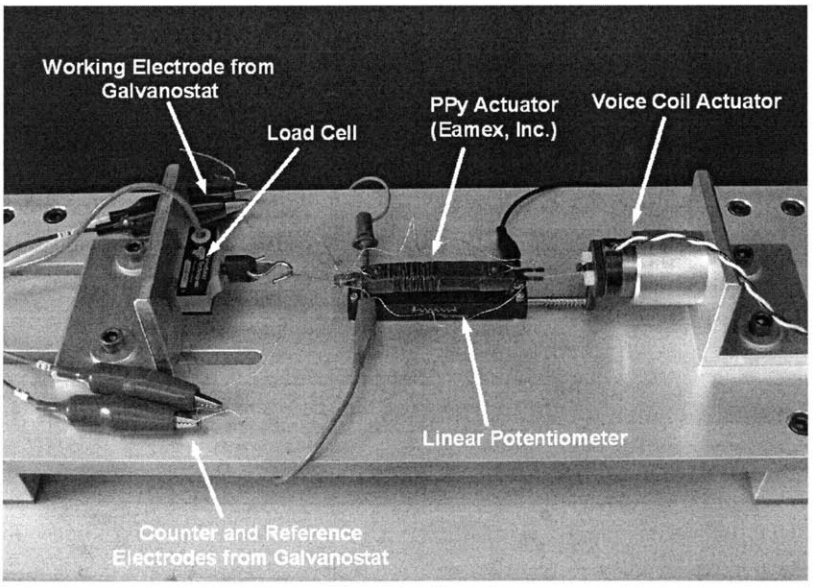

Figure 2-3: Dynamic Mechanical Analyzer Test Apparatus

The main design features of the test stand include a low profile construction, a compact footprint, and an adjustable L bracket to which the load cell is attached. Overall, the mounting of the various sensors and actuators was accomplished using threaded fasteners, two aluminum L-brackets, and the base of the test stand. All mounting screws were ANSI sizes. Most mechanical testing of PPy actuators occurred below 10 Hz and therefore the mounting was sufficiently rigid to prevent structural resonances from entering the desired closed loop frequency band.

The sensors and actuators used in the design include a voice coil actuator, a linear potentiometer, and a tension-compression load cell. Specifically, the actuator used to apply time-varying forces is a NCC05-11-011-1X voice coil made by H2W Technologies. The voice coil operates on the Loretz force principle and is capable of a maximum continuous force of 1.1 lb (4.9 N). The maximum stroke of the voice coil is 0.5 in (12.7 mm). Both the force and displacement specifications exceed the target specifications in Table 2-1, which illustrates the success of the design. Furthermore, the voice coil provides an excellent platform for feedback control of force as the Lorenz force scales linearly with current in the moving coil. The displacement of the actuator was measured by means of an ETI Systems linear potentiometer. The potentiometer supplies an analog voltage directly proportional to the absolute displacement of the wiper. The stroke of the linear potentiometer is approximately 2 in (50.8 mm). Measurements of force were obtained using a Transducer Techniques MPL-10 0 - 10 lbf (0 – 44.5 N) load cell. The load cell provides an analog voltage output proportional to the applied force. All excitation voltages were provided by a BK Precision 1760 dual rail power supply.

Following component selection and installation, the filtering and data acquisition requirements were incorporated into the design. Input and output voltages were analog in nature and therefore amenable to external filtering. The force and displacement signals were filtered using first order, low-pass, passive RC filters. The cutoff frequency of the filters was approximately 10 Hz to allow for strict filtering of unwanted high frequency noise. The first order dynamics of the force signal filter were included in the design of the feedback controller. The load cell voltage was taken directly from a full

Wheatstone bridge strain gauge circuit and was therefore differential. Following filtering, the force signal was amplified using an INA101HP instrumentation amplifier which has a high common mode rejection ratio (106 dB at 60 Hz) for the differential signal. The filtered displacement signal and the filtered and amplified force signal were acquired using a National Instruments PCI-6036 DAQ board and an IBM ThinkCentre 3.4 GHz Pentium 4 CPU running LabVIEW ™ 7.1. Selected LabVIEW virtual instruments (VIs) created during the course of this research can be found in Appendix B. The required resolution for force and displacement measurements listed in Table 2-1 was easily obtained because the NI PCI-6036 DAQ board contains 16 analog inputs which are each equipped with 16-bit analog to digital converters. Following the application of the appropriate calibration curve in LabVIEW, the resulting signal resolutions were smaller than 0.001 N and 0.003 mm for the force and displacement respectively. All data were collected by sampling the signals at 30 Hz. This sampling frequency was selected based upon the fastest anticipated time-varying signal as well as the feedback control specifications. Upon successful acquisition of the system signals, a suitable force feedback loop was designed to control the force applied to the actuator by the voice coil. The design of this control loop is addressed in the following section.

2.2.3 Feedback Control

The intended use of the DMA was to apply arbitrary time varying forces to the PPy actuator. This objective was achieved by forming a closed loop control system using the voice coil actuator and the load cell force signal. The single input – single output (SISO) design was accomplished via phase margin in the continuous frequency domain. The overall feedback loop is shown in Figure 2-4. Note that the output of the controller was applied to the voice coil using an OPA549T power operational amplifier set for unity gain. The dynamics of the amplifier and the 0-10V saturation associated with the A/D output are not included in Figure 2-4 because these effects are not relevant for the bandwidth and range of signals in the system.

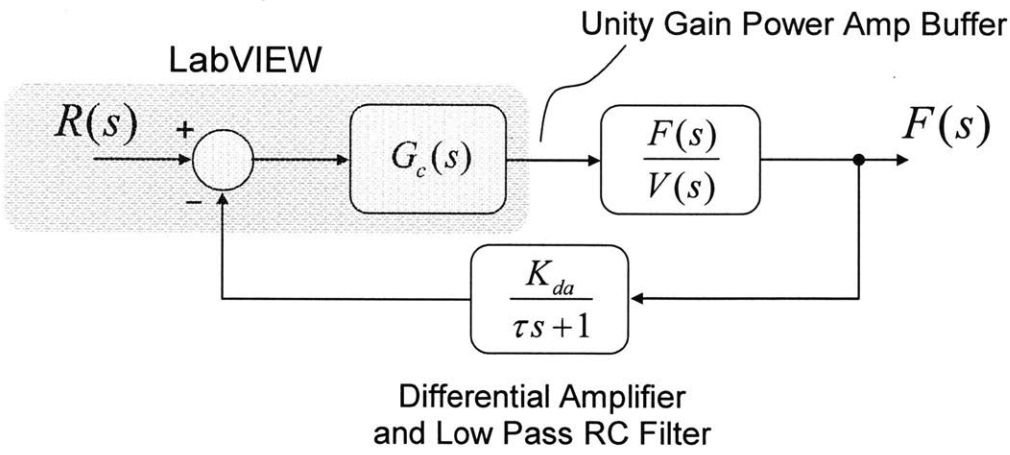

Figure 2-4: SISO Force Control Loop used in DMA

The plant model was expressed as a transfer function from applied voltage to force $F(s)/V(s)$. The relationship in the s-plane, is given in Equation 2.1.

$$\frac{F(s)}{V(s)} = \frac{K}{R + sL + \left(\frac{K^2 s(b_2 s + k_2)}{(ms^2 + k_1 + b_{vc}s)(b_2 s + k_2) + b_2 k_2 s} \right)} \tag{2.1}$$

In Equation 2.1, the main terms are the coil resistance R, the force to current constant for the voice coil K, and the coil inductance L. Notice that the term in parentheses in the denominator of Equation 2.1 arises from the back electromotive force (emf). The back emf in turn arises from the current carrying coil moving quickly in the magnetic field provided by the stator. The term in parentheses also accounts for the actuator dynamics, which are discussed in Chapter 3. After experimentally measuring the required constants, the theoretical bode plot was created. The bode plot of the loop transfer function is shown in Figure 2-5 along with the lag compensated loop transfer function. The lag pole was placed at the origin resulting in a PI controller.

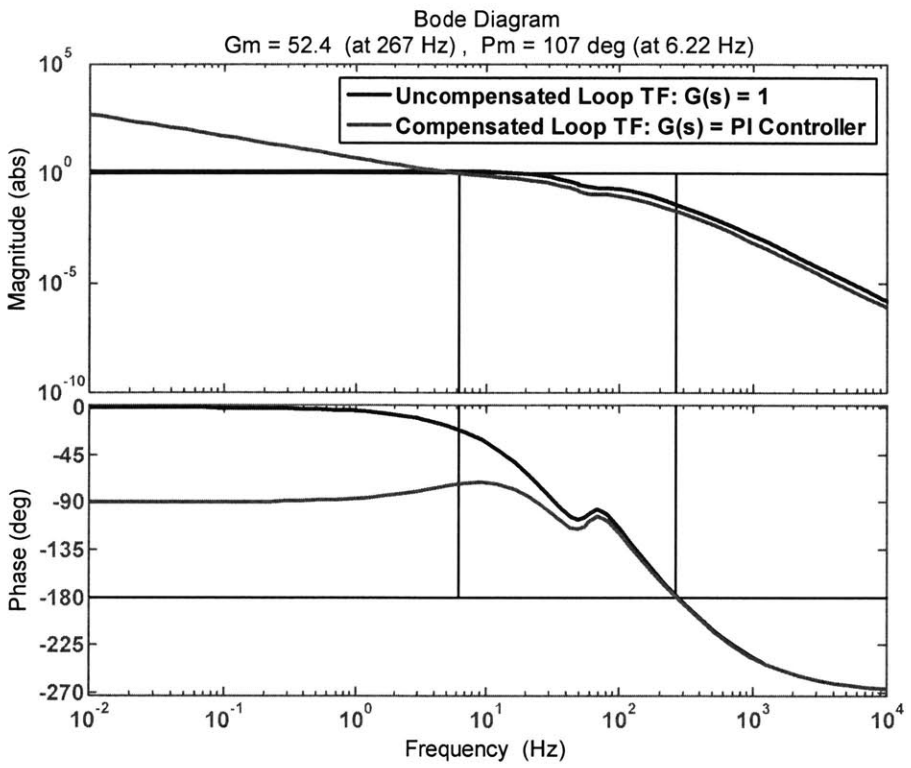

Figure 2-5: Uncompensated and Compensated Loop Transfer Functions for DMA

Notice from Figure 2-5 that the PI controller resulted in a phase margin of 107° and a crossover frequency of 6.2 Hz. This conservative design was chosen to allow for real time performance when the control loop was implemented digitally using LabVIEW. Using Tustin's approximation with a sampling period of 33 ms (corresponding to 30 Hz), the PI controller was implemented as Equation 2.2:

$$V(t) = V(t-1) + 0.66E(t) - 0.06E(t-1)\,, \tag{2.2}$$

where $E(t-1)$ is the reference force to measured force error occurring one time step prior to the current iteration and $E(t)$ is the current error. The coefficient multiplying $E(t)$ is the proportional gain and this coefficient strongly influences the closed loop performance. In Equation (2.2), $V(t-1)$ is the previously applied voltage input to the voice coil. The time series of voltage inputs were applied to the voice coil using the

digital to analog converter available on the NI PCI-6036 DAQ board as well as the unity gain buffer formed using an OPA549T power operational amplifier.

A simulated closed loop step response is shown in Figure 2-6. Note that the closed loop time constant is less than 0.1 s.

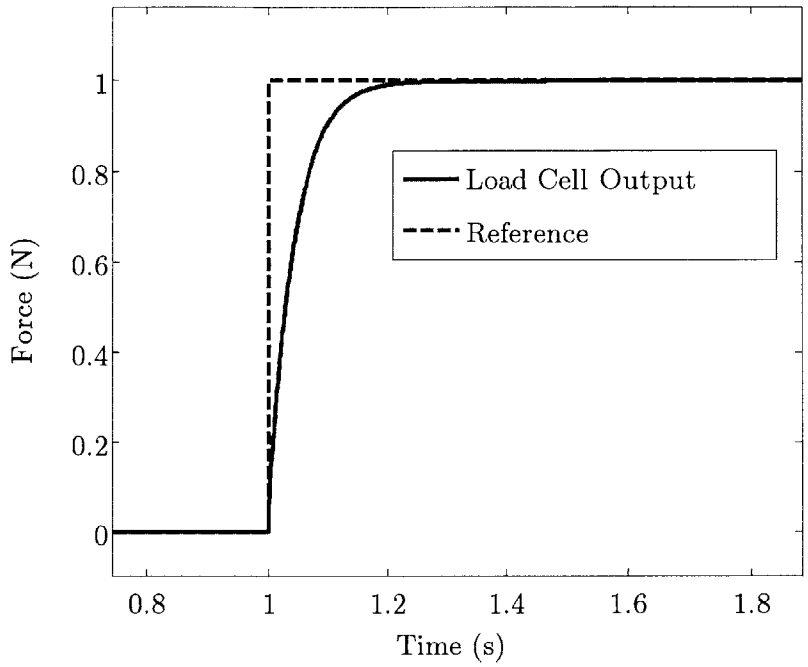

Figure 2-6: Simulated Closed Loop Step Response of PI Force Controller

Improved performance of the control system could have been achieved if an explicit real time platform were used rather than LabVIEW. However, such hardware was not available at the time of this research. For example, Quanser Inc. offers a Wireless Ethernet Embedded Control System (WEECS) unit that can fulfill data acquisition and control requirements with sampling rates in excess of 1 kHz. Alternatively, the Ardence real-time extension (RTX) for Windows provides a way to assure that high sampling rates occur in real time (that is, the sampling interval remains fixed and control computations occur within each sampling period).

2.3 Electrical Stimulation using a Potentiostat-Galvanostat

The experimental apparatus described thus far accounted only for the mechanical excitation of the PPy actuators. To fully characterize actuator behavior, electrical

excitation was also required. A combined potentiostat and galvanostat was used to apply excitation voltages and currents respectively. An Agilent 33220A function generator was connected to the HA-151 to provide the morphology of the galvanostat and potentiostat outputs. Mean-zero square waves were the most commonly used waveform.

The Hokuto Denko HA-151 potentiostat-galvanostat unit is shown in Figure 2-1. The key specifications for the HA-151 are listed in Table 2-2.

Table 2-2: Performance Specifications for HA-151 Potentiostat-Galvanostat [1]

Performance Metric	Value	Units
Maximum Current Output	$\pm$ 1.3	A
Maximum Voltage Output	$\pm$ 15	V
Speed of Response	$<$ 50	μs
Voltage Control Tolerance	3	mV
Current Control Tolerance	1	mA

As shown in Table 2-2, the HA-151 introduces a $\pm$ 1.3 A saturation non-linearity for excitation of the PPy actuator. Thus, the electrical model identified for in the following chapter, is valid only for currents below 1.3 A.

2.4 References

[1] *Operation Manual for HA-151 Potentiostat/Galvanostat*, Hokuto-Denko Corporation, 2005.

Chapter 3
Lumped Parameter Modeling of Multilayer Actuators

3.1. Development of Grey Box Model

The term grey box is used in this chapter to indicate a model structure where some knowledge of the underlying physics is used to create a linear lumped parameter model. Furthermore, the term grey box is employed because the governing equations cannot be derived from first principles and must instead be derived based on phenomenological mathematical descriptions of the actuator behavior (for example viscoelasticity). The foremost characteristics of PPy linear actuators that must be modeled are charge accumulation, material viscoelasticity, viscoplasticity, and charge induced strain. The overall lumped parameter model is shown in Figure 3-1. The associated symbols are defined in the following sections.

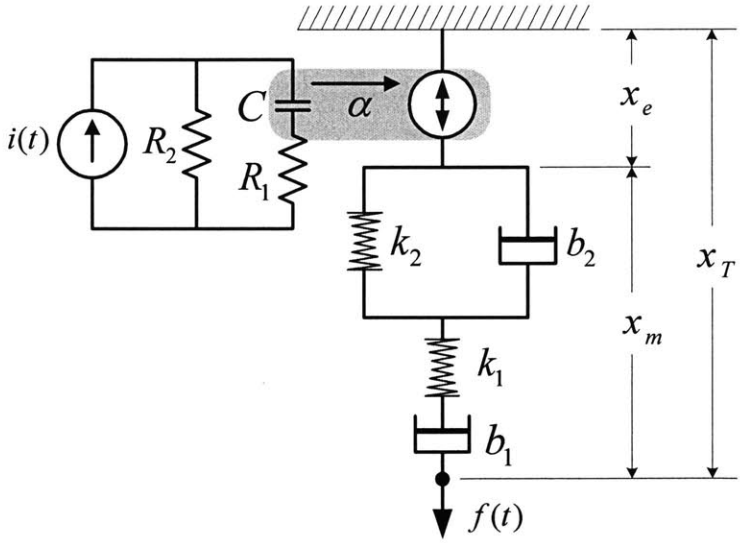

Figure 3-1: Lumped Parameter Model for PPy Linear Actuator

In establishing the grey box model, several assumptions are required. The key assumptions are as follows: 1) there is no coupling between charge accumulation and

creep, 2) the mechanical model parameters are time invariant, 3) the actuator is used only in tension, 4) the double layer charging dynamics can be neglected, 5) the charge to strain interaction is linear and unidirectional, 6) the degradation of the polymer occurs at time scales long relative to the model characteristic times, and 7) the actuator is isothermal during operation. These and other assumptions will be discussed in the following sections.

3.1.1. Charge Accumulation

Charge accumulation is modeled using the electrical circuit shown on the left-hand side of Figure 3-1. This model is similar to that found in [1] and [2]. The capacitance C represents the bulk capacitance of the PPy films. These films form both the working and reference electrodes in the PPy electrochemical cell. The resistance R_1 represents ion diffusion, contact resistance of the electrodes, and electrolyte resistance. The behavior of a single PPy film can be adequately captured for a large range of frequencies using only the R_1 and C elements [3]. Multi-layered actuators, however, exhibit additional system-level electrical behavior. The existence of leakage currents is an important experimentally observed phenomenon in the layered actuators. Current loss has been modeled by an additional resistive path characterized by R_2. Hence, the complete circuit model is as shown in Figure 3-1. Note that this circuit model neglects the small double layer capacitance which exists at the interface of the electrolyte and polymer because of its rapid charging time.

3.1.2. Mechanical Properties

Material viscoelasticity and viscoplasticity are modeled using the spring and dashpot model shown in the right-hand side of Figure 3-1. Viscoelastic and viscoplastic effects can be primarily attributed to the parallel arrangement of the polymer films. With a parallel film arrangement, the effective stiffness of an actuator scales linearly with n, where n is the number of PPy films. Other sources of stiffness and damping include the encapsulation material and the viscous electrolyte shearing. Furthermore,

the dielectic films and polymer electrodes slide past one another during actuation. This causes additional friction that can be lumped into discrete dashpot elements. In the case of multilayer encased actuators, stress and strain are not meaningful concepts because an effective cross sectional area and polymer film length are not readily available. Thus, the mechanical model is formulated in terms of the force and displacement variables. The overall mechanical displacement is given by x_m and the applied force is a specified function of time $f(t)$.

The passive behavior exhibited by PPy actuators can be represented using a Kelvin model in series with a Maxwell model as shown in the right hand side of Figure 3-1. This series combination is sometimes referred to as a Burgers fluid. The Kelvin model, which is characterized by k_2 and b_2, is used to set the time constant of the creep after a sudden load is applied. The time constant is given by

$$\tau_{creep} = \frac{b_2}{k_2}. \tag{3.1}$$

The instantaneous elongation x_0 of the polymer in response to a step load F_0 is determined by the elastic constant k_1 as

$$x_0 = \frac{F_0}{k_1}. \tag{3.2}$$

Because PPy actuators are made up of thin films, they buckle under small compressive loads. Therefore, the actuators are used only in tension. When a tensile load is removed, the actuators exhibit some plasticity which is captured by the dashpot element b_1. For a constant load and no electrical excitation, the slope of the displacement versus time curve in steady state gives the value of b_1:

$$b_1 = \frac{F_0}{\dot{x}_{T,ss}} \tag{3.3}$$

Equations 3-1 to 3-3 describe the key behaviors used in the identification of the mechanical model parameters. It is assumed that the actuator will be used at room temperature (20 – 25 °C). The isothermal assumption is important because viscoelastic

parameters are typically strong functions of temperature. It has also been suggested that a weak relationship exists between creep and charging dynamics [5], but these effects are assumed to be negligible. Overall, the mechanical model presented here extends and simplifies the mechanical models proposed by [1] and [4].

3.1.3. Electromechanical Coupling

An important aspect of the PPy actuator model is the assumption of unidirectional coupling between the electrical and mechanical domains as suggested in Figure 3-1. The unidirectional coupling assumption implies that the application of mechanical loads does not affect the electrical charging and electrochemically induced elongation. From a system identification standpoint, the assumption of unidirectional and additive coupling is essential because it allows for independent identification of the mechanical and electrical model parameters.

The electrochemical strain generated by the application of a current or voltage source to a PPy film has been shown to be linearly related to the amount of charge accumulated in the material through the charge to strain ratio [3],[4]. The linear relationship is shown in Equation 3.4, where x_e is the electrochemical displacement due to charge, α is the displacement-to-charge coefficient, and Q is the charge contained on the capacitor C:

$$x_e = \alpha Q \tag{3.4}$$

For a stress of up to 30 MPa this relationship has been shown to be relatively constant for a single film [5]. A quadratic relationship has also been posed in [1], but the present discussion will use the linear relationship and will assume a small enough working stroke to make any nonlinearity in the constitutive relationship immaterial in the parameter identification. It has been shown that the electrochemical displacement and mechanical displacement are roughly additive and independent [3]. Therefore, the electrochemical displacement generating element is in series with the remainder of the mechanical model as shown in Figure 3-1. Note again that the assumption of one way

coupling between the electrical domain and the mechanical domain allows for independent identification of the electrical parameters R_1, R_2, and C. The apparent unidirectional relationship indicates that PPy actuators do not appear to behave as gyrators or transformers, although a theory for symmetric coupling is presented in [1].

Utilizing the results from Section 3.1.1 and 3.2.2 as well as Equation 3.4, the PPy actuator's overall dynamic equations can be readily derived. The equations can be written in either state space form or transfer function form. The state space equations are amenable to numerical simulation while the transfer function form is useful for system identification purposes. The equations for a PPy actuator in state space form are given in Equation 3.5. Note that the state variables are the elongation of the damping elements. The elongation of b_1 is necessary as a state variable insofar as the total displacement is an output of the system:

$$\begin{aligned}
\frac{d}{dt}\begin{Bmatrix} Q \\ x_{b2} \\ x_{b1} \end{Bmatrix} &= \begin{pmatrix} \frac{-1}{(R_1+R_2)C} & 0 & 0 \\ 0 & \frac{-k_2}{b_2} & 0 \\ 0 & 0 & 0 \end{pmatrix}\begin{Bmatrix} Q \\ x_{b2} \\ x_{b1} \end{Bmatrix} + \begin{pmatrix} 0 & \frac{R_2}{R_1+R_2} \\ \frac{1}{b_2} & 0 \\ \frac{1}{b_1} & 0 \end{pmatrix}\begin{Bmatrix} f(t) \\ i(t) \end{Bmatrix} \\
\begin{Bmatrix} x_e \\ x_m \end{Bmatrix} &= \begin{pmatrix} \alpha & 0 & 0 \\ 0 & 1 & 1 \end{pmatrix}\begin{Bmatrix} Q \\ x_{b2} \\ x_{b1} \end{Bmatrix} + \begin{pmatrix} 0 & 0 \\ \frac{1}{k_1} & 0 \end{pmatrix}\begin{Bmatrix} f(t) \\ i(t) \end{Bmatrix}
\end{aligned} . \tag{3.5}$$

The dynamic equations in transfer function form must be written as two separate transfer functions. The first transfer function relates the electrochemical displacement x_e to the input current supplied by the galvanostat $i(t)$:

$$\frac{X_e(s)}{I(s)} = H_e(s) = \frac{\alpha R_2 C}{(R_1 + R_2)Cs + 1}. \tag{3.6}$$

The second transfer function expresses the relationship between the mechanical (that is, force-induced) displacement x_m and the external force $f(t)$ supplied by the voice coil. This transfer function is given in Equation 3.7:

$$\frac{X_m(s)}{F(s)} = H_m(s) = \frac{\frac{b_2}{k_1}s^2 + (1 + \frac{k_2}{k_1} + \frac{b_2}{b_1})s + \frac{k_2}{b_1}}{s(k_2 + b_2 s)}. \tag{3.7}$$

Thus, from Figure 3-1 and Equations 3.6 and 3.7, the overall displacement x_T is given as the linear superposition of the electrical and mechanical displacements:

$$X_T(s) = H_e(s)I(s) + H_m(s)F(s). \tag{3.8}$$

3.1.4. Parameter Identification Techniques

Identification of the continuous grey box model parameters was achieved using separate techniques for the electrical and mechanical model components. The continuous electrical model parameters were identified by first identifying the discrete equivalent to the polymer impedance as defined by the electrical circuit in Figure 3-1. A single pole single zero ARX model was used to obtain three defining parameters. The continuous impedance model is given by Equation 3.9:

$$Z(s) = \frac{V_{PPy}(s)}{I(s)} = \frac{R_1R_2Cs + R_2}{(R_1 + R_2)Cs + 1}. \tag{3.9}$$

Therefore, the discrete equivalent can be written as

$$Z(z) = \frac{V_{PPy}(z)}{I(z)} = \frac{b_0 + b_1z^{-1}}{1 + az^{-1}}. \tag{3.10}$$

Using Tustin's bilinear relationship, the continuous and discrete model parameters can be uniquely related according to Equations 3-11 to 3-13:

$$R_1 = \frac{-(b_o + b_1)(b_o - b_1)}{2(ab_o - b_1)}, \tag{3.11}$$

$$R_2 = \frac{b_o + b_1}{1 + a}, \tag{3.12}$$

and

$$C = \frac{-(ab_o - b_1)T_s}{(b_o + b_1)^2}. \tag{3.13}$$

In short, the electrical model was identified by estimating the a, b_1, and b_2 parameters[1] in Equation 3.10 using batch least squares from voltage and current time series data. The discrete parameters a, b_0, and b_1 were then converted to the continuous parameters using Equations 3.11 to 3.13.

There are certain limitations of the above technique. First, the electrical input to the actuator must be persistently exciting. However, for the low order model presented, the persistence of excitation condition is almost always met. Second, and more importantly, when the discrete circuit model is used as a one step ahead predictor its performance using validation data (that is, data taken with the intent purpose of validating a model) is excellent. However, when the corresponding continuous model is used with the same input data, a moderate disparity arises from the fact that the continuous model is equivalently an infinite step ahead predictor.

Identification of the mechanical model parameters was accomplished by fitting the appropriate time constants as described in Section 3.1.2. Step loads were applied to the polymer actuator as time response to step load inputs facilitates calculation of time constants and also validates the linearity of the response. Manual tuning of the parameters reduced model to data residues to provide excellent data fits using various actuators.

Finally, identification of the strain to charge ratio α was accomplished by first identifying the electrical model parameters. With values for the circuit model parameters, the charge residing in the bulk capacitance of the polymer films was estimated through use of the state equations (Equation 3.5). The instantaneous charge and instantaneous elongation were taken as points along the curve of the constitutive relationship given in Equation 3.4.

[1] Note that b_0 and b_1 in the discrete electrical impedance model are different than the damping parameters used in the continuous mechanical model. The distinction is intended to be clear from the context.

3.2. Black Box Modeling of Polypyrrole

For complex systems, *a priori* knowledge of system dynamics is not completely available and the governing equations cannot be described from first principles. Although single film PPy actuators in electrolyte solution are becoming well understood, multilayer actuators exhibit system level behaviors that make the above grey box modeling difficult. Therefore, black box modeling, which is more broadly called system identification, is a natural choice for creating repeatable input-output relationships for multilayer PPy actuators. In general, system identification seeks to establish the transfer function relationships between inputs and outputs for a system of interest. An overview of system identification is provided in [6].

The majority of system identification techniques have been established for discrete time series and therefore this section will deal only with identification of discrete model parameters. Several possible black box model structures exist for describing the behavior of PPy actuators; each model structure differs based on its assumptions about the dynamics between input to output and noise to output (for example ARX, ARMAX, OE). The general Box-Jenkins (BJ) model structure provided the best prediction capabilities for PPy linear actuators. A Box-Jenkins structure assumes completely independent dynamics for the input-output transfer functions (both electrical and mechanical) and the noise-output transfer function. This finding agrees with the grey box modeling outlined in the previous section.

3.2.1. Box-Jenkins Model Structure

From the assumed independence of the electrically driven displacement and mechanical viscoelastic response, a PPy actuator can be modeled as shown in Figure 3-2. Note the addition of a Gaussian white noise disturbance $e(t)$. Upon filtering through the discrete transfer function H, the noise becomes a colored disturbance $v(t)$. The additional $v(t)$ term will account for unmodeled nonlinearities, cross couplings, etc.

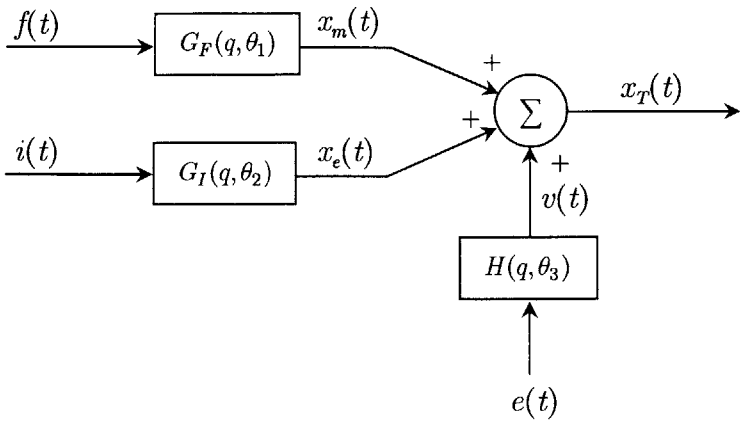

Figure 3-2: Model Structure Assumed for Black Box Identification

In Figure 3-2, the force and current are filtered through discrete transfer functions $G_F(q, \theta_1)$ and $G_I(q, \theta_1)$. The designations $G_F(q, \theta_1)$ and $G_I(q, \theta_1)$ are used to differentiate these transfer functions from their continuous analogs in Equations 3.6 and 3.7. Following the notation in [6], q is a forward time shift operator and θ denotes a parameter vector. In the case of the Box-Jenkins model, the parameter vectors contain unknown constants that specify the locations of the poles and zeros of the transfer functions in the z-plane.

The modeling in Sections 3.1 suggests that G_F and G_I will have different characteristic roots. Furthermore, experimental data shows that the viscoelastic response is not completely symmetric because it is assumed that the unmodeled nature of the asymmetric mechanical response enters late in the process with relatively independent dynamics. In addition, the experimental method for changing applied force requires moving hanging weights as described in Section 2.1 and such movement can be treated as a measurement error. Hence, the current black box model will be parametrized in the general two-input Box-Jenkins form.

3.2.2. Parameter Identification Techniques

The System Identification Toolbox in Matlab was used to compare the variants of the Box-Jenkins model, including ARX, ARMAX, and OE. A state space (SS) model was also identified and its prediction capabilities were compared with the discrete

transfer function models. For the Box-Jenkins structure, the complete parametrization consists of 6 polynomials, the orders of which are free choices that can be selected based on intuition and desired model accuracy.

In short, it was assumed that the total displacement was given by

$$x_T(t) = \frac{B_1(q)}{F_1(q)} f(t) + \frac{B_2(q)}{F_2(q)} i(t) + \frac{C(q)}{D(q)} e(t)\,, \tag{3.14}$$

or, substituting the appropriate transfer function symbols,

$$x_T(t) = G_F(q,\theta_1) f(t) + G_I(q,\theta_2) i(t) + H(q,\theta_3) e(t)\,. \tag{3.15}$$

The model structure in Equation 3.15 and shown in Figure 3-2 will be denoted as $\mathcal{M}^*$.

3.3. Experimental Results

Several experiments were conducted to discover, revise, and validate the models described in Sections 3.1 and 3.2. The experimental data were taken using apparatuses described in Chapter 2. Most of the data for the grey box models were taken using the apparatus described in Section 2.2, while the black box data were taken with the apparatus described in Section 2.1. In all cases, Matlab was used to perform relevant data analysis and plotting. The associated M-files can be found in Appendix A.

3.3.1. Grey Box Results

The data used in establishing the grey box model can be broken down into three main areas. First, data were collected to ascertain the electrical characteristics of the actuator and to validate the unidirectional coupling assumption. Second, data were collected to describe the viscoelastic-viscoplastic response of the actuator to applied loads. Finally, data were collected to establish a value for the strain to charge coupling coefficient.

The experiment performed to confirm the unidirectional coupling between the electrical and mechanical domains was performed as follows. First a 200 g load was

applied to a 5-layer actuator mounted in the vertical test stand described in Section 2.1. The displacement of the actuator was allowed to equilibrate to a steady state value. The displacement measured by the LVDT was then zeroed electronically using LabVIEW. Upon zeroing of the displacement, the actuator was charged for approximately 6 s with a 0.5 A square wave provided by the galvanostat. Following the charging, the 200 g was released. This voltage, current, and displacement data collected during this experiment are shown in Figure 3-3.

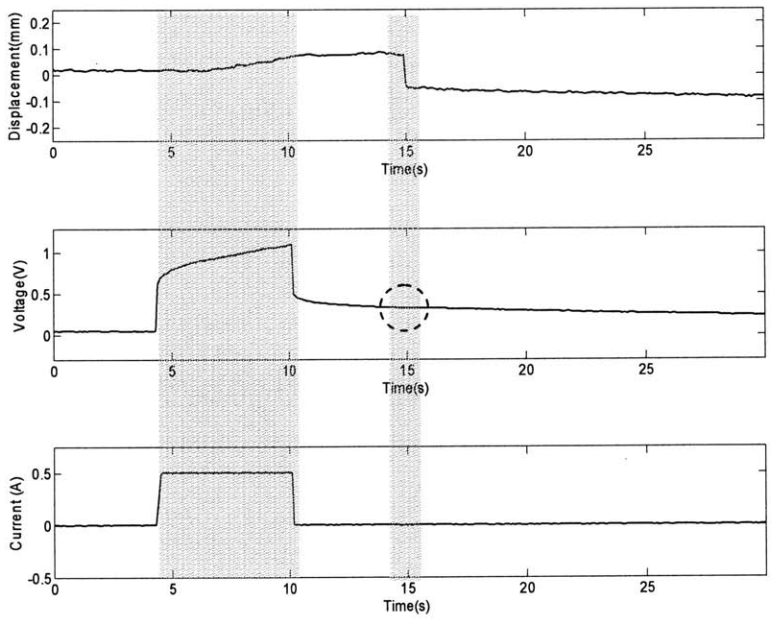

Figure 3-3: Current, Voltage, and Displacement versus Time for Unidirectional Coupling Experiment

As indicated by the dashed circle in Figure 3-3, the absence of any change in the voltage waveform upon the sudden release of the 200 g mass serves as a confirmation that changes in mechanical loading are not accompanied by changes in the polymer charge and electrochemically induced displacement.

The identification of the circuit model shown in the left hand side of Figure 3-1 was performed for a 12-layer actuator using an applied current waveform and measured voltage output. Both current and voltage measurements were performed using the HA-151 potentiostat and galvanostat unit. The parameter identification experiments utilized

$\pm$0.9A current square waves of different frequencies to provide different amounts of charge in the polymer. Specifically, 0.2 Hz, 0.15 Hz, and 0.1 Hz were used in data sets 1, 2, and 3 respectively. The 0.2 Hz data set, which is representative of the three data sets, is shown in Figure 3-4. The batch least squares (LS) results of the discrete and continuous impedance parameter identification are summarized in Table 3-1. Note that Equations 3.11 to 3.13 were used to convert the discrete parameters to the continuous parameters. The results are summarized in Table 3-1.

Table 3-1: Discrete and Continuous Impedance Parameters from Equations 3.9 and 3.10

Data Set	b_o	b_1	a	R_1 (Ω)	R_2 (Ω)	C (F)
1	0.3970	-0.3632	-0.9869	0.45	2.58	2.50
2	0.3648	-0.3321	-0.9839	0.43	2.02	2.51
3	0.3706	-0.3430	-0.9887	0.42	2.45	3.1
Means	0.377	-0.346	-0.987	0.43	2.35	2.70
Std. Dev.	0.017	0.016	0.002	0.015	0.293	0.344

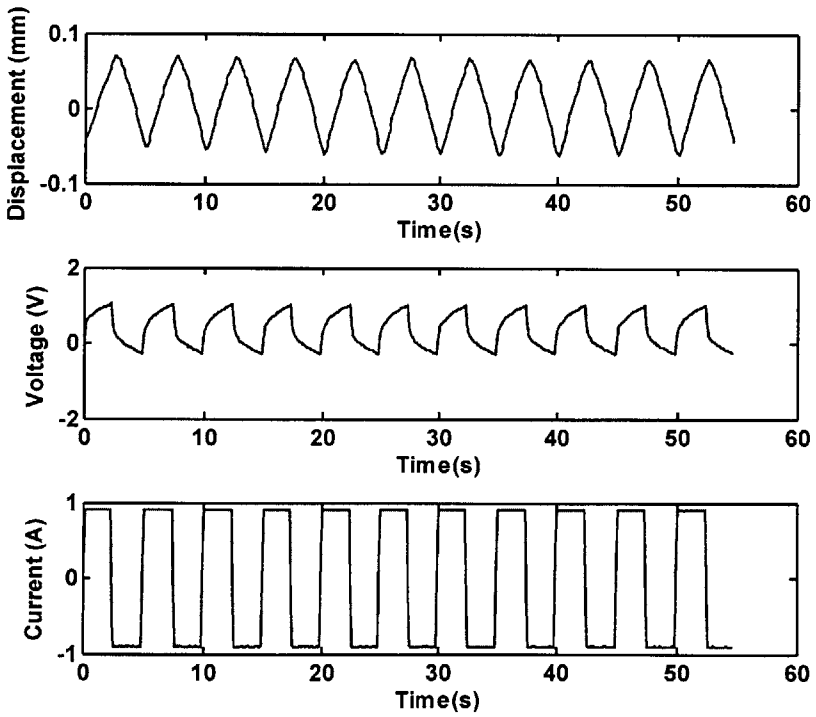

Figure 3-4: Current, Voltage, and Displacement Data (0.2 Hz) Used in Identification

For all LS estimates of the discrete impedance parameters, the variance and covariance was less than 0.03. On average, the PPy actuator behaved as a very large capacitive load with small series and parallel resistances. The time constant for charging, as taken from the denominator Equation 3-6, is approximately 7.5 s.

In a separate experiment, data were taken using a 5 layer actuator subjected to a 1.2 A current square wave at 0.1 Hz. The actuator was loaded isotonically using a 150 g mass. The electrical circuit parameters measured using least squares were $R_1 = 1.32$ Ω, $R_2 = 2.72$ Ω, and $C = 0.46$ F. The current input and voltage output are shown in Figure 3-5. Note that the plot of voltage versus time contains both the measured and the predicted output using the `lsim` function in Matlab. The predicted output coincides extremely well with the measured voltage.

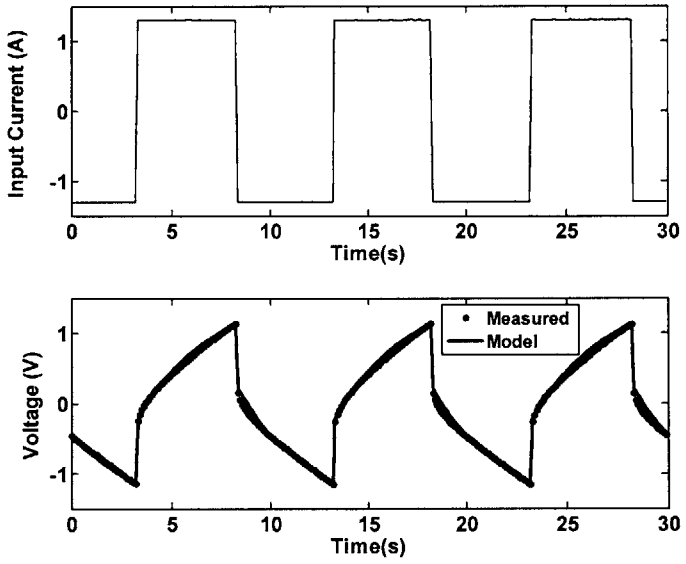

Figure 3-5: Measured and Predicted Voltage Output for a 5-layer Actuator Subjected to 150 g Loading and 1.2 A Current Square Wave

The second set of grey box modeling data describes the mechanical behavior of the PPy actuators to various applied loads. The data presented here were taken using the test apparatus described in Section 3.2. Shown in Figures 3-6 through 3-8 are data taken by applying incremental square waves ranging from 0.5 N to 2.75 N to three

separate 12-layer actuators. A 0.25 N force increment was used. Note that a bias load of 0.5 N was used to remove the catenary associated with the actuator residing in the horizontal test apparatus. For all of the mechanical testing experiments, the actuator displacements were the result of applied forces only because the actuators were not subjected to any electrical excitation.

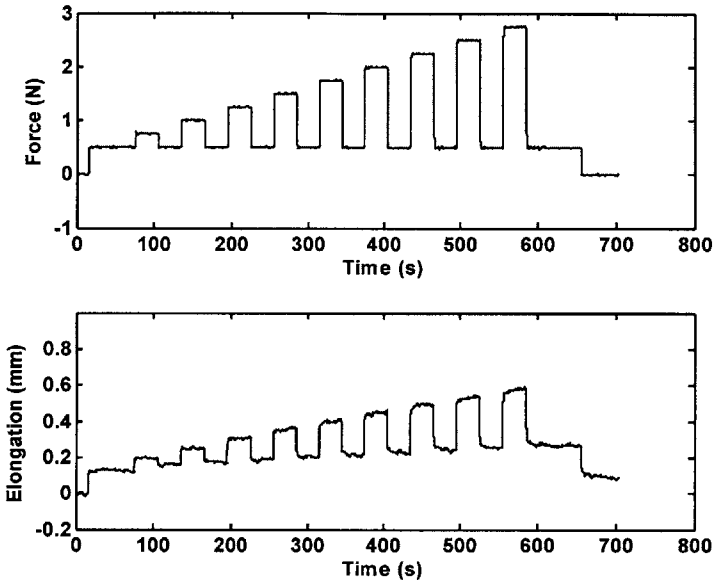

Figure 3-6: Applied Forces and Resulting Displacement for 12-Layer Actuator 106

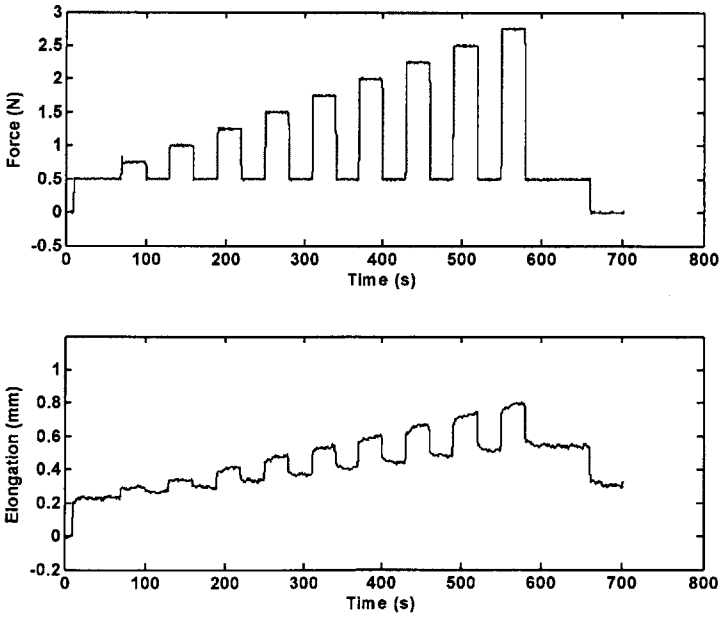

Figure 3-7: Applied Forces and Resulting Displacement for 12-Layer Actuator 114

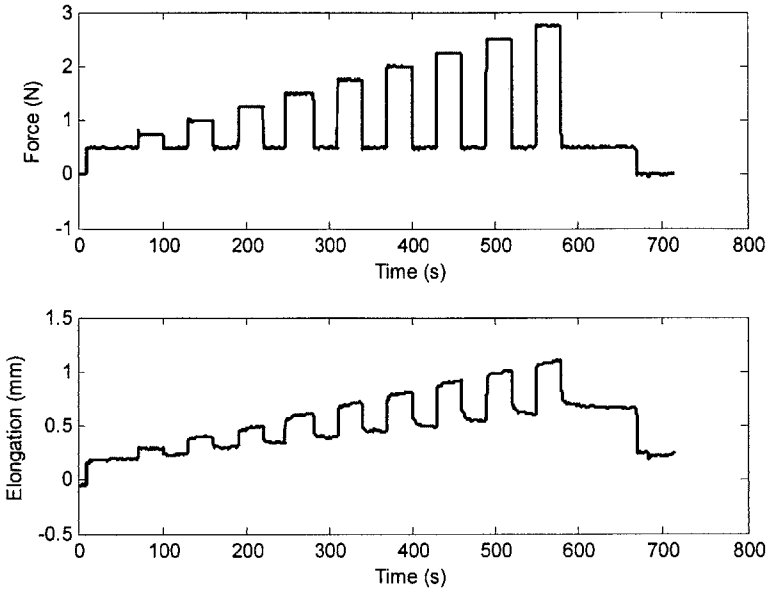

Figure 3-8: Applied Forces and Resulting Displacement for 12-Layer Actuator 108

Note that the data shown in Figures 3-6 to 3-8 have the same salient features. Specifically, the displacement versus time plot shows features indicative of viscoelastic behavior. In terms of the poles of the transfer function in Equation 3-7, it is apparent that the characteristic roots reside on the real axis in the s-plane as predicted by the model. Another notable feature is the presence of the viscoplastic behavior. When the final applied load was removed, there was a fraction of the displacement (approximately 0.2 mm) that remained. Data shown in [1] suggest similar qualitative behavior in single PPy films. Since the actuators are used in tension only (and the model is valid only in tension), the presence of a pole at $s = 0$ in Equation 3.7 accounts for the viscoplastic behavior. The viscoplasticity of the mechanical model shown in Figure 3-1 is an attractive feature. Other viscoelastic models, such as the standard linear solid, do not capture plasticity effects.

Using the data shown in Figure 3-6, the parameters of the mechanical model were obtained by fitting the relationships in Equations 3.1 to 3.3. Manual tuning was performed to improve the overall fit between model and data. Using the numerical values for the mechanical model parameters and the `lsim` function in Matlab, the force input data were applied to the mechanical model. The resulting output is shown in Figure 3-9. The solid

line plot of displacement versus time in Figure 3-9 was created using $k_1 = 6300$ N/mm, $b_1 = 1.7\times10^6$ N·s/mm, and $k_2 = 1.0\times10^4$ N/mm, and $b_2 = 2.0\times10^6$ N·s/mm.

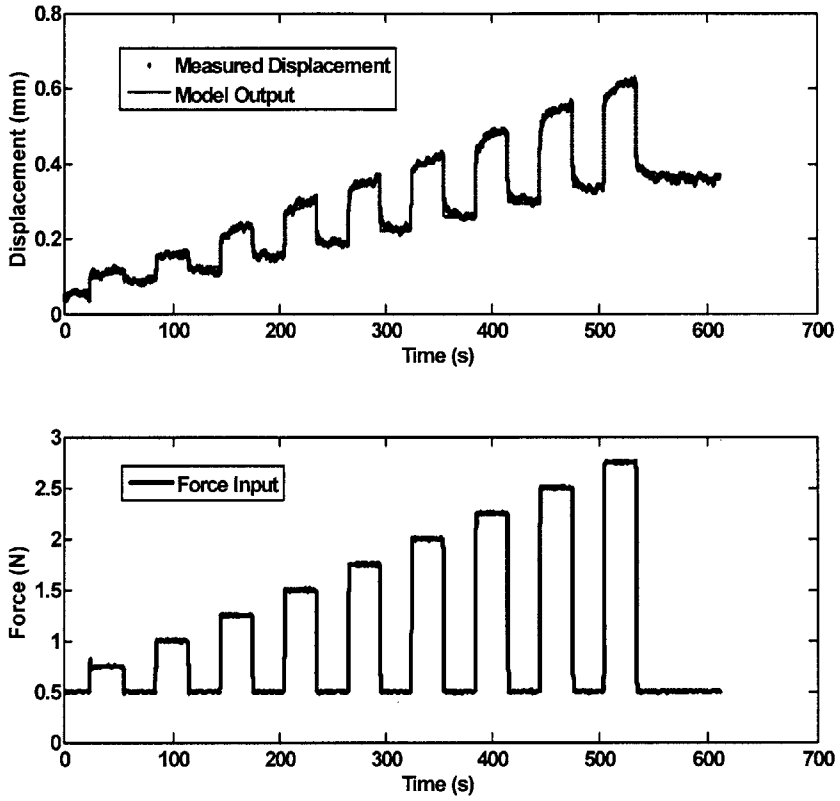

Figure 3-9: Measured and Model Output for Actuator under Time Varying Mechanical Loading

The final set of data collected for grey box modeling is data containing both mechanical and electrical excitation. Displacement, current, and voltage data were collected for a 12-layer actuator under 200 g isotonic loading. These data were used to quantify the charge to displacement constitutive relationship. Using the identified R_1, R_2, and C values from Table 3-1, charge on the capacitor was computed for a given current input. The estimated charge, combined with measurements of x_T, gave plots of the constitutive relationship at the various frequencies[2]. Figures 3-10 and 3-11 show the

[2] Note that after the load was applied to the actuator, the viscoelastic displacement was allowed to reach a steady state value. The mechanical displacement was assumed to be quasi-stationary throughout the experiment and thus $x_T \approx x_e$.

constitutive relationship for 0.2 Hz and 0.1 Hz respectively. Note that a linear least squares fit was used to obtain a relationship with and without forced zero crossing. Figure 3-11 shows morphology suggesting saturation, which was not unexpected. This electrochemical displacement saturation occurs when the voltage within the material reaches that of the ion double layer. One significant feature of both Figure 3-11 and Figure 3-12 is the presence of a hysteresis loop. The hysteresis loop suggests a time lag between the application of current and the conversion to a mechanical displacement. For simplicity, the model of the constitutive relationship will be assumed to remain linear. However, the model structure discussed in the next section will account for time lags between the electrical input and mechanical output. For the linear behavior in Figure 3-10, the average slope of the charge versus displacement curves was $\alpha = 0.068$ mm/C.

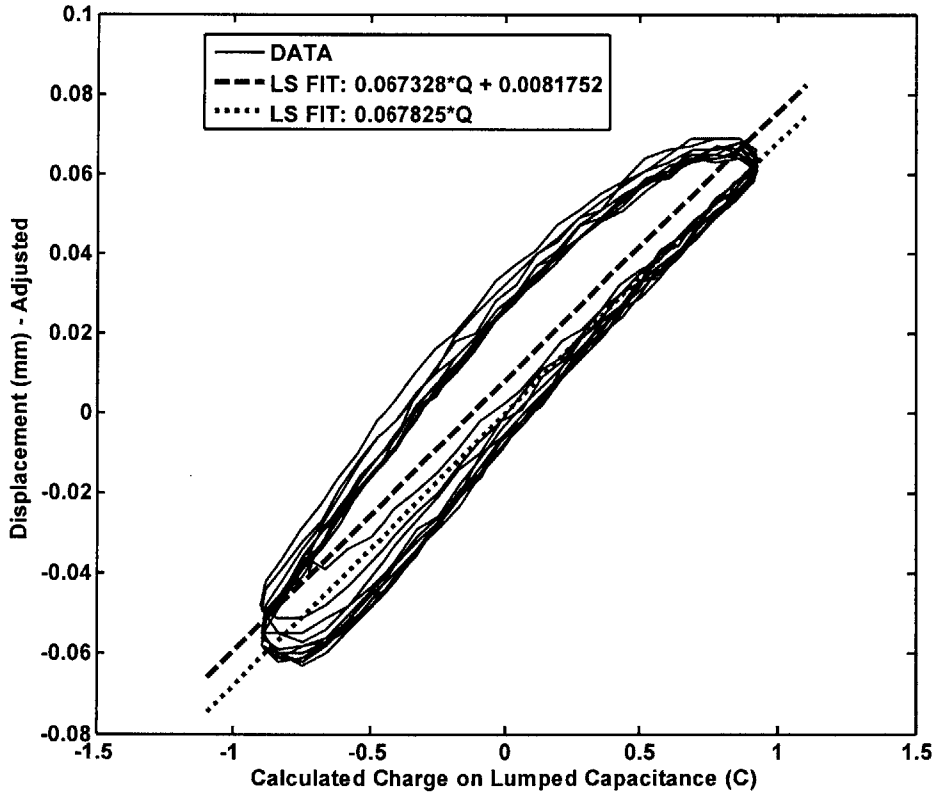

Figure 3-10: Charge Versus Displacement for 0.2 Hz Input Current Square Wave

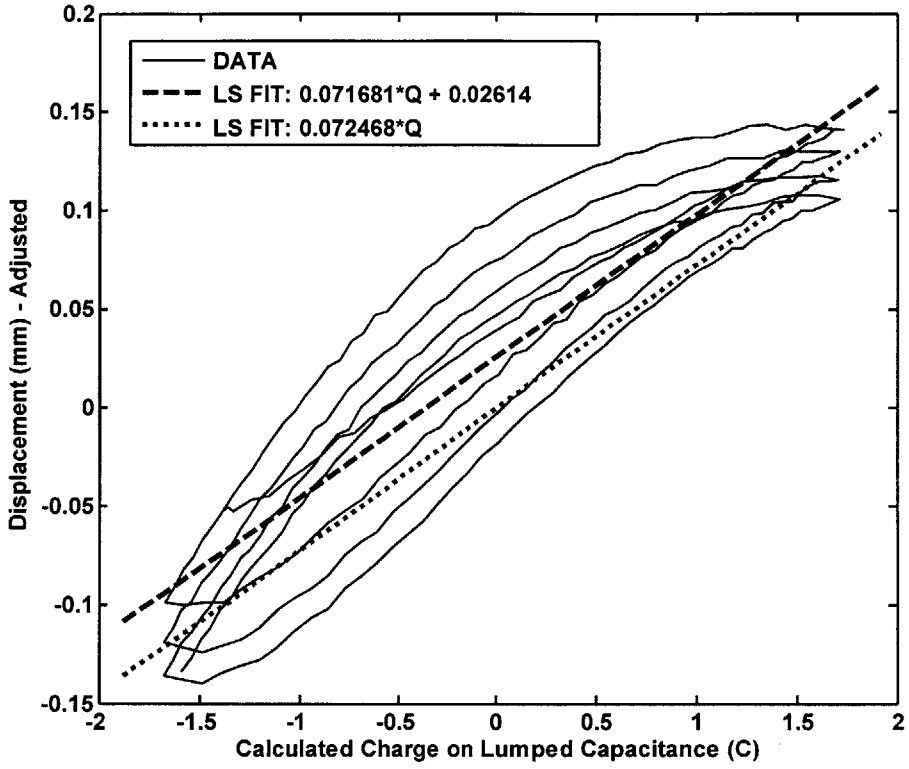

Figure 3-11: Charge Versus Displacement for 0.1 Hz Input Current Square Wave

3.3.2. Black Box Results

Now the identification of the black box model structure $\mathcal{M}^*$ will be addressed. The input-output data set Z for identifying parameters within this model structure is shown in Figure 3-12. Note that the output is taken to be the displacement and the inputs are taken to be force and current. Similar data were obtained with the same actuator 2 hours after the initial data were collected. The second data set was used for model validation.

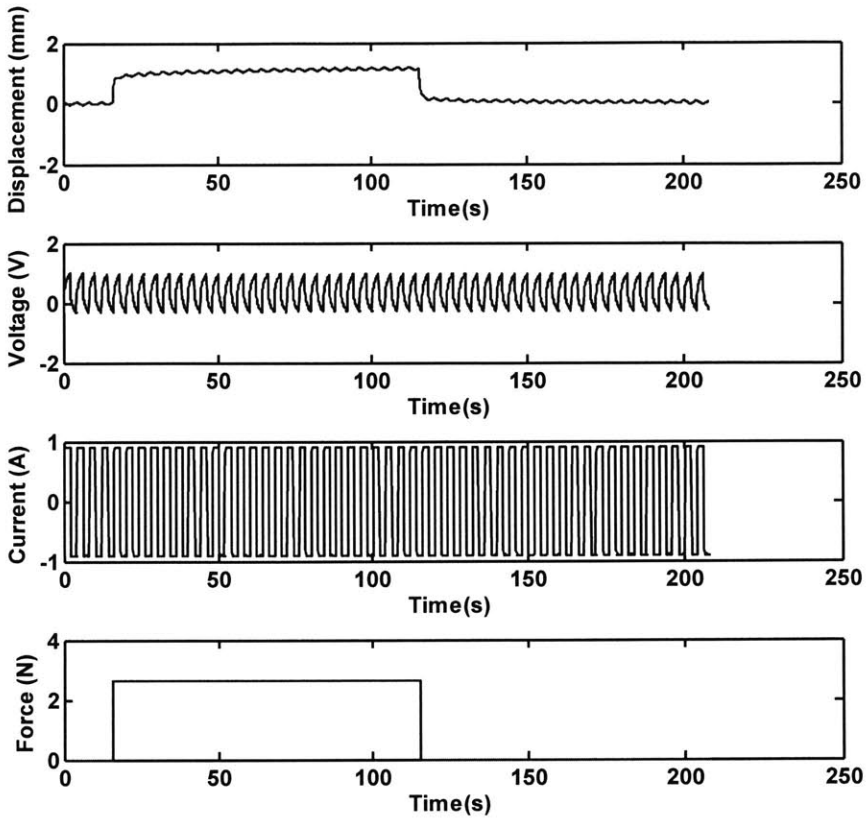

Figure 3-12: Data Used for Identification of Models Within $\mathcal{M}^*$

The levels of persistent excitation were found to be of order 15 for the step force input and 20 for the current square wave input. These levels of persistent excitation were computed using `pexcit` with a 0.01 cutoff for the singular values of the input autocorrelation matrix $\mathbf{R}_n$:

$$\mathbf{R}_n = \begin{pmatrix} R_u(0) & R_u(1) & \dots & R_u(n-1) \\ R_u(1) & R_u(0) & \dots & R_u(n-2) \\ \vdots & \vdots & \ddots & \vdots \\ R_u(n-1) & R_u(n-2) & \dots & R_u(0) \end{pmatrix} \tag{3.16}$$

where, for example, $R_u(1)$, is given by $E[u(t = T_s)u(t = 0)]$ with E as the expectation operator and T_s as the sampling period.

Using the System Identification Toolbox, the order within each model type (for example ARX, ARMAX, etc.) was manually varied until the numerical value of Akaike

Information Criterion (AIC) was minimized for that model type. The overall results are shown in Table 3-2:

Table 3-2: Summary of Black Box PPy Actuator Modeling Using Current Control and Force Inputs

Model Type	% Fit ID Data	% Fit Validation Data	AIC	Mechanical Model Order	Electrical Model Order	Noise Model Order
ARX	86.8	80.1	-9.5	3	3	0
ARMAX	75.0	58.7	-9.2	3	3	0
OE	95.8	92.9	-7.6	3	3	0
SS	92.8	86.4	-9.7	6		Constant
BJ ($\mathcal{M}^*$)	**94.3**	**90.1**	**-9.5**	**3**	**3**	**3**

Note that the two-input BJ model performs the best overall of all the model choices. Hence, the assertions of the grey box modeling, namely independent electrical and mechanical dynamics, are confirmed indirectly using the black box modeling approach. Note, however, that the independent dynamics of the noise are a necessary element to the success of the BJ model. The final BJ results are shown in Figures 3-13 and 3-14 for the identification data and validation data respectively:

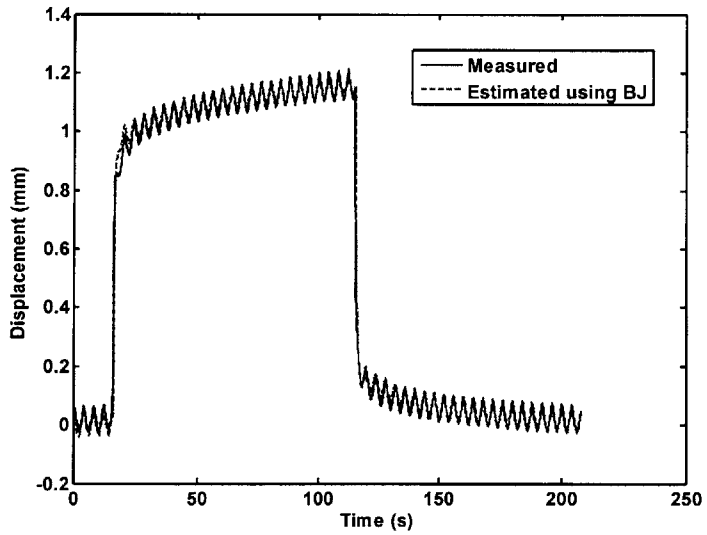

Figure 3-13: Identification Displacement Data – 3rd Order BJ Structure

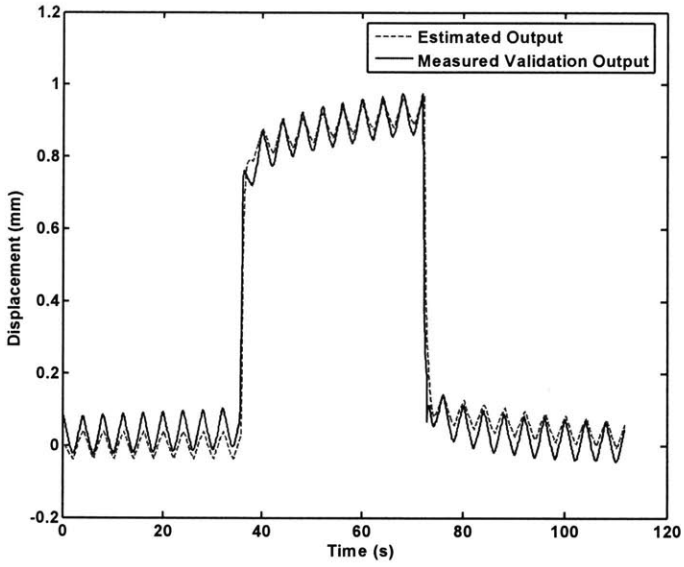

Figure 3-14: Validation Displacement Data – 3rd Order BJ Structure

A plot of the residuals for prediction is shown in Figure 3-15. The units of the ordinate are mm while the units of the abscissa are s. Note that the prediction error appears as Gaussian white noise except at the mechanical loading transitions, these spikes in estimation error may arise because of the slight time delay between applied force and displacement response.

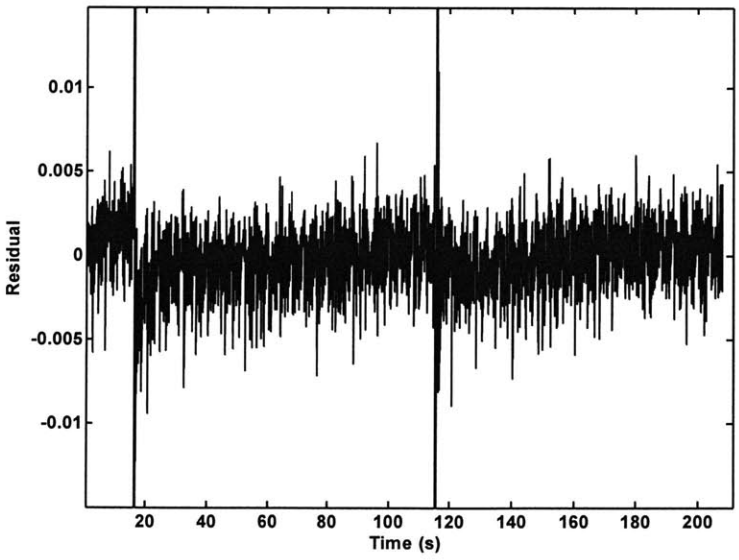

Figure 3-15: $\varepsilon(t,\theta)$ – Residuals from Identification Data

Although the black box electrical model order is higher than the grey box model, both the electrical and mechanical dynamics can be captured using only 3 poles. The model's pole and zero maps were converted to the s-plane and are shown in Figure 3-16 for the final black box model. The leftmost plot shows the electrical model while the rightmost plot shows the mechanical model.

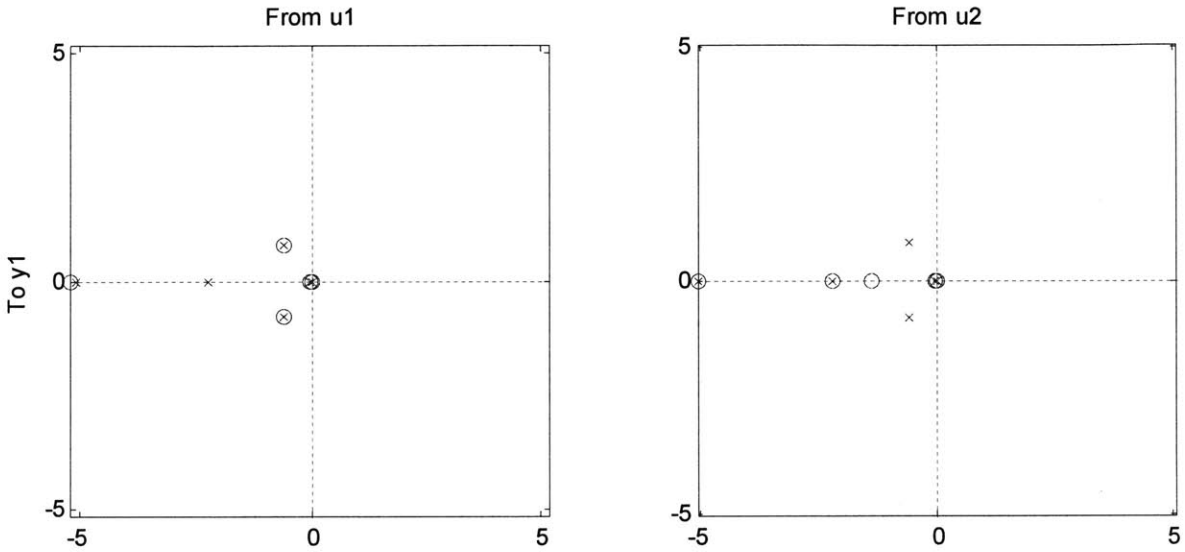

Figure 3-16: Pole-Zero Constellations for Identified Model

From Figure 3-16, it appears that the model order can be pared down because of the high frequency pole and zero. Removal of these frequencies is likely to leave the low frequency dynamics (dynamics occurring below 5 rad/s) unchanged. However, since the PPy actuators used to obtain the data can operate at frequencies of up to 1 Hz (6.3 rad/s), the highest frequency poles and zeros are indeed necessary. Overall the black box modeling provides similar model order to the grey box modeling and the black box results reinforce the grey box model structure.

3.4. References

[1] Bowers T., *Modeling, Simulation, and Control of a Polypyrrole-Based Conducting Polymer Actuator*, S.M. Thesis, MIT, Cambridge, MA, 2004.

[2] Qi B., Lu W., and Mattes B.R., "Control System for Conducting Polymer Actuators", *Smart Structures and Materials EAPAD*, Vol 4695, pp. 359-366, 2002.

[3] Madden J., *Conducting Polymer Actuators*, Ph.D. Thesis, MIT, Cambridge, MA, 2000.

[4] Della Santa A., De Rossi D., and Mazzolidi A., "Characterization and modeling of a conducting polymer muscle-like linear actuator", *Smart Materials and Structures*, Vol 6, pp. 23-24, 1997.

[5] Madden J., Madden P., Anquetil P., and Hunter I., "Load and Time Dependence of Displacement in a Conducting Polymer Actuator", *Material Research Society Proceedings*, Vol 698, pp. 137-144.

[6] Ljung L. *System Identification: Theory for the User*, 2nd Ed. Prentice Hall. Upper Saddle River, NJ, 1999.

Chapter 4
Monitoring and Preventing Actuator Degradation

4.1 Online Estimation of Polymer Electrical Impedance

PPy actuators degrade through an oxidative process when used repeatedly. To date, PPy actuators have been treated only minimally on a systems level. Moreover, degradation has been scarcely treated in the controls, instrumentation, and robotics literature. The general hardware framework for preventing degradation derives from Figure 4-1.

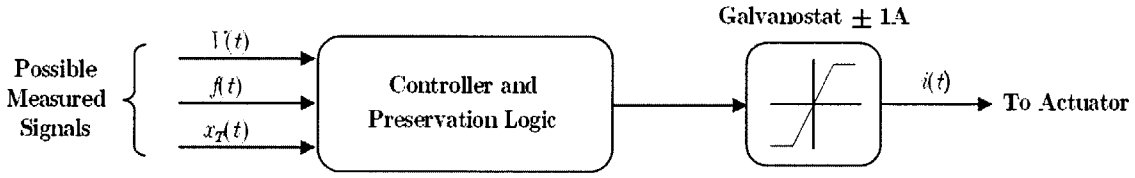

Figure 4-1: General Hardware Layout for Control and Degradation Prevention

A natural direction for the present research was to address two central difficulties preventing widespread use of PPy actuators: the detection of degradation and the prevention of degradation. The key metric indicative of PPy degradation is an increase in impedance [1]. It is speculated that greater impedance leads to reduced charging and therefore reduced mechanical stroke. The following analysis presents a method is presented to monitor deleterious impedance increases and curb degradation through concomitant voltage de-rating. To further bolster the actuator protection scheme, short term overloads are prevented by monitoring the voltage across the actuator V_{PPy}.

Chapter 3 illustrated that the PPy charging dynamics can be modeled well by the RC circuit shown in Figure 4-2.

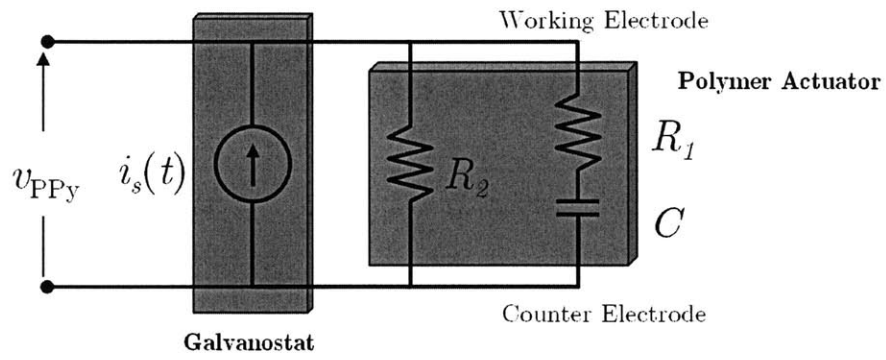

Figure 4-2: RC Impedance Model Used to Model PPy Actuator Charging Dynamics

The circuit in Figure 4-2 can be thought of as a frequency dependent resistance or impedance. Note that the concept of impedance is valid for linear systems and therefore the linearity of the electrical model is assumed. It was also shown in Chapter 3 that the electrical circuit parameters could be identified using a batch least squares process where the data were processed after they were collected. Pragmatically, to monitor degradation, the impedance, or more precisely the increase in impedance from a reference datum, must be known while the actuator is in use. A very robust method for obtaining estimates of time varying impedance is to use recursive least squares with a suitable forgetting factor. The next section describes the technique of real-time impedance identification.

4.1.1 RLS Formulation

Online impedance monitoring is the first step in the proposed actuator preservation strategy. The simplicity of the electrical model allows for online estimation of R_1, R_2, and C using the recursive least squares technique. For convenience, some of the equations listed in Chapter 3 will be repeated. The impedance of the electrical network shown in Figure 4-2 is given by

$$Z(s) = \frac{V_{PPy}(s)}{I(s)} = \frac{R_1 R_2 C s + R_2}{(R_1 + R_2)Cs + 1}. \tag{4.1}$$

Using Tustin's approximation and a sampling time of T_s, the impedance can be written in discrete autoregressive with exogenous input (ARX) form as follows:

$$Z(z) = \frac{V_{PPy}(z)}{I(z)} = \frac{b_0 + b_1 z^{-1}}{1 + az^{-1}}, \tag{4.2}$$

where the discrete parameters map nonlinearly to the continuous parameters as

$$R_1 = \frac{-(b_o + b_1)(b_o - b_1)}{2(ab_o - b_1)}, \tag{4.3}$$

$$R_2 = \frac{b_o + b_1}{1 + a}, \tag{4.4}$$

and

$$C = \frac{-(ab_o - b_1)T_s}{(b_o + b_1)^2}. \tag{4.5}$$

Hence, using the notation in [2], the predictor used to formulate the least squares problem can be stated as follows:

$$\hat{v}_{PPy}(t) = \varphi(t)^T \hat{\theta} = \begin{bmatrix} i_s(t) & i_s(t-1) & -v_{PPy}(t-1) \end{bmatrix} \begin{bmatrix} b_0 & b_1 & a \end{bmatrix}^T, \tag{4.6}$$

where the hat over a variable indicates that the variable is an estimate of the true system value.

The RLS algorithm updates an initial guess of the parameter vector $\hat{\theta}(0)$ based on the data vector $\varphi(t)$ acquired at each time step. In the traditional LS algorithm (batch processing least squares), an estimate of the parameters is obtained using N data vectors $\varphi(1)$ $\varphi(2)...\varphi(N)$ and single inversion of the matrix $P^{-1} = \Phi\Phi^T$ where $\Phi = [\varphi(1)$ $\varphi(2)...\varphi(N)]$. The LS estimate is written $\hat{\theta} = PB = (\Phi\Phi^T)^{-1}\sum_{t=1}^{n} y(t)\varphi(t)$ with $y(t)$ being the measured output at each time step. In the recursive algorithm, inversion of the large $\Phi\Phi^T$ matrix is not necessary because the covariance matrix can be updated at each time step using the matrix inversion lemma. The resulting algorithm is given in Equations 4.7 and 4.8.

$$\hat{\theta}(t) = \hat{\theta}(t-1) + \frac{P_{t-1}}{1 + \varphi(t)^T P_{t-1}\varphi(t)}(y(t) - \varphi(t)^T \hat{\theta}(t-1)) \tag{4.7}$$

$$P_t = P_{t-1} - \frac{P_{t-1}\varphi(t)\varphi(t)^T P_{t-1}}{1 + \varphi(t)^T P_{t-1}\varphi(t)} \tag{4.8}$$

The initial conditions required for the algorithm are an initial parameter guess $\hat{\theta}(0)$, which is arbitrary, and an initial positive definite covariance matrix P_0, which is typically chosen as the identity matrix in $\mathbb{R}^{m\times m}$ with m equal to the dimension of the parameter vector. To give preference to recent data and to monitor trends in the polymer impedance, the RLS algorithm can be modified to include a forgetting factor α_f, where $\alpha_f < 1$. The forgetting factor allows for exponential weighting of the data. Data points collected k steps prior to the current time step will be given a weight α_f^k. The forgetting factor is introduced into the algorithm by premultiplying Equation 4.8 by $1/\alpha_f$:

$$P_t = \frac{1}{\alpha}\left(P_{t-1} - \frac{P_{t-1}\varphi(t)\varphi(t)^T P_{t-1}}{1 + \varphi(t)^T P_{t-1}\varphi(t)} \right). \tag{4.9}$$

One difficulty associated with Equation 4.9 is that when the system parameters enter a steady state, the covariance matrix P_t can grow in an unbounded manner. Thus, to avoid instability in the algorithm, the covariance matrix must be reset to some arbitrary positive definite matrix at suitable time intervals.

Assuming persistence of excitation of the galvanostat current input, an online estimate of R_1, R_2, and C will be available after applying Equations 4.3 to 4.5 to each new estimate of the discrete parameters a, b_1, and b_2. The impedance can be estimated in real time using Equation 4.10:

$$\|Z(j\omega)\| = \left\| \frac{R_2 + R_1 R_2 C j\omega}{1 + (R_1 + R_2)C j\omega} \right\| = \frac{\sqrt{{R_2}^2 + (R_1 R_2 C\omega)^2}}{\sqrt{1 + ((R_1 + R_2)C\omega)^2}}, \tag{4.10}$$

where ω is taken as the dominant angular frequency of the applied current input and the voltage output.

4.1.2 Forgetting Factor Selection

The selection of a forgetting factor is an important step towards a successful impedance detection algorithm. The RLS update law using a forgetting factor is stated in Equation 4.9. It is necessary to consider three things in order to select a forgetting factor: the sampling interval, the speed with which impedance is expected to change, and the relative weight of past data. Specifically, the forgetting factor to achieve an $\varepsilon\%$ weighting of the data point that occurred T_f prior to the current time step can be selected based on the following equation:

$$\alpha_f = 10^{(\log_{10}(\varepsilon)-2)\left(\frac{T_s}{T_f}\right)}, \tag{4.11}$$

where T_s is the sampling interval and all other terms remain as previously defined.

4.2 Minimizing Degradation Through Voltage De-rating

Large voltage inputs applied for long periods of time can lead to rapid degradation of the actuator material. Moreover, large voltages that occur as transients although less damaging will still lead to degradation that accrues over time [3]. In short, the rate of permanent degradation can be accelerated in a closed loop scenario due to excessive voltages applied to the polymer. Experimental analysis of PPy actuators has shown that consistent performance, and hence lifecycle, is limited if the actuators are used to generate electrochemical strains in excess of 7% at 5 MPa [2].

The above factors suggest that degradation can be avoided by applying voltages conservatively. However, maximum actuator performance comes only from maximum applied voltages. Thus, the method proposed here involves an online de-rating scheme for actuators where successively smaller voltage saturation limits are imposed on the actuator. This method is conceptual and was not tested experimentally, but the experimental methodology follows logically from the ideas presented in the following paragraphs.

Section 4.3 will show that a typical actuator may exhibit an impedance increase of 15-25% during its lifetime with minimum impedance occurring after some repeated cycling. The impedance identified during the first use of the actuator is taken as the base value from which percentage increases are computed. The overall preservation strategy is shown in Figure 4-3 and Figure 4-4:

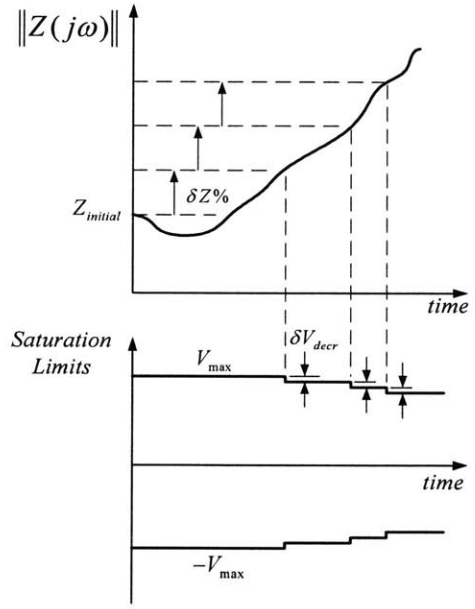

Figure 4-3: Impedance Changes and Associated Voltage Envelope Reduction

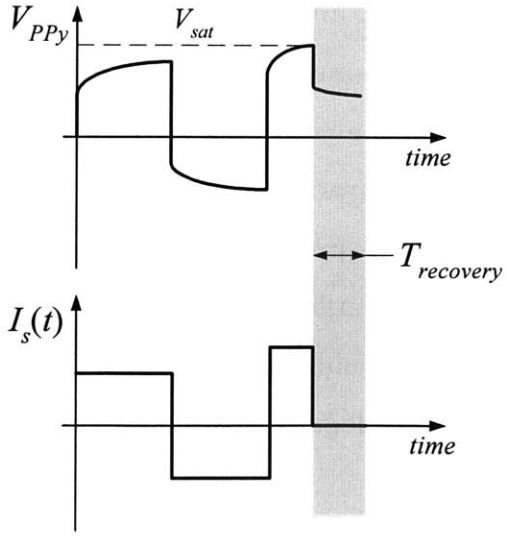

Figure 4-4: Enforcing Voltage Saturation Using Current Control

Figure 4-3 shows long term impedance monitoring and its correspondence to the reduction in the allowed voltage envelope; Figure 4-4 shows how the voltage saturation is enforced using the control input. As shown in Figure 4-3, initial voltage saturation limits of $\pm \underline{V}_{max}$ are set to provide the best possible control authority without reaching the oxidation potential of the PPy material. These limits will be decremented in absolute value by an amount δV_{der} for each increase in impedance of $\delta Z\%$. Note that $\underline{V}_{max}$, δV_{der}, $\delta Z\%$ are design parameters and specific parameter values may be assigned depending on the application. For example, for an actuator that must perform very small stroke tasks for a long period of time, more conservative values may be used. If large stroke is desired and a decrease in lifecycle is acceptable, then the preservation will be less conservative, having a small value for δV_{der} and a large value for $\delta Z\%$. Figure 4-3 shows that the voltage saturation limits as shown in Figure 4-2 are enforced by setting the current to zero for a time of $T_{recovery}$. A finite time $T_{recovery}$ is needed to avoid rapid switching of the current source. Note that during $T_{recovery}$ a feedback controller must be turned off to avoid windup of the error associated with integral action. Also $T_{recovery}$ should be selected to be as small as possible to avoid sacrificing performance. In order to provide reasonable estimates of impedance, a large RLS time window of length T_f is used as discussed in Section 4.1.2. Within T_f, the RLS estimate will stabilize before the controller checks the computed impedance value.

4.3 Experimental Results

The experimental results described in this section include impedance identification perfomed using both LS and RLS techniques. The batch LS method is a desirable data processing method because of its stability and clarity when presenting the impedance identification concept. An experiment conducted using RLS will be described later in this section.

A 12-layer actuator (Actuator 135 per Eamex's model numbering scheme) was cycled electrically for approximately 5 hours using a 0.1 Hz current square wave of ±1.3 A, which gave an approximate initial output voltage of ± 1.15V PP. The actuator was loaded

isotoncially with 300 g in the vertical test stand described in Section 2.1. An inspection of actuator 135 following failure revealed that the electrolyte solution evaporated during operation and the PPy layers eventually broke with the continuous operation. The data for the experiment are shown in Figure 4-5.

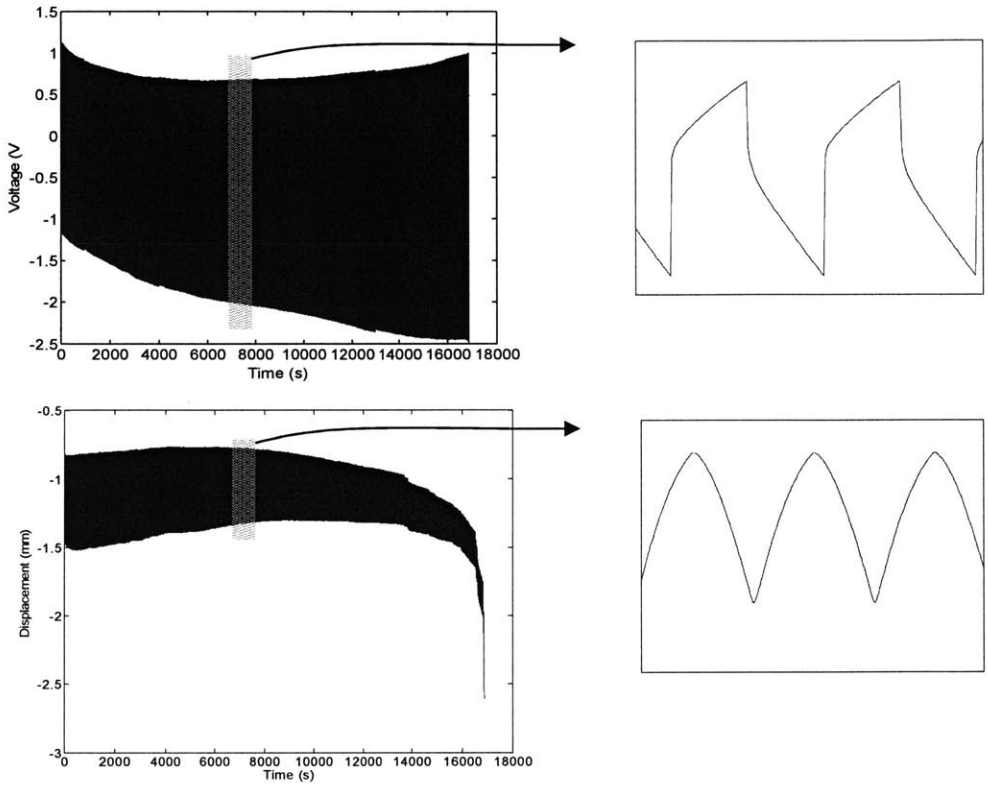

Figure 4-5: Extended Electrical Cycling Culminating in Failure of PPy Actuator 135 Under 300g Load

Using a batch least squares process for every 1000 voltage and current data points (100 s), the parameters $\theta = [a\ b_0\ b_1]$ were identified from the impedance model in Equation 4.2. Then, using the relationships derived from Tustin's formula (Equations 4.3 to 4.5), the resistances and capacitance were computed. The resulting resistances and capacitance are plotted in Figure 4-6.

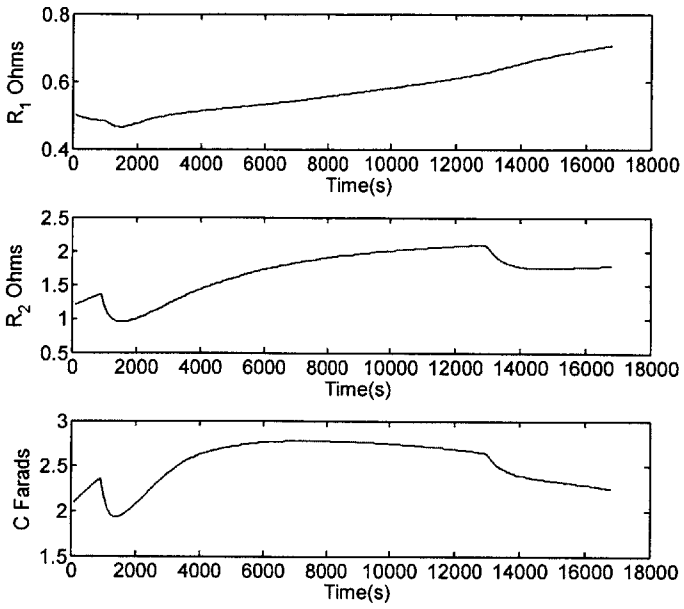

Figure 4-6: Resistances and Capacitance Identified Using Batch LS

The impedance versus time was computed according to Equation 4.10. A value of $\omega = 0.628$ rad/s (0.1Hz) was used because this was the dominant frequency of the applied current square wave. The result of the impedance computation is shown in Figure 4-7.

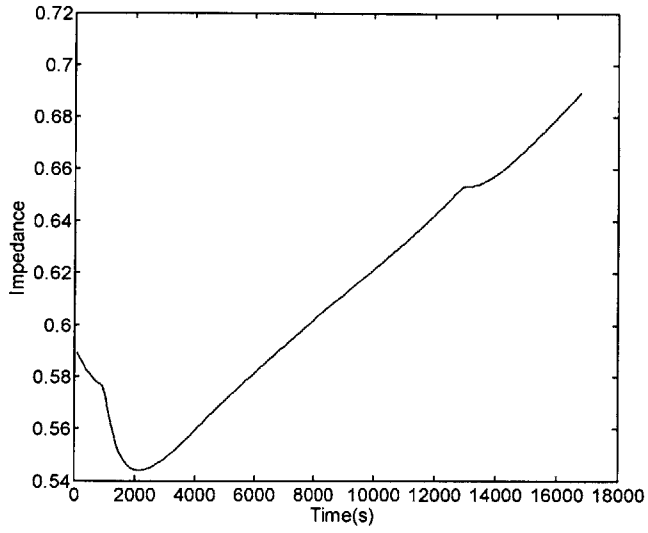

Figure 4-7: Impedance (Ω) versus Time (s) for Actuator 135

Note that the impedance curve in Figure 4-7 exhibits an initial decrease. Upon reaching a minimum value at 2100 s, the impedance increases monotonically and linearly. The

linear behavior beyond 2100 s suggests that a simple model for impedance increase based on the number of electrical cycles may be possible.

In a separate experiment, data were collected with concurrent use of an RLS algorithm. The RLS algorithm was implemented in LabVIEW. See Appendix B for the associated VI. Data were collected at 15 Hz. Figure 4-8 shows the online identification of the electrical model parameters for a 12-layer PPy actuator. The actuator was given a 300 g axial load and actuated electrically with a 0.1 Hz, 1.2 V peak to peak voltage square wave applied between the working and counter electrodes. The actuator was mounted in the vertical test stand described in Section 2.1. In this implementation of the RLS algorithm, the covariance was reset to the identity matrix approximately 5 seconds and a forgetting factor of $\alpha_f = 0.985$ was used.

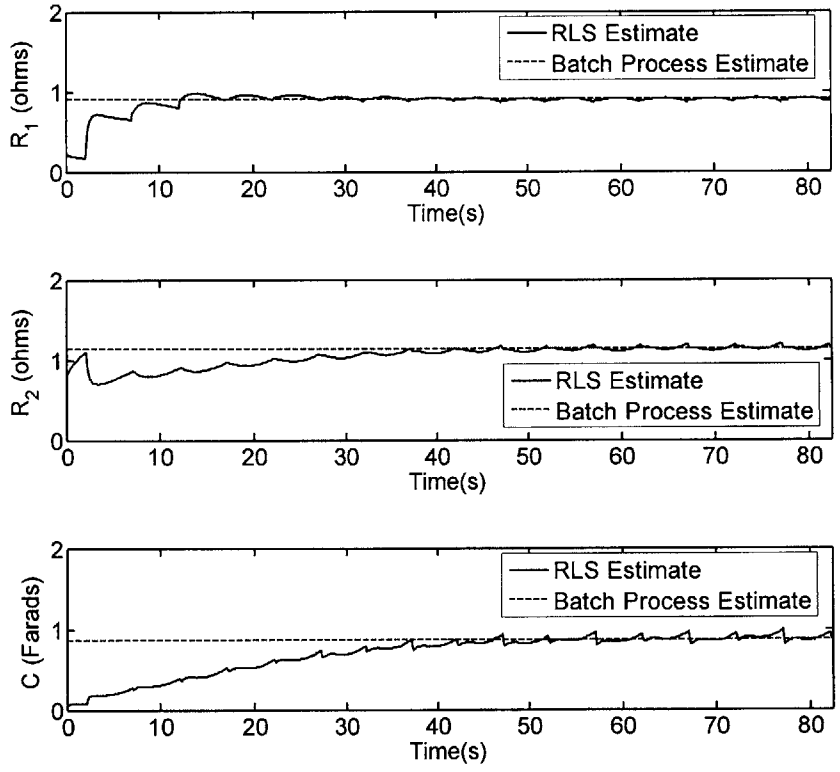

Figure 4-8: LS and RLS Electrical Parameter Estimates for 12 Layer Actuator

Overall, this chapter has described both LS and RLS techniques for monitoring actuator impedance. It has been shown that both techniques can be employed

successfully to obtain an estimate of actuator electrical impedance as a function of time. Thus, the relative degradation of the actuator can be estimated. If extended performance is desired, the voltage derating scheme described in Section 4.2 can be used.

4.4 References

[1] Otero T., Marquez M., and Suarez I., "Polypyrrole: Diffusion Coefficients and Degradation by Overoxidation", *J. Phys. Chem.*, B, Vol 108, pp. 15429-15433, 2004.

[2] Ljung L. *System Identification: Theory for the User*, 2nd Ed. Prentice Hall. Upper Saddle River, NJ, 1999.

[3] Madden J., Cush R., Kanigan T., and Hunter I., "Fast contracting polypyrrole actuators", *Synth. Metals*, Vol 113, pp. 185–193, May 2000.

Chapter 5
Application of Polypyrrole Actuators to a Humanoid Foot

5.1 Multifunctional Nature of Polypyrrole Actuators

Polypyrrole actuators are desirable as artificial muscles because they 1) have inherent stiffness and damping and 2) have the ability to modulate their behavior through appropriate electrical inputs. DC motors have the latter ability only. Like natural muscles, PPy actuators can behave as stiff, compliant, or dissipative elements depending on the required task, anatomical placement, and phase of locomotion.

As discussed in Chapter 1, the stagnation point for much of humanoid robotics has been a lack of suitable actuators or robot muscles. Traditional electromechanical actuators are not efficient at mimicking natural muscle behavior because they do not possess an inherent stiffness, they have a large form factor, and they require a transmission element. Ultimately, electromechanical actuators introduce unwanted noise, backlash, and weight to the robotic system. To illustrate a drawback of traditional electromechanical actuators, consider the transfer function relationship for a DC motor with rotor inertia J, armature resistance R, and torque-back emf constant K:

$$\frac{\Theta(s)}{V(s)} = \frac{\frac{1}{K}}{s(\frac{RJ}{K^2}s + 1)}. \tag{5.1}$$

Equation 5.1 expresses the armature voltage V to angular displacement Θ relationship in the s-domain. The presence of the free integrator in Equation 5.1 indicates that a constant applied voltage input results in a linearly increasing angular displacement. Alternatively, one can interpret the free integrator as a lack of stiffness in the system. This interpretation shows that DC motors require a non-zero voltage input to behave as a stiffness element. DC motors have successfully been employed to mimic stiffness behavior or mechanical impedance. The idea of impedance control was first enumerated in [1]. Unlike DC motors, however, PPy muscle actuators inherently possess the

requisite stiffness and damping found in natural muscles. This key advantage is a central premise of this chapter.

A comprehensive overview of the role of muscles in successful locomotion for animals is given in [2]. As described [2], the changing muscle behavior can be quantified using a work loop diagram. Work loops show the relationship between force and length as a muscle performs a given task. For repetitive motion (for example locomotion) the force versus length curves must be closed. Figure 5-1 illustrates representative work loops for positive work production and energy dissipation. Note that the area enclosed by a work loop yields an energy value. When a loop is traversed counterclockwise, energy is produced (Figure 5-1a). When the loop is traversed clockwise, then energy is absorbed (Figure 5-1b).

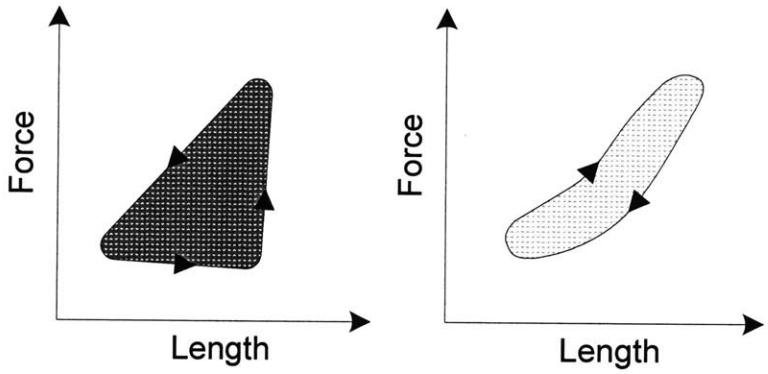

Figure 5-1: (a) Positive Power Producing Work Loop (b) Power Absorbing Work Loop as Adapted from [2]

Using electrical excitation, PPy actuators can modify their behavior to match a desired work loop profile. However, it is important to note that the current conducting polymer technology has a limited control authority due to degradation by oxidation, small strain, and small rate of strain as described in Chapter 1.

5.2 Design of a Humanoid Foot

In the design of a humanoid foot the two key metrics are stiffness and damping. To minimize the required electrical excitation of PPy muscle actuators, the overall foot

and leg system must inherently possess the desired stiffness and damping properties. Moreover, the musculoskeletal architecture is critical to successful locomotion because it establishes the "preflex" that acts instantaneously to a sudden disturbance.

Before creating the humanoid foot, relevant biomechanics research was consulted. Several articles published in engineering biomechanics journals address the biomechanical analysis of the human foot. Particularly relevant articles include [3] and [4]. However, a majority of biomechanics research is focused upon quantifying ground reaction forces and deformation of the bones inside the foot. The humanoid foot was designed by taking insight from human anatomy and references such as [3] and [4].

The annotated solid model of the foot assembly is given in Figure 5-2. Four actuators, arranged in two antagonistic pairs, are used in the present design. The actuators are placed in a manner analogous to the tendons and muscles of the anterior and posterior compartments of the human lower leg. The artificial tendon material is 0.025in Kevlar cord.

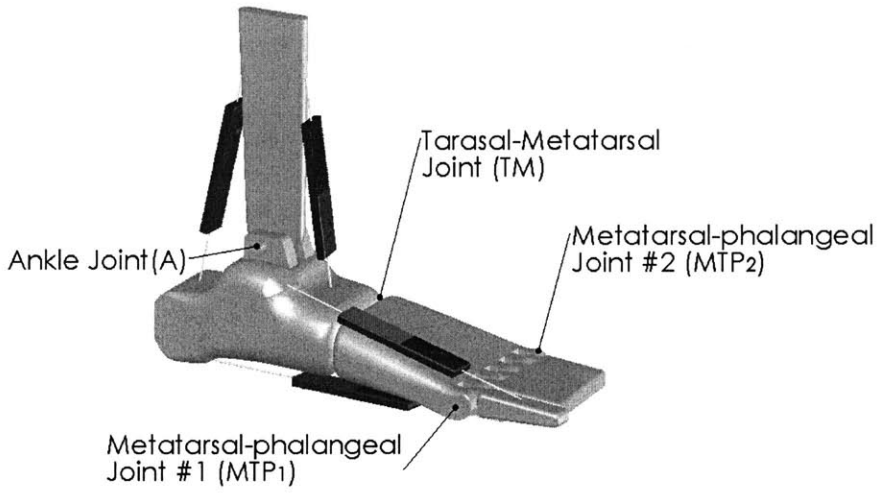

Figure 5-2: SolidWorks Design of Four Degree of Freedom Anthropomorphic Foot with Artificial Muscle Actuators Attached

In Figure 5-2, the joints are labeled according to the related human counterpart. For an overview of the anatomy of a human foot, refer to Appendix C. The ankle (A) and

metatarsal-phalangeal (MTP_i) joints are designed to be purely revolute, while the tarsal-metatarsal (TM) joint is intended to be revolute within a small neighborhood of the reference configuration shown. An initial 2.5:1 prototype of this design was realized using a Dimension SST and four 12-layer PPy actuators made by Eamex Corp. The prototype without the actuators attached is shown in Figure 5-3.

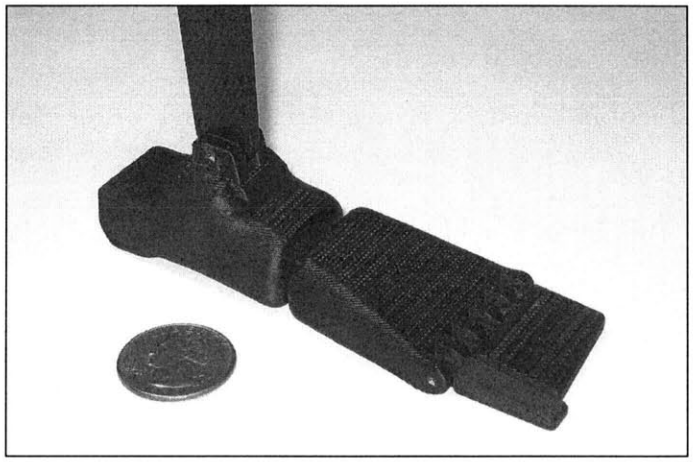

Figure 5-3: 2.5:1 Physical Realization of Four Degree of Freedom Anthropomorphic Foot without Artificial Muscle Actuators Attached

A comparison of the design in Figures 5-2 and 5-3 with a human foot reveals many important similarities. First, the gross motion of a human foot is determined by plantar and dorsal flexion as well as rotation of the MTP joints, especially the first toe joint. The importance of the MTP_1 joint justifies its independence from the remaining MTP joints, which have been amalgamated into the link revolving at MTP_2. Actuation of this joint is not considered in this work. Second, the human calcaneus, or heel bone, serves as the moment arm for forces applied to the foot by the posterior leg muscles. This protuberance enables effective plantar flexion both in humans and in the anthropomorphic design. Finally, the artificial foot contains a large longitudinal arch similar to the two longitudinal arches found in the human foot. In humans, the arches of the foot contribute to the passive compliance characteristics of the foot. The effectiveness of the arches also depends on the mechanical properties of the metatarsal

bones along its length. The dependence of arch deflection on material properties will not be discussed in the following section, which focuses on a rigid body analysis only.

5.3 Jacobian Analysis

A convenient and systematic way to characterize the compliance and damping of a robot kinematic chain is through Jacobian analysis. A concise discussion of the techniques in this section can be found in [5].

Generally, a Jacobian matrix is a matrix of first order partial derivatives that relates two vector spaces. In the context of a robotic manipulator, the two vector spaces are typically the joint velocity space and the task velocity space. Thus, the Jacobian relates velocities of individual actuators to the velocity of the end effector in Cartesian task space. The Jacobian matrix is also configuration dependent with several entries containing nonlinear trigonometric terms. An alternative definition for the Jacobian $\mathbf{J}$, which coincides well with the analysis in subsequent sections, can be stated in terms of virtual displacements in the joint space and virtual displacements in the Cartesian task space. For an infinitesimal displacement vector $\delta\boldsymbol{\theta}$ in the m dimensional actuator space, the corresponding displacement $\delta\mathbf{x}$ in the n dimensional task space is given by

$$\delta\mathbf{x} = \begin{Bmatrix} \delta x_1 \\ \delta x_2 \\ \vdots \\ \delta x_n \end{Bmatrix} = (\mathbf{J})(\delta\boldsymbol{\theta}) = \begin{pmatrix} \frac{\partial x_1}{\partial \theta_1} & \frac{\partial x_1}{\partial \theta_2} & \cdots & \frac{\partial x_1}{\partial \theta_m} \\ \frac{\partial x_2}{\partial \theta_1} & \frac{\partial x_2}{\partial \theta_2} & \cdots & \frac{\partial x_2}{\partial \theta_m} \\ \vdots & \vdots & \ddots & \vdots \\ \frac{\partial x_n}{\partial \theta_1} & \frac{\partial x_n}{\partial \theta_2} & \cdots & \frac{\partial x_n}{\partial \theta_m} \end{pmatrix} \begin{Bmatrix} \delta\theta_1 \\ \delta\theta_2 \\ \vdots \\ \delta\theta_m \end{Bmatrix}. \tag{5.2}$$

5.3.1 Jacobian Matrices Relating the Actuator, Joint, and Cartesian Spaces

Figure 5-4 shows the nomenclature used in the computation of Jacobian matrix relating the joint space and the Cartesian task space for the foot. As seen in Figure 5-4,

the 3-link representation of the foot considers the midpoint of the first phalanx as the end of the kinematic chain.

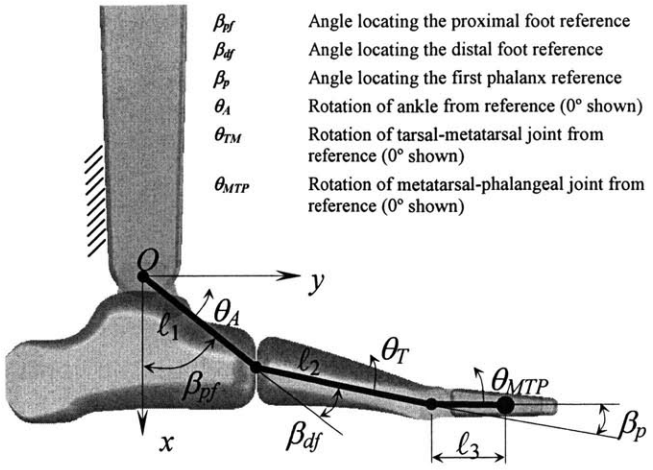

Figure 5-4: Three-Link Description of Foot for Consideration of Stiffness and Damping

The reference coordinate system is attached to the leg, which is assumed to be fixed in Cartesian space for the purpose of Jacobian analysis. This assumption is tantamount to an infinite upper body inertia. Although this approximation will not hold in real systems, it is expected that the stiffness and damping values resulting from the Jacobian analysis will be reasonably accurate. Another important assumption is that the angles of deflection at the joints will assumed to be small deviations from the reference configuration shown (that is, $\theta_A = \delta\theta_{\mathrm{A}}$, $\theta_{TM} = \delta\theta_{\mathrm{TM}}$, $\theta_A = \delta\theta_{\mathrm{MTP}}$).

The Jacobian matrix $\mathbf{J}_{\theta\to x}$ for the 3-link representation of the foot is given by Equation 5.3 where a shorthand notation has been employed for sine and cosine terms. The shorthand s indicates a sine and the c indicates a cosine. The commas between subscripts indicate the addition of the angles with the corresponding subscript. For example, $-\ell_3 c_{A,TM,MTP}$ is shorthand for $-\ell_3 \cos(\theta_A + \theta_{TM} + \theta_{MTP})$. As indicated by the subscript $\theta\to x$, Equation 5.3 provides the transformation between the joint space and the Cartesian task space.

$$\mathbf{J}_{\theta \to x} = \begin{pmatrix} -\ell_1 s_{pf,A} - \ell_2 s_{pf,df,A,TM} - \ell_3 c_{A,TM,MTP} & \\ \ell_1 c_{pf,A} + \ell_2 c_{pf,df,A,TM} - \ell_3 s_{A,TM,MTP} & \\ -\ell_2 s_{pf,df,A,TM} - \ell_3 c_{A,TM,MTP} & -\ell_3 c_{A,TM,MTP} \\ \ell_2 c_{pf,df,A,TM} - \ell_3 s_{A,TM,MTP} & -\ell_3 s_{A,TM,MTP} \end{pmatrix} \tag{5.3}$$

Notice that the Jacobian matrix above is dependent on the configuration of the foot.

Figure 5-5 shows the nomenclature used in the computation of the Jacobian matrix in the actuator coordinate system. All of the linear displacements of the actuators and tendon-like attachments were mapped to the joint angles using triangle approximations and the law of cosines.

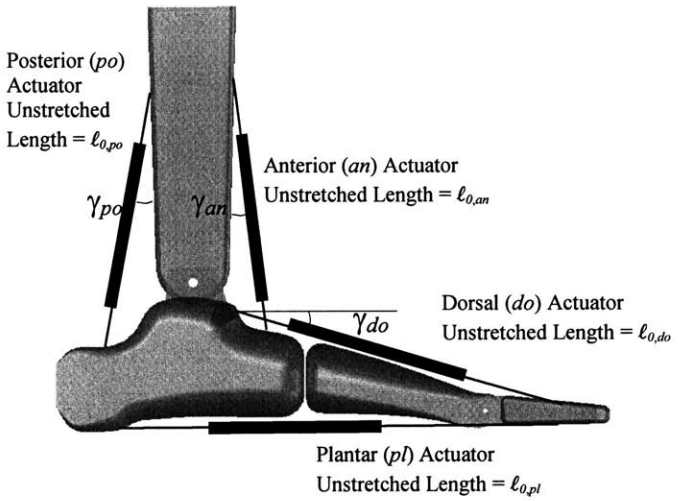

Figure 5-5: Actuator Reference Angles and Lengths Used for Establishing $\mathbf{J}_{\ell \to \theta}$ Matrix

The Jacobian matrix relating the actuator space to the joint space is given by Equation 5.4:

$$\mathbf{J}_{\ell\to\theta} = \begin{bmatrix} \frac{-2\ell_{an}}{\sqrt{(2\ell_{an}r_{an}\sin(\beta_{an}-\gamma_{an}))^2+4r_{an}{}^2(\ell_{an,0}{}^2-\ell_{an}{}^2)}} & \cdots \\ 0 & \\ 0 & \end{bmatrix}$$

$$\begin{bmatrix} \frac{2\ell_{po}}{\sqrt{(2\ell_{po}r_{po}\sin(\gamma_{po}-\beta_{po}))^2+4r_{po}{}^2(\ell_{po,0}{}^2-\ell_{po}{}^2)}} & \cdots \\ 0 & \\ 0 & \end{bmatrix}$$

$$\begin{bmatrix} 0 & 0 \\ \varepsilon_{do} & \varepsilon_{pl} \\ \frac{-2\ell_{do}}{\sqrt{(2\ell_{do}r_{do}\sin(\gamma_{do}))^2+4r_{do}{}^2(\ell_{do,0}{}^2-\ell_{do}{}^2)}} & \frac{\ell_{pl}r_{pl}}{\sqrt{\ell_{pl}{}^2-\ell_{pl,0}{}^2}} \end{bmatrix}. \quad (5.4)$$

In Equation 5.4, r_{an}, r_{po}, r_{do}, and r_{pl} are radii from a joint to an artificial muscle attachment site. For example, r_{an} corresponds to this distance between the angle joint and the anterior actuator's connection point. β_{an} and β_{po} are two angles that locate the actuator attachment points as referenced from the vertical.

5.3.2 Simplified Actuator Model

The definition for compliance and damping for the ith actuator in the actuator space is given in Equations 5.5 and 5.6:

$$c_i = k_i{}^{-1} \triangleq \left(\frac{\partial F_i}{\partial x_{T,i}}\right)^{-1} \quad (5.5)$$

and

$$b_i \triangleq \left(\frac{\partial F_i}{\partial \dot{x}_{T,i}}\right), \quad (5.6)$$

where c_i is compliance, b_i is a damping coefficient, $x_{T,i}$ is total displacement, and F_i is the actuator force. Jacobian compliance and damping analysis is unnecessarily cumbersome if the 2-pole 2-zero model described in Section 3.1 is used to compute Equations 5.5 and 5.6. Thus, this section will present a simplified version of the mechanical model.

The dominant mechanical dynamics of the PPy actuator can be captured by the Maxwell model shown in Figure 5-6.

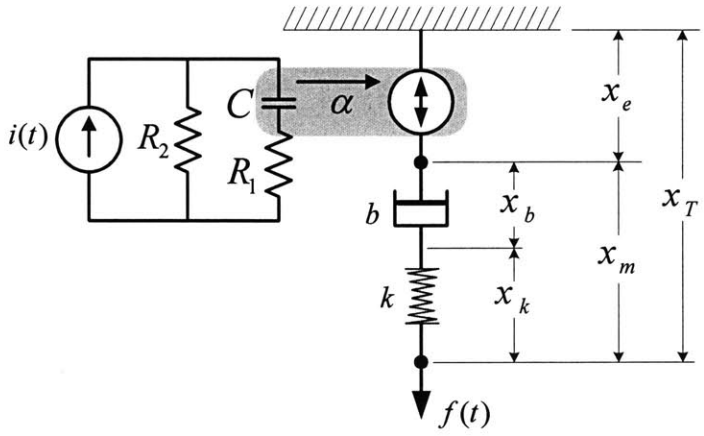

Figure 5-6: Maxwell Model Used for Jacobian Compliance and Damping Analysis

As shown in Figure 5-7, the Maxwell model agrees quite well with the experimentally measured force and displacement data. Notice, however, the slight disparity that occurs between the measured and predicted displacement for times greater than 500 s. The data shown in Figure 5-7 were obtained under the same experimental conditions listed in Section 3.3.1.

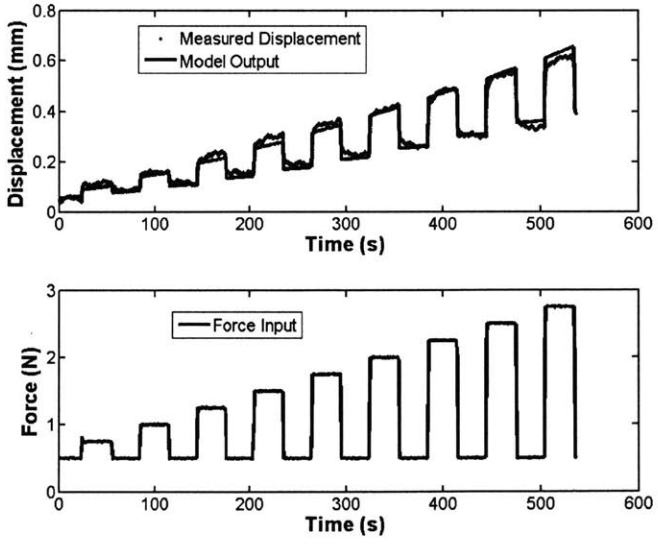

Figure 5-7: Experimental Validation of Maxwell Model for a 12-layer PPy Actuator. Measured Data is Shown versus Model with $k = 9100$ N/m and $b = 1.7\times10^{6}$ N·s/m

5.3.3 Compliance and Damping Analysis

The compliance of the foot can be established using Equation 5.3 to 5.6 using the typical symmetric transformation in Equation 5.7 where $\mathbf{C}_\ell$ is the diagonal compliance matrix given in Equation 5.8.

$$\mathbf{C}_x = \mathbf{J}_{\theta\to x}[\mathbf{J}_{\ell\to\theta}\mathbf{C}_\ell\mathbf{J}^T_{\ell\to\theta}]\mathbf{J}^T_{\theta\to x} \tag{5.7}$$

$$\mathbf{C}_\ell = \begin{pmatrix} k_{an}^{-1} & 0 & 0 & 0 \\ 0 & k_{po}^{-1} & 0 & 0 \\ 0 & 0 & k_{do}^{-1} & 0 \\ 0 & 0 & 0 & k_{pl}^{-1} \end{pmatrix} \tag{5.8}$$

All of the design variables enter the compliance equation through the Jacobian matrices, which creates an opportunity for highly effective design optimization. Numerical values of the compliance will be given later in this section.

Similar to the compliance analysis described above, the damping matrix $\mathbf{D}_\ell$ in the actuator coordinate system can be written in the task coordinate system by using the Jacobian matrices found previously:

$$\mathbf{D}_x = \mathbf{J}_{\theta\to x}[\mathbf{J}_{\ell\to\theta}\mathbf{D}_\ell\mathbf{J}^T_{\ell\to\theta}]\mathbf{J}^T_{\theta\to x} \tag{5.9}$$

where $\mathbf{D}_\ell$ is the diagonal matrix given in Equation 5.10:

$$\mathbf{D}_\ell = \begin{pmatrix} b_{an} & 0 & 0 & 0 \\ 0 & b_{po} & 0 & 0 \\ 0 & 0 & b_{do} & 0 \\ 0 & 0 & 0 & b_{pl} \end{pmatrix}. \tag{5.10}$$

Again, note that the geometric design parameters are involved in the damping characteristics of the foot and leg assembly.

The numerical values used to compute the stiffness and damping matrices are shown in Table 5-1. The values in Table 5-1 were obtained using the measured dimensions of the design, which are comparable to those in the human foot.

Table 5-1: Nominal Design Parameters Used to Obtain Numerical Stiffness and Damping Matrices

Symbol	Quantity	Value	Units
ℓ_1	Link 1 Length	50.8	mm
ℓ_2	Link 2 Length	62.5	mm
ℓ_3	Link 3 Length	23.6	mm
$\ell_{po,0}$	Initial *po* act. length	93.2	mm
$\ell_{an,0}$	Initial *an* act. length	97.5	mm
$\ell_{do,0}$	Initial *do* act. length	113.3	mm
$\ell_{pl,0}$	Initial *pl* act. length	139.2	mm
r_{po}	Ankle to *po* attachment radius	41.7	mm
r_{an}	Ankle to *an* attachment radius	18.0	mm
r_{do}	MTP to *do* attachment radius	23.1	mm
r_{pl}	MTP to *pl* attachment radius	16.3	mm
β_{pf}	Initial angle, link 1	49.0	deg
β_{df}	Initial angle, link 2	30.9	deg
β_p	Initial angle, link 3	10.1	deg
β_{po}	Angle locating r_{po}	57.7	deg
β_{an}	Angle locating r_{an}	50.7	deg
γ_{po}	Angle locating *po* act.	12.9	deg
γ_{an}	Angle locating *an* act.	6.1	deg
γ_{do}	Angle locating *do* act.	15.1	deg

Using the values in Table 5-1, the stiffness and damping values obtained in the previous subsection as well as Equations 5.4 and 5.6, the compliance and damping matrices were computed in the task space. Each actuator was assumed to have identical stiffness k and damping b.

$$\mathbf{C}_x = \begin{pmatrix} 1081 & 9.6 \\ 9.6 & 7.3 \end{pmatrix} mm / N \tag{5.11}$$

$$\mathbf{D}_x = \begin{pmatrix} 1.7 \times 10^7 & 1.5 \times 10^5 \\ 1.5 \times 10^5 & 1.1 \times 10^5 \end{pmatrix} N \cdot s/mm \tag{5.12}$$

Notice that the compliance and damping are two orders of magnitude larger in the x-direction than in the y-direction. When considering forces applied at the first phalanx, the large compliance in the x-direction and relatively small compliance in the y-direction are commensurate with the geometry of the design. Similarly, in Equation 5.12, one expects the inherent damping of a foot's musculoskeletal system to be larger when forces are applied parallel to the y-axis.

The values listed in Equation 5.11 and Equation 5.12 provide a starting point for optimization of the design. Note that the search space for optimal parameters is extremely large as evidenced by the number of parameters in Table 5-1.

5.4 Walking Gait Work Loop Tracking

To test the feasibility of applying PPy actuators as multifunctional muscles in the humanoid foot, numerical simulations of a walking gait were performed using the simplified mechanical model for the actuators. The simplified mechanical model enables generalization to more complex anatomical structures.

5.4.1 Model for Walking Gait

Time profiles of the actuator lengths were specified to achieve a specific foot trajectory resembling the stance phase of a human gait. The stance phase can be broken down into contact, loading, midstance, terminal stance, and pre-swing. Figure 5-8 shows the stance phase of walking along with a qualitative depiction of the actuator length changes and ground reaction forces.

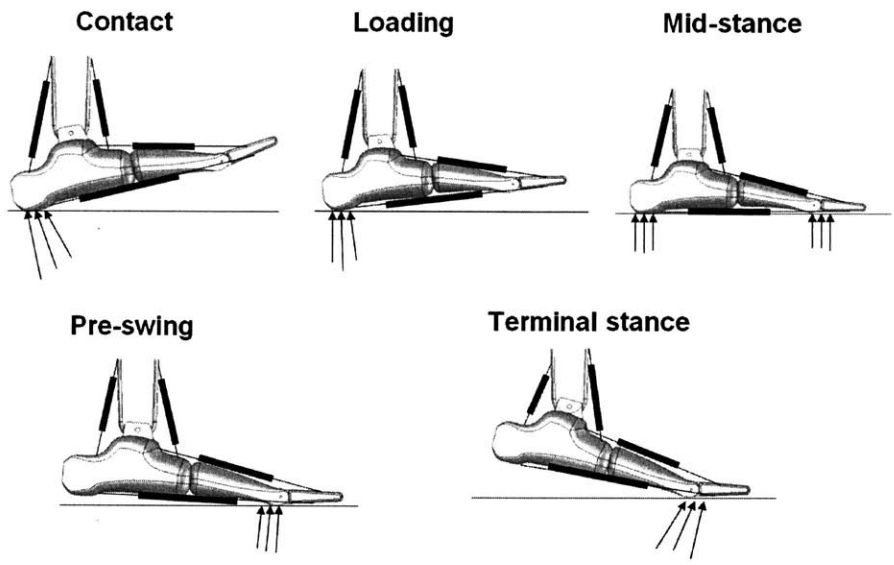

Figure 5-8: Humanoid Foot during Stance Phase of Walking

For simplicity, the length profiles for the actuators are approximated as sinusoids with $t = 0$ corresponding to contact. The actuator length functions are listed below. In keeping with the definitions of this chapter, the actuator total length is indicated by ℓ rather than x_T as in Chapter 3.

$$\ell_{an}(t) = \ell_{an,0} - \sin(2\pi t) \ mm \tag{5.13}$$

$$\ell_{po}(t) = \ell_{po,0} + \sin(2\pi t) \ mm \tag{5.14}$$

$$\ell_{do}(t) = l_{do,0} - \sin(2\pi t) - 1 \ mm \tag{5.15}$$

$$\ell_{do}(t) = l_{do,0} - \sin(2\pi t) - 1 \ mm \tag{5.16}$$

Although not shown here, the joint angular velocities are readily obtained using Equation 5.4.

5.4.2 Work Loop Tracking

Because length changes in the actuators are relatively well known and can be approximated concisely using Equations 5.13 to 5.16, the equations of motion for the Maxwell model shown in Figure 5-6 can be written using length rather than force as the

input function. Applying the Laplace transform with zero initial conditions to the equations of motion leads to the following relation in the s-plane:

$$F(s) = \frac{skb}{bs + k} L(s) - \frac{\alpha kb}{bs + k} I(s), \tag{5.17}$$

where $I(s)$ is the current flowing through the capacitor in the circuit model of Figure 2 and $L(s)$ is the length change. Hence, Equation 5.17 shows that the force in the actuator depends not only on the length but also on the current input.

Using Equation 5.17, the force profile in the actuators was computed. Force versus length profiles for the anterior actuator are shown in Figure 5-9 for $i(t) \equiv 0$ and $i(t) = 1.5 \cdot \sin(13t)$ A. In the case of non-zero current input, the value of α was taken to be 5 mm/C. This value of α is approximately seven to ten times larger than the latest PPy actuator capabilities but provides a more pronounced force versus length profile for illustrative purposes. Note that the work loop in Figure 5-9 was created using a feedforward current input only. Ideally, each actuator in the foot mechanism could follow a prespecified work loop in the presence of disturbances. The implementation of closed loop control provides an opportunity for further research as discussed in the next chapter.

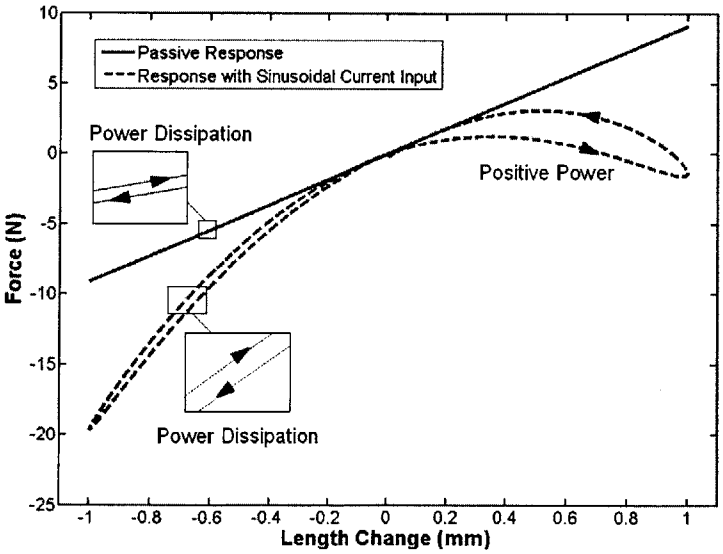

Figure 5-9: Work Loops for PPy Actuator Using Zero and Non-Zero Current Inputs

Figure 5-9 shows that, in the absence of control input, the actuator responds to length changes by storing elastic potential energy as it follows a linear trajectory. Because of the viscous damping term, however, the work loop has a small finite width and is traversed in a clockwise sense. When a sinusoidal current input $i(t)$ is applied, the work loop morphology changes dramatically to the dashed line in Figure 5-9. Specifically, during the first part of the cycle, the current input forces the actuator to be increasingly stiff and dissipative as evidenced by the larger slope and loop width respectively. In the last past of the cycle (dashed curve in upper right hand corner of Figure 5-9), the actuator is producing power in excess of what was dissipated previously.

5.5 References

[1] Hogan N., "Impedance control: An approach to manipulation: Part I, Part II, Part III", *J. Dynam. Syst., Measurement, Contr.—Trans. ASME*, Vol 107, pp. 1–24, 1985.

[2] Dickinson M., et. al., "How Animals Move", *Science*, Vol 288, pp. 100-106, 2000.

[3] Gefen A., Megido-Ravid M., Itzchak Y., and Arcan M., "Biomechanical Analysis of the Three-Dimensional Foot Structure During Gait: A Basic Tool for Clinical Applications", *Journal of Biomechanical Engineering*, Vol 124, pp. 630-639, 2002.

[4] Salathe E. and Arangio G., "A Biomechanical Model of the Foot: The Role of Muscles, Tendons, and Ligaments", *Journal of Biomechanical Engineering,* Vol 122, pp. 281-287, 2000.

[5] Asada H. and Slotine J., *Robot Analysis and Control*, New York: Wiley, 1986.

Chapter 6
Conclusions

6.1 Conclusions

The primary objective of this research was to investigate multilayer PPy linear actuators from a bio-robotics perspective. Three of the major research thrusts were modeling, identification, and application of multilayer PPy actuators. The research presented in this thesis provides the necessary groundwork for practical use of PPy actuators. Pragmatically, a low order model of PPy actuators is needed to make design decisions and to create an effective feedback controller. The identification of model parameters in real-time can greatly extend the lifetime of a polymer actuator. And, the design of a humanoid foot illustrates a unique application that utilizes the inherent characteristics of PPy actuators.

This thesis takes a step beyond the contemporary literature that focuses primarily on single films and material optimization to the new realm of systems level research that will use PPy actuators in robotics, control, and instrumentation applications. A more specific recapitulation of the main objectives and outcomes of this thesis is contained in Sections 6.1.1 to 6.1.3.

6.1.1 Modeling of Polypyrrole Actuators

Two modeling approaches were used in this thesis: grey box and black box. The first approach was grey box modeling. A first order RC electrical model and a second order spring-dashpot mechanical model were presented and experimentally validated for multilayer actuators. A unidirectional coupling from the electrical to the mechanical domain was assumed where charge was directly proportional to the elongation of the film analogous to the results found in [1] and [2]. The grey box model was constructed based on physically motivated phenomenological descriptions of polymer charging and viscoelastic behavior. Equations 3.5 to 3.8 provide the quantitative relations used in the grey box model.

The black box modeling of PPy actuators was accomplished by assuming the general Box-Jenkins discrete transfer function structure. Models within this structure (for example ARX) were identified. Ultimately, it was determined that the most general Box-Jenkins form wherein all discrete poles and zeros were unique provided the best description of the actuator behavior. Quantitatively, the Akaike Information Criterion (AIC) was minimized using a third-order Box-Jenkins Structure. Equations 3.14 and 3.15 provide the quantitative relations used in the black box model.

In sum, the black box model of PPy actuators is most appropriate when online identification is to be performed. This black box approach is also desirable offline because model parameters are readily obtained from input data using the System Identification Toolbox available for Matlab. On the other hand, the grey box model is useful when physical insight is desired. This model is also useful for continuous time controller design. Simplification of the grey box mechanical behavior to a Maxwell unit allows for mathematically tractable compliance and damping analysis of structures utilizing PPy actuators.

6.1.2 Impedance Identification of Polypyrrole

In order to slow the degradation of PPy actuators, a method of online impedance identification and voltage de-rating was developed. The identification of electrical impedance while the system is operating provides a method for monitoring the degradation state of an actuator. The degradation state can be expressed as a percentage increase from the reference impedance value when the actuator begins its electrical cycling. The identification of impedance using LS and RLS was shown in Chapter 4. Voltage saturation limits that are decreased based on the degradation state can also be used. The aforementioned technique is shown in Figures 4-2 and 4-3 for a galvanostat current input.

The ultimate goal of artificial muscles is to provide repeatable, forceful, and large stroke contraction and thus the artificial muscle material will be driven to its performance extremes. The impedance identification technique presented in this thesis is

ideally suited for actuators that will be used repetitively. The degradation strategy presented in this work can be generalized to include any actuator material that 1) has a degradation metric that can be identified online and 2) has a counteracting mechanism that can slow degradation.

6.1.3 Application of PPy Actuators to a Humanoid Foot

In current literature, use of the inherent mechanical stiffness and damping properties of smart materials has been to actively control structural vibrations. In particular, most research utilizes PZT actuators to achieve desirable vibration isolation in aerospace structures. For this research, the humanoid foot was chosen from a host of possible applications because it is a challenging robotic system that is not well suited to traditional electrochemical actuators. An effective humanoid foot using smart material has far-reaching implications in biped robot agility as well as advanced prosthetics.

The humanoid foot and leg assembly were created using SolidWorks and then physically realized using a Dimension SST fuse deposition rapid prototyping machine. The design was analyzed in terms of compliance and damping to externally applied forces. Antagonistically paired PPy actuators serve as multifunctional muscles in the system. A low-order Maxwell model of PPy actuators was validated experimentally and shown to provide a simple means for compliance and damping analysis of any structure involving PPy actuators.

6.2 Future Work

Several opportunities exist to extend the work presented in this thesis. In general, there are two parallel paths that PPy research may take: materials science improvements and system level applications. The first path of research must work towards overcoming the current actuator limitations as outlined in Section 1.4. The second path of research is to focus on effective control and application of PPy actuators to engineering systems despite the actuators' limitations. This thesis focused on the second path of research.

The modeling of PPy actuators has been extensively treated. However, further data validation using several actuators and a wider variety of force inputs would serve as a natural and useful extension of the results Chapter 3. The system identification presented in Chapters 3 and 4 could also be bolstered with a wider variety inputs time series than those offered. The largest opportunity for future work involves the general study of multifunctional actuator materials. The multifunctional nature, as discussed in Chapter 5, was utilized in the design of a humanoid foot. Additional work in this area should relax the infinite inertia assumption of the compliance and stiffness model. Also, the testing and design optimization of the humanoid foot presents an empirically rich area of robotics research. The humanoid foot, however, is only one of myriad possible applications of a multifunctional muscle material. Moreover, strategies for assigning and following work loops with artificial muscles provides intriguing feedback and feedforward control challenges. Such challenges form an analytically rich horizon of robotics research.

6.3 References

[1] Madden, John D. W., *Conducting Polymer Actuators*, Ph.D. Thesis, MIT, Cambridge, MA, 2000.

[2] Della Santa A., De Rossi D., Mazzolidi A., "Characterization and modeling of a conducting polymer muscle-like linear actuator", *Smart Materials and Structures*, Vol 6, pp. 23-24, 1997.

Appendix A
Selected Matlab Files

A1: Experimental Apparatus

```
% FORCE CONTROLLER DESIGN
% This M File is for the design of the PPy Actuator Testing Apparatus
% 6-23-06

% CLEAR SCREEN, ETC.
%--------------------------------------------------------------------------
clc
clear all
close all
%--------------------------------------------------------------------------


% INPUT MODEL AND SYSTEM PARAMETERS
%--------------------------------------------------------------------------
                    %All Units are MKS
R = 3;              %Winding Resistance
Rs = 0;             %Sense Resistor Resistance
L = 1e-3;           %Coil Inductance
K = 3.9;            %Force Constant/Back EMF Constant
b2 = 2300;          %Viscoelastic Damping Constant
k2 = 300;           %Viscoelastic Elastic Constant
k1 = 3860;          %Viscoelastic Elastic Constant
m = 0.03;           %Moving Mass
bvc = 6;            %Damping in Voice Coil Slide Motion (includes potentiometer, etc.)

s = tf('s');
fc = 100;            %Force Signal Filter Cutoff Frequency (1st Order Butterworth)
tau = 1/(2*pi*fc);
Fs = 30;           % Sampling Frequency in Hertz
Ts = 1/Fs;          % Sampling Period in seconds
%--------------------------------------------------------------------------


% DEFINE TRANSFER FUNCTIONS
%--------------------------------------------------------------------------
%Gp = K/(R+Rs+s*L+(K^2*s*(b2*s+k2))/((k1+bvc*s+m*s^2)*(b2*s+k2)+b2*k2*s)); % Plant F(s)/V(s)
Gp = (K/R)/((L/R)*s+1);
Gpwd = Gp*(2/Ts)/(s+(2/Ts)); % Plant w. ZOH approximation
H = 1/(tau*s+1); % Force Signal Filter
U_L = Gpwd*H; % Uncompensated Loop Transfer Function
Kp = 15;%24.55;
Gc = Kp*(0.002*s+1)/s; % Controller Transfer Function
L = Gc*U_L;
GCL = feedback(Gpwd*Gc,H); % Closed Loop Transfer Function F(s)/R(s)

% figure
% bode(U_L)
% set(gcf,'name','L(s) - Uncompenstated');
% figure
% margin(L)
% set(gcf,'name','L(s) - Compenstated');
% figure
% bode(GCL)
% set(gcf,'name','F(s)/R(s)');

figure
bode(U_L)
hold on
margin(L)
```

```
legend('Uncompensated Loop TF: G(s) = 1','Compensated Loop TF: G(s) = PI Controller')
figure
bode(GCL)
set(gcf,'name','F(s)/R(s)');

%--------------------------------------------------------------------------


% % SIMULINK SIMULATION - CONTINUOUS
% %-------------------------------------------------------------------------
% Nc = get(Gc,'num');
% Nc = Nc{[1]};
% Dc = get(Gc,'den');
% Dc = Dc{[1]};
%
% Np = get(Gp,'num');
% Np = Np{[1]};
% Dp = get(Gp,'den');
% Dp = Dp{[1]};
%
% tStop = 10;
%
% sim('Force_Loop');
% figure
% set(gcf,'name','SIMULINK SIMULATION OUTPUT')
% %subplot(2,1,1)
% plot(t,V,'LineWidth',2)
% xlabel('Time (s)')
% ylabel('Control Voltage (V)')
%
% %subplot(2,1,2)
% figure
% plot(t,F)
% hold on
% plot(t,R,'--k','LineWidth',2)
% legend('Load Cell Output','Reference')
% xlabel('Time (s)')
% ylabel('Force (N)')
% %-------------------------------------------------------------------------

% SIMULINK SIMULATION - DISCRETE
%--------------------------------------------------------------------------
clear V t F R
Fs_str = num2str(Fs);
Title = ['DISCRETE SIMULINK SIMULATION OUTPUT (Fs = ' Fs_str ' Hz)'];
Gc_D = c2d(Gc,Ts,'tustin') % Obtain Discrete Controller

Nc_D = get(Gc_D,'num');
Nc_D = Nc_D{[1]};
Dc_D = get(Gc_D,'den');
Dc_D = Dc_D{[1]};

Np = get(Gp,'num');
Np = Np{[1]};
Dp = get(Gp,'den');
Dp = Dp{[1]};

tStop = 10;

sim('Force_Loop_Discrete');
figure
set(gcf,'name',Title)
subplot(2,1,1)
plot(t_sampled,V,'LineWidth',2)
xlabel('Time (s)')
ylabel('Control Voltage (V)')

subplot(2,1,2)
plot(t,F)
hold on
```

```
plot(t,R,'--k','LineWidth',2)
legend('Load Cell Output','Reference')
xlabel('Time (s)')
ylabel('Force (N)')
%--------------------------------------------------------------------------
```

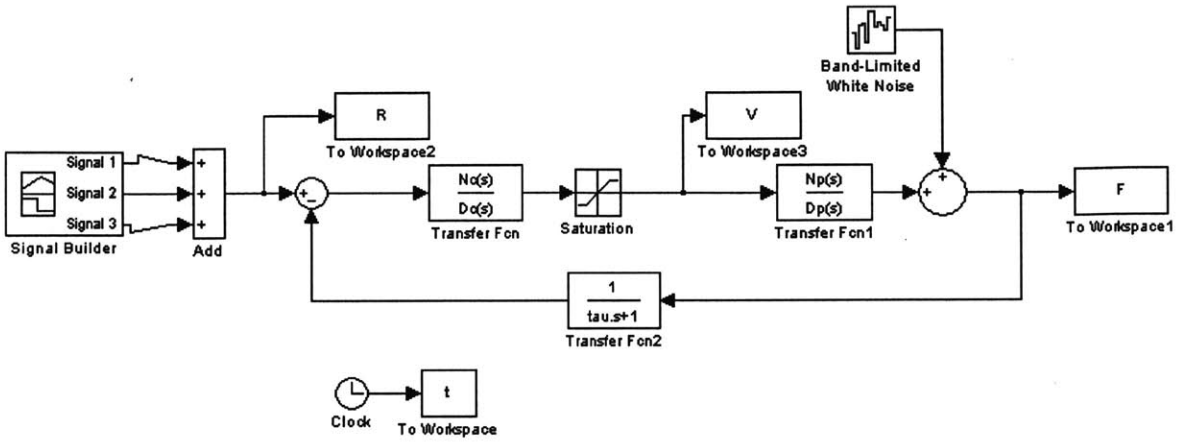

Figure A1: DMA Test Stand Simulink Diagram for Simulation of Force Controller Performance

A2: Lumped Parameter Modeling of Polypyrrole Multilayer Actuators

```
% M FILE FOR SIMULATING VISCOELASTIC MODEL: KELVIN IN SERIES W. MAXWELL
% CLEAR SCREEN, ETC.
%--------------------------------------------------------------------------
clc
close all
clear
%--------------------------------------------------------------------------


% DEFINE PARAMETERS AND CREATE INPUT
%--------------------------------------------------------------------------
k2 = 3190;
b2 = 0.76;
k1 = 1;
b1 = 0.02;
t = 0:0.001:60;
F = 1.5*[zeros(1,10000) ones(1,30000) zeros(1,20001)];
%--------------------------------------------------------------------------


% CREATE TF AND SIMULATE RESPONSE
%--------------------------------------------------------------------------
s = tf('s');
H = (b1*b2*s^2+(k2*b2+k1*b2+k2*b1)*s+k1*k2)/(b1*b2*k2*s^2+k1*k2*b2*s);
y = lsim(H,F,t);
plot(t,y)
xlabel('Time (s)');
ylabel('Displacement');
%--------------------------------------------------------------------------
```

```
% M FILE TO IDENTIFY THE PARAMETERS OF THE PPY ELECTRICAL MODEL
% CLEAR WORKSPACE, ETC.
%-----------------------------------------------------------------
clear all; close all; clc;
%-----------------------------------------------------------------


% LOAD DATA FOR ELECTRICAL ID DEPENDING ON LOAD
%-----------------------------------------------------------------
dataFileNum =  input('Enter Actuator Number (106,108,114): ');

switch dataFileNum
    case 106
        data = load('106_Electrical_ID.txt');
        force = input('Enter Load: (1,2,3 N, 4 = all data): ');
        Fs = 100;

        switch force
            case 1
                nStart = 2063;
                nEnd = 3240;
                F = data(nStart:nEnd,1);
                R = data(nStart:nEnd,2);
                I = data(nStart:nEnd,3);
                V = data(nStart:nEnd,4);
                X = data(nStart:nEnd,5);
                t = 0:0.01:(length(X)-1)*.01;
            case 2
                nStart = 3260;
                nEnd = 4510;
                F = data(nStart:nEnd,1);
                R = data(nStart:nEnd,2);
                I = data(nStart:nEnd,3);
                V = data(nStart:nEnd,4);
                X = data(nStart:nEnd,5);
                t = 0:0.01:(length(X)-1)*.01;
            case 3
                nStart = 4525;
                nEnd = 6345;
                F = data(nStart:nEnd,1);
                R = data(nStart:nEnd,2);
                I = data(nStart:nEnd,3);
                V = data(nStart:nEnd,4);
                X = data(nStart:nEnd,5);
                t = 0:0.01:(length(X)-1)*.01;
            case 4
                nStart = 2063;
                nEnd = 6345;
                F = data(nStart:nEnd,1);
                R = data(nStart:nEnd,2);
                I = data(nStart:nEnd,3);
                V = data(nStart:nEnd,4);
                X = data(nStart:nEnd,5);
                t = 0:0.01:(length(X)-1)*.01;
        end

    case 108
        data = load('108_Electrical_ID.txt');
        force = input('Enter Load: (1,2,3 N, 4 = all data): ');
        Fs = 50;

        switch force
            case 1
                nStart = 1580;
                nEnd = 3250;
                F = data(nStart:nEnd,1);
                R = data(nStart:nEnd,2);
                I = data(nStart:nEnd,3);
                V = data(nStart:nEnd,4);
                X = data(nStart:nEnd,5);
                t = 0:0.02:(length(X)-1)*.02;
```

```
        case 2
            nStart = 3275;
            nEnd = 4350;
            F = data(nStart:nEnd,1);
            R = data(nStart:nEnd,2);
            I = data(nStart:nEnd,3);
            V = data(nStart:nEnd,4);
            X = data(nStart:nEnd,5);
            t = 0:0.02:(length(X)-1)*.02;
        case 3
            nStart = 4375;
            nEnd = 5560;
            F = data(nStart:nEnd,1);
            R = data(nStart:nEnd,2);
            I = data(nStart:nEnd,3);
            V = data(nStart:nEnd,4);
            X = data(nStart:nEnd,5);
            t = 0:0.02:(length(X)-1)*.02;
        case 4
            nStart = 1580;
            nEnd = 5560;
            F = data(nStart:nEnd,1);
            R = data(nStart:nEnd,2);
            I = data(nStart:nEnd,3);
            V = data(nStart:nEnd,4);
            X = data(nStart:nEnd,5);
            t = 0:0.02:(length(X)-1)*.02;
    end

case 114
    data = load('114_Electrical_ID.txt');
    force = input('Enter Load: (1,2,3 N, 4 = all data): ');
    Fs = 50;

    switch force
        case 1
            nStart = 1525;
            nEnd = 2980;
            F = data(nStart:nEnd,1);
            R = data(nStart:nEnd,2);
            I = data(nStart:nEnd,3);
            V = data(nStart:nEnd,4);
            X = data(nStart:nEnd,5);
            t = 0:0.02:(length(X)-1)*.02;
        case 2
            nStart = 3034;
            nEnd = 3910;
            F = data(nStart:nEnd,1);
            R = data(nStart:nEnd,2);
            I = data(nStart:nEnd,3);
            V = data(nStart:nEnd,4);
            X = data(nStart:nEnd,5);
            t = 0:0.02:(length(X)-1)*.02;
        case 3
            nStart = 4760;
            nEnd = 6610;
            F = data(nStart:nEnd,1);
            R = data(nStart:nEnd,2);
            I = data(nStart:nEnd,3);
            V = data(nStart:nEnd,4);
            X = data(nStart:nEnd,5);
            t = 0:0.02:(length(X)-1)*.02;
        case 4
            nStart = 1525;
            nEnd = 6610;
            F = data(nStart:nEnd,1);
            R = data(nStart:nEnd,2);
            I = data(nStart:nEnd,3);
            V = data(nStart:nEnd,4);
            X = data(nStart:nEnd,5);
            t = 0:0.02:(length(X)-1)*.02;
```

```
        end
end
%-------------------------------------------------------------------


% INITIALIZE ID TERMS
%-------------------------------------------------------------------
phi = [-V(1); I(2); I(1)];
beta = V(2)*phi;
%-------------------------------------------------------------------


% FORM LLSE ID MATRICES VECTOR AND IDENTIFY MODEL
%-------------------------------------------------------------------
for i = 3:(length(V))
    zeta = [-V(i-1) I(i) I(i-1)];
    phi  = [phi zeta'];
    beta = beta + V(i)*zeta';
end

Rn = phi*phi';
Rn_rank = rank(Rn);
if Rn_rank < 3
    error('Rank of Rn is too small')
end

theta = inv(Rn)*beta;

a = theta(1)
b0 = theta(2)
b1 = theta(3)
realTheta = convertCircuitParameters(theta, Fs)
%-------------------------------------------------------------------------


% USE IDENTIFIED MODEL TO ESTIMATE THE OUTPUT AND EVALUATE THE PERFORMANCE
%-------------------------------------------------------------------------
R1 = realTheta(1);
R2 = realTheta(2);
C = realTheta(3);
s = tf('s');
H = (R2+R1*R2*C*s)/(1+(R1+R2)*C*s);
num = get(H,'num');
num = num{1};
den = get(H,'den');
den = den{1};
[a,b,c,d] = tf2ss(num,den);
sys = ss(a,b,c,d);

%Vppy_Est = phi'*theta;
Vppy_Est = lsim(sys,I,t,V(1)-0.2);
Vppy_Est = Vppy_Est;
Vppy_True = V;
Is_True = I;
tplot = t;

DataFit = 100*(1-(norm(Vppy_Est-Vppy_True)/norm(Vppy_True-mean(Vppy_True))))


%-------------------------------------------------------------------------


% PLOT OUTPUT
%-------------------------------------------------------------------------
figure;
plot(tplot, Vppy_True,'b.', tplot, Vppy_Est,'k','LineWidth',3)
legend('Measured Voltage','Model Output');
xlabel('Time (sec)')
ylabel('Voltage (volts)')
%-------------------------------------------------------------------------
```

```
% MATLAB FUNCTION TO CONVERT ID'ED CIRCUIT PARAMETERS TO THEIR REAL SYSTEM COUNTERPARTS.
function realTheta = convertCircuitParameters(theta, Fs)

% USER DEFINED PARAMETERS
%----------------------------------------------------------------
a  = theta(1);
b0 = theta(2);
b1 = theta(3);

% CALCULATE PARAMETERS
%----------------------------------------------------------------
T = 1/Fs;
c = (2/T);

R2 = (b0 + b1)/(1+a);

tau1 = (b0-b1)/(c*(1 + a));
tau2 = (1-a)/(c*(1 + a));

R1 = (tau1*R2)/(tau2*R2 - tau1);
C = (tau1)/(R1*R2);

realTheta = [R1 R2 C];
%----------------------------------------------------------------
```

A3: Monitoring and Preventing Actuator Degradation

```
% M FILE FOR IMPEDANCE IDENTIFICATION USING LEAST SQUARES AND ACTUATOR FAILURE TEST
% CLEAR SCREEN AND WORKSPACE
%%%%%%%%%%%%%%%%%%%%%%%%%%%%%%%%%%%%%%%%%%%%%%%%%%%%%%%%%%%%%%%%%%%%%%%%%%%%
clc
clear
close all
%%%%%%%%%%%%%%%%%%%%%%%%%%%%%%%%%%%%%%%%%%%%%%%%%%%%%%%%%%%%%%%%%%%%%%%%%%%%

% READ IN DATA AND FORM VECTORS
%%%%%%%%%%%%%%%%%%%%%%%%%%%%%%%%%%%%%%%%%%%%%%%%%%%%%%%%%%%%%%%%%%%%%%%%%%%%
dt = 0.1;
nStart = 16100;
nStop = 1.8485e5;

data = load('135 RLS Degrade Current 4-13-06.txt');
t = 0:dt:(nStop-nStart)*dt;
t = t';
X = data(nStart:nStop,4);
V = data(nStart:nStop,5);
I = data(nStart:nStop,6);
%%%%%%%%%%%%%%%%%%%%%%%%%%%%%%%%%%%%%%%%%%%%%%%%%%%%%%%%%%%%%%%%%%%%%%%%%%%%


% FORM LEAST SQUARES ESTIMATES OF R1, R2, and C FOR EACH DATA WINDOW
%%%%%%%%%%%%%%%%%%%%%%%%%%%%%%%%%%%%%%%%%%%%%%%%%%%%%%%%%%%%%%%%%%%%%%%%%%%%

Pinv = zeros(3,3);
B = zeros(3,1);
nWindowStart = 1;
k = 1;
w = 0.628; % Approximate angular frequency for impedance calculation

while nWindowStart < (length(I) - 1001)
    for j = 0:999
    phi(:,j+1) = [-V(nWindowStart+j) I(nWindowStart+j+1) I(nWindowStart+j)]';
    Pinv = Pinv + phi(:,j+1)*phi(:,j+1)';
    B = B + V(nWindowStart+j+1)*phi(:,j+1);
    end
```

```
    theta = (Pinv^-1)*B;
    Vfit{k} = phi'*theta;
    Vact{k} = V(nWindowStart:(nWindowStart+999));
    DataFit(k) = 100*(1-(norm(Vact{k}(:,1)-Vfit{k}(:,1))/norm(Vfit{k}(:,1)-mean(Vfit{k}(:,1)))));

    a = theta(1);
    bo = theta(2);
    b1 = theta(3);

    R1(k) = (-(bo+b1)*(bo-b1))/(2*(a*bo-b1));
    R2(k) = (bo+b1)/(1+a);
    C(k)  = (-(a*bo-b1)*dt)/(bo+b1)^2;
    Z(k) = sqrt((R1(k)*R2(k)*C(k)*w)^2+R2(k)^2)/sqrt(((R1(k)+R2(k))*C(k)*w)^2+1);

    tImpedancePlot(k) = 100*k;
    nWindowStart = nWindowStart + 1000;
    k = k+1;
end


clear data dt nStart nStop nWindowStart tau1 tau2 a b0 b1 theta w j k phi c B Pinv
%%%%%%%%%%%%%%%%%%%%%%%%%%%%%%%%%%%%%%%%%%%%%%%%%%%%%%%%%%%%%%%%%%%%%%%%%%%%%%%


% PLOT RESULTS
%%%%%%%%%%%%%%%%%%%%%%%%%%%%%%%%%%%%%%%%%%%%%%%%%%%%%%%%%%%%%%%%%%%%%%%%%%%%%%%
figure(1)
set(gcf,'name','RESISTANCES AND CAPACITANCE')
subplot(3,1,1)
plot(tImpedancePlot,R1)
xlabel('Time(s)')
ylabel('R_1 Ohms')

subplot(3,1,2)
plot(tImpedancePlot,R2)
xlabel('Time(s)')
ylabel('R_2 Ohms')

subplot(3,1,3)
plot(tImpedancePlot,C)
xlabel('Time(s)')
ylabel('C Farads')

figure(2)
set(gcf,'name','IMPEDANCE')
plot(tImpedancePlot,Z)
xlabel('Time(s)')
ylabel('Impedance')
%%%%%%%%%%%%%%%%%%%%%%%%%%%%%%%%%%%%%%%%%%%%%%%%%%%%%%%%%%%%%%%%%%%%%%%%%%%%%%%

% CREATE PLOT OF ELECTRICAL MODEL FIT FOR BEGINNING 300 DATA POINTS
%%%%%%%%%%%%%%%%%%%%%%%%%%%%%%%%%%%%%%%%%%%%%%%%%%%%%%%%%%%%%%%%%%%%%%%%%%%%%%%
r1 = R1(1);
r2 = R2(1);
c = C(1);
s = tf('s');
t1 = t(1:300);
v1 = V(1:300);
i1 = I(1:300);
TF = (r1*r2*c*s+r2)/((r1+r2)*c*s+1);
vsim = lsim(TF,I(1:300),t1);
figure
subplot(2,1,1)
plot(t1,i1,'k');
xlabel('Time(s)');
ylabel('Input Current (A)')
subplot(2,1,2)
plot(t1,v1,'.');
hold on
plot(t1,vsim,'k')
xlabel('Time(s)')
```

```
ylabel('Voltage (V)')
legend('Measured','Model')
%%%%%%%%%%%%%%%%%%%%%%%%%%%%%%%%%%%%%%%%%%%%%%%%%%%%%%%%%%%%%%%%%%%%%%%%%%%
```

```
% M FILE FOR IMPEDANCE SELECTION OF RLS FORGETTING FACTOR
% CLEAR SCREEN AND WORKSPACE
%-----------------------------------------------------------------------------------
clc
close all
clear

eps = input('Enter in % contribution of data point after forgetting time has expired: ');
fsamp1 = input('Enter in Sampling Frequency in Hz: ');
tsamp1 = 1/fsamp1;
tmax = (log10(eps)-2)/(log10(0.99))*tsamp1;

for j = 0:tmax
    alpha1(j+1) = 10^((log10(eps)-2)*(tsamp1/(j+1)));
end

plot(0:tmax,alpha1);
xlabel('Desired Forgetting Time (seconds)')
ylabel('RLS Forgetting Factor (alpha)')
```

```
% M-FILE FOR RECURSIVE LEASE SQUARES CIRCUIT ID

% CLEAR SCREEN AND WORKSPACE
%%%%%%%%%%%%%%%%%%%%%%%%%%%%%%%%%%%%%%%%%%%%%%%%%%%%%%%%%%%%%%%%%%%%%%%%%%%%%%%%%%%%%%%%%%%%%%%
clc
close all
clear
%%%%%%%%%%%%%%%%%%%%%%%%%%%%%%%%%%%%%%%%%%%%%%%%%%%%%%%%%%%%%%%%%%%%%%%%%%%%%%%%%%%%%%%%%%%%%%%


% LOAD IN DATA
%%%%%%%%%%%%%%%%%%%%%%%%%%%%%%%%%%%%%%%%%%%%%%%%%%%%%%%%%%%%%%%%%%%%%%%%%%%%%%%%%%%%%%%%%%%%%%%
data = load('ID_#106_11_17_05_150g.txt');
Vppy = data(:,2);
Ippy = data(:,3);
%%%%%%%%%%%%%%%%%%%%%%%%%%%%%%%%%%%%%%%%%%%%%%%%%%%%%%%%%%%%%%%%%%%%%%%%%%%%%%%%%%%%%%%%%%%%%%%


% SET INITIAL CONDITIONS AND ALPHA FORGETTING FACTOR
%%%%%%%%%%%%%%%%%%%%%%%%%%%%%%%%%%%%%%%%%%%%%%%%%%%%%%%%%%%%%%%%%%%%%%%%%%%%%%%%%%%%%%%%%%%%%%%
% Initialize Parameter Estimate
theta_h = zeros(3,1);

% Initialize P matrix
Pt = eye(3);

% Set forgetting factor
alpha = .91;  %corresponds to approximately 10 seconds
%%%%%%%%%%%%%%%%%%%%%%%%%%%%%%%%%%%%%%%%%%%%%%%%%%%%%%%%%%%%%%%%%%%%%%%%%%%%%%%%%%%%%%%%%%%%%%%


% RLS LOOP
%%%%%%%%%%%%%%%%%%%%%%%%%%%%%%%%%%%%%%%%%%%%%%%%%%%%%%%%%%%%%%%%%%%%%%%%%%%%%%%%%%%%%%%%%%%%%%%
for t = 2:length(Vppy)

    % Set phi
     phi = [-Vppy(t-1) Ippy(t) Ippy(t-1)]';


    %Compute Theta Hat
    theta_h = theta_h + (Pt*phi/(alpha + phi'*Pt*phi))*(Vppy(t)-phi'*theta_h);

    % Revise Pt matrix
```

```
    Pt = (1/alpha)*(Pt - (Pt*phi*phi'*Pt/(alpha + phi'*Pt*phi)));

    % Compute Circuit Parameters
    a = theta_h(1);
    bo = theta_h(2);
    b1 = theta_h(3);
    R1(t) = (-(bo+b1)*(bo-b1))/(2*(a*bo-b1));
    R2(t) = (bo+b1)/(1+a);
    C(t)  = (-(a*bo-b1)*0.1)/(bo+b1)^2;

    % Reset Covariance Matrix to Identity Every 10s
    if mod(t,100)== 0,
        Pt = eye(3);
    end


end
%%%%%%%%%%%%%%%%%%%%%%%%%%%%%%%%%%%%%%%%%%%%%%%%%%%%%%%%%%%%%%%%%%%%%%%%%%%%%%%%%%%%%%%%%%%%%%%%%


% CREATE PLOT
%%%%%%%%%%%%%%%%%%%%%%%%%%%%%%%%%%%%%%%%%%%%%%%%%%%%%%%%%%%%%%%%%%%%%%%%%%%%%%%%%%%%%%%%%%%%%%%%%
subplot(3,1,1)
plot([1:length(R1)]*.1,R1,'r','LineWidth',2)
grid on
xlabel('Time (s)');
ylabel('R_1 (ohms)');
axis([20 160 1 4.5])

subplot(3,1,2)
plot([1:length(R2)]*.1,R2,'r','LineWidth',2)
grid on
xlabel('Time (s)');
ylabel('R_2 (ohms)');
axis([20 160 0.5 2])

subplot(3,1,3)
plot([1:length(C)]*.1,C,'b','LineWidth',2)
grid on
xlabel('Time (s)');
ylabel('C (Farads)');
axis([20 160 0 1])
%%%%%%%%%%%%%%%%%%%%%%%%%%%%%%%%%%%%%%%%%%%%%%%%%%%%%%%%%%%%%%%%%%%%%%%%%%%%%%%%%%%%%%%%%%%%%%%%%
```

A4: Application of Polypyrrole Actuators to a Humanoid Foot

```
% M-FILE FOR COMPUTATION OF FORCE VERSUS LENGTH CHARACTERISTICS FOR PPY ACTUATORS IN
% ANTHROPOMORPHIC FOOT

% CLEAR SCREEN, ETC----------------------------------------------------------
clear
clc
close all
%----------------------------------------------------------------------------


% DEFINE NECESSARY CONSTANTS ------------------------------------------------
l1 = 2.00;
l2 = 2.46;
l3 = 0.93;
Bpf = 49.03; Bpf = Bpf*(pi/180);
Bdf = 30.896; Bdf = Bdf*(pi/180);
Bp = 10.075; Bp = Bp*(pi/180);
lopo = 3.67;
```

```
loan = 3.84;
lodo = 4.46;
lopl = 5.48;
gampo = 12.901; gampo = gampo*(pi/180);
gaman = 6.126; gaman = gaman*(pi/180);
gamdo = 15.064; gamdo = gamdo*(pi/180);
rpo = 1.64;
ran = 0.71;
rdo = 0.91;
rpl = 0.64;
Bpo = 57.66; Bpo = Bpo*(pi/180);
Ban = 50.71; Ban = Ban*(pi/180);
%-------------------------------------------------------------------------

%Form Joint to Cartesian Jacobian
Jth_x = zeros(2,3);
Jth_x(1,1) = -l1*sin(Bpf)-l2*sin(Bpf+Bdf)-l3;
Jth_x(2,1) = -l1*cos(Bpf)-l2*sin(Bpf+Bdf);
Jth_x(1,2) = l2*sin(Bpf+Bdf)-l3;
Jth_x(2,2) = -l2*sin(Bpf+Bdf);
Jth_x(1,3) = -l3;
Jth_x(2,3) = 0;

%Form Actuator to Joint Jacobian
J = zeros(3,4);
L = [loan,lopo,lodo,lopl+0.0001]';
J(2,3) = -0.001;
J(2,4) = 0.001;
J(1,1) = -2*L(1)/sqrt( (2*L(1)*ran*sin(Ban-gaman))^2+4*ran^2*(loan^2-L(1)^2) );
J(1,2) = 2*L(2)/sqrt( (2*L(2)*rpo*sin(gampo-Bpo))^2+4*rpo^2*(lopo^2-L(2)^2) );
J(3,3) = -2*L(3)/sqrt( (2*L(3)*rdo*sin(gamdo))^2+4*rdo^2*(lodo^2-L(3)^2) );
J(3,4) = L(4)*rpl/sqrt(L(4)^2-lopl^2);

%Form actuator stiffness matrix
k = 9.1 % N/mm
Kl = k^-1*eye(4);

%Form actuator damping matrix
b = 1700 % N-s/mm
Dl = b*eye(4);

%Form Cartesian Compliance Matrix
Kx = Jth_x*(J*Kl*J')*Jth_x'

%Form Cartesian Damping Matrix
Dx = Jth_x*(J*Dl*J')*Jth_x'


% M-FILE FOR COMPUTATION OF FORCE VERSUS LENGTH CHARACTERISTICS FOR PPY ACTUATORS IN
% ANTHROPOMORPHIC FOOT

% CLEAR SCREEN, ETC-----------------------------------------------------------
clear
clc
close all
%-------------------------------------------------------------------------


% DEFINE NECESSARY CONSTANTS -------------------------------------------------
l11 = 2.00;
l22 = 2.46;
l13 = 0.93;
Bpf = 49.03; Bpf = Bpf*(pi/180);
Bdf = 30.896; Bdf = Bdf*(pi/180);
Bp = 10.075; Bp = Bp*(pi/180);
lopo = 3.67;
loan = 3.84;
lodo = 4.46;
lopl = 5.48;
gampo = 12.901; gampo = gampo*(pi/180);
```

```
gaman = 6.126; gaman = gaman*(pi/180);
gamdo = 15.064; gamdo = gamdo*(pi/180);
rpo = 1.64;
ran = 0.71;
rdo = 0.91;
rpl = 0.64;
Bpo = 57.66; Bpo = Bpo*(pi/180);
Ban = 50.71; Ban = Ban*(pi/180);
%-------------------------------------------------------------------------


% FORM LENGTH INPUTS, TIME STEP, AND TIME-------------------------------
dt = 0.0001;
T = 1;
t = 0:dt:T;

lan_max = 1;
lpo_max = 1;
ldo_max = 1;
lpl_max = 1;

lan_t = -lan_max*sin(2*pi*t/T);
lpo_t = lpo_max*sin(2*pi*t/T);
ldo_t = -ldo_max*sin(2*pi*t/T)-ldo_max;
lpl_t = lpl_max*sin(2*pi*t/T)+lpl_max;

dT_lan_t = -(2*pi/T)*lan_max*cos(2*pi*t/T);
dT_lpo_t = (2*pi/T)*lpo_max*cos(2*pi*t/T);
dT_ldo_t = -(2*pi/T)*ldo_max*cos(2*pi*t/T);
dT_lpl_t = (2*pi/T)*lpl_max*cos(2*pi*t/T);

b = 1700; %N-s/mm
k = 9.1; %N/mm
alpha = 5; %mm/C
s = tf('s');
H = k*b/(b*s+k);
G = alpha*k*b/(b*s+k);

Imax = 1.5;
I_t = Imax*sin(4.1*pi*t);

FXan = lsim(H,dT_lan_t,t);
FXpo = lsim(H,dT_lpo_t,t);
FXdo = lsim(H,dT_ldo_t,t);
FXpl = lsim(H,dT_lpl_t,t);

FQan = lsim(G,I_t,t);

Fan = FXan-FQan;


figure
plot(lan_t,FXan,'r','LineWidth',2)
hold on
plot(lan_t,Fan,'b--','LineWidth',2)
xlabel('Length Change (mm)')
ylabel('Force (N)')
axis([-1.1,1.1,-25,10])
legend('Passive Response','Response with Sinusoidal Current Input')



% M-FILE TO PLOT VISCOELASTIC DATA FROM FORCE CONTROL APPARATUS

% CLEAR SCREEN, ETC.
%-------------------------------------------------------------------------
clc
clear
close all
%-------------------------------------------------------------------------
```

```
% LOAD DATA AND PLOT
%-------------------------------------------------------------------------
data = load('Viscoelasticity_Data_114.txt');
F = data(:,1);
F = BandPrefilter(F, 32, 0.01, 40);
X = data(:,3);
X = BandPrefilter(X, 32, 0.1, 40);

tfitStart = 45*40;
tfitEnd = length(X)-1800;

Ffit = F(tfitStart:tfitEnd);
Xfit = X(tfitStart:tfitEnd);
tfit = 0:(1/40):(length(Xfit)-1)*(1/40);



dt = 1/40; % Sampling Period
t = 0:dt:(length(X)-1)*dt;

figure
subplot(2,1,1)
plot(t,F,'LineWidth',2)
xlabel('Time (s)')
ylabel('Force (N)')
subplot(2,1,2)
plot(t,X,'LineWidth',2)
xlabel('Time (s)')
ylabel('Elongation (mm)')
%-------------------------------------------------------------------------

%DEFINE PARAMETERS AND CREATE INPUT
%-------------------------------------------------------------------------
close all
clc
% k1 = 9100;
% b1 = 3.3e6;
%
% k2 = 1e4;
% b2 = 1.5e6;
%
 dy = -0.18;

k = 9100;
b = 1.7e6;
%-------------------------------------------------------------------------


% CREATE TF AND SIMULATE RESPONSE
% -------------------------------------------------------------------------
s = tf('s');
%H = (b1*b2*s^2+(k1*b1+k2*b1+k1*b2)*s+k2*k1)/(b2*b1*k1*s^2+k2*k1*b1*s); %Kelvin + Maxwell Model
H = (b*s+k)/(k*b*s);
xo = X(tfitStart);
y = lsim(H,Ffit,tfit,xo);
subplot(2,1,1)
plot(tfit(1:(length(tfit)-3000)),Xfit(1:(length(tfit)-3000))+dy,'.','LineWidth',3)
hold on
plot(tfit(1:(length(tfit)-3000)),y(1:(length(tfit)-3000))*1000,'k','LineWidth',3)
xlabel('Time (s)');
ylabel('Displacement (mm)');
legend('Measured Displacement','Model Output')
subplot(2,1,2)
plot(tfit(1:(length(tfit)-3000)),Ffit(1:(length(tfit)-3000)),'k','LineWidth',3)
xlabel('Time (s)');
ylabel('Force (N)');
legend('Force Input')
% -------------------------------------------------------------------------
```

```
% % OPTIMIZE PARAMETERS FOR FIT
% % ------------------------------------------------------------------------
% close all
% clc
% s = tf('s');
% SSo = 500;
%
% dk1 = 100;
% db1 = 0.1e6;
% dk2 = 500;
% db2 = 0.1e6;
%
% b2 = 1.6e6;
% k2 = 20000;
%
% i = 1;
% for k1 = 50:dk1:5000
% for b1 = 1.5e6:db1:1.8e6
% %for k2 = 14000:dk2:22000
% %for b2 = 2e6:db2:4e6
%
% H = (b1*b2*s^2+(k1*b1+k2*b1+k1*b2)*s+k2*k1)/(b2*b1*k1*s^2+k2*k1*b1*s);
% xo = X(tfitStart);
% y  = lsim(H,Ffit,tfit,xo);
% SS(i) = norm((y*1000-Xfit).^2);
% if SS(i) < SSo
% k1opt = k1;
% b1opt = b1;
% k2opt = k2;
% b2opt = b2;
% end
% SSo = SS(i);
% i = i+1;
%
%
% end
% end
% %end
% %end
%
% k1
% b1
% k2
% b2
%
% s = tf('s');
% H = (b1*b2*s^2+(k1*b1+k2*b1+k1*b2)*s+k2*k1)/(b2*b1*k1*s^2+k2*k1*b1*s);
% xo = X(tfitStart);
% y = lsim(H,Ffit,tfit,xo);
% plot(tfit,y*1000,'k','LineWidth',3)
% hold on
% plot(tfit,Xfit-0.04,'-.','LineWidth',3)
% xlabel('Time (s)');
% ylabel('Displacement');
% legend('Predicted Displacement Using Measured Force','Measured Displacement')
% %------------------------------------------------------------------------
```

Appendix B
Selected LabVIEW Files

B1: Experimental Apparatus

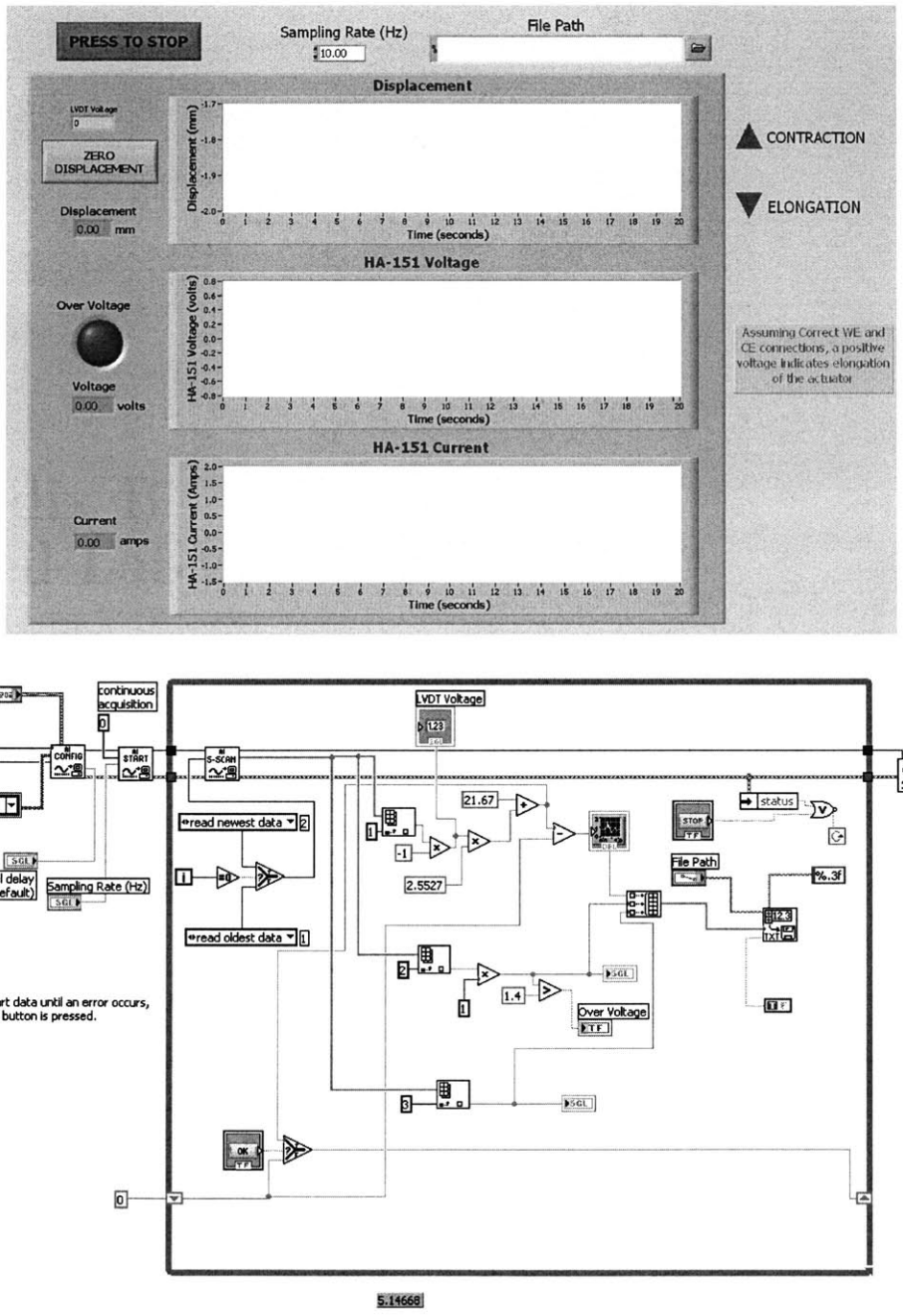

Figure B1: LabVIEW VI Used for Gathering Electrical Data and Displacement

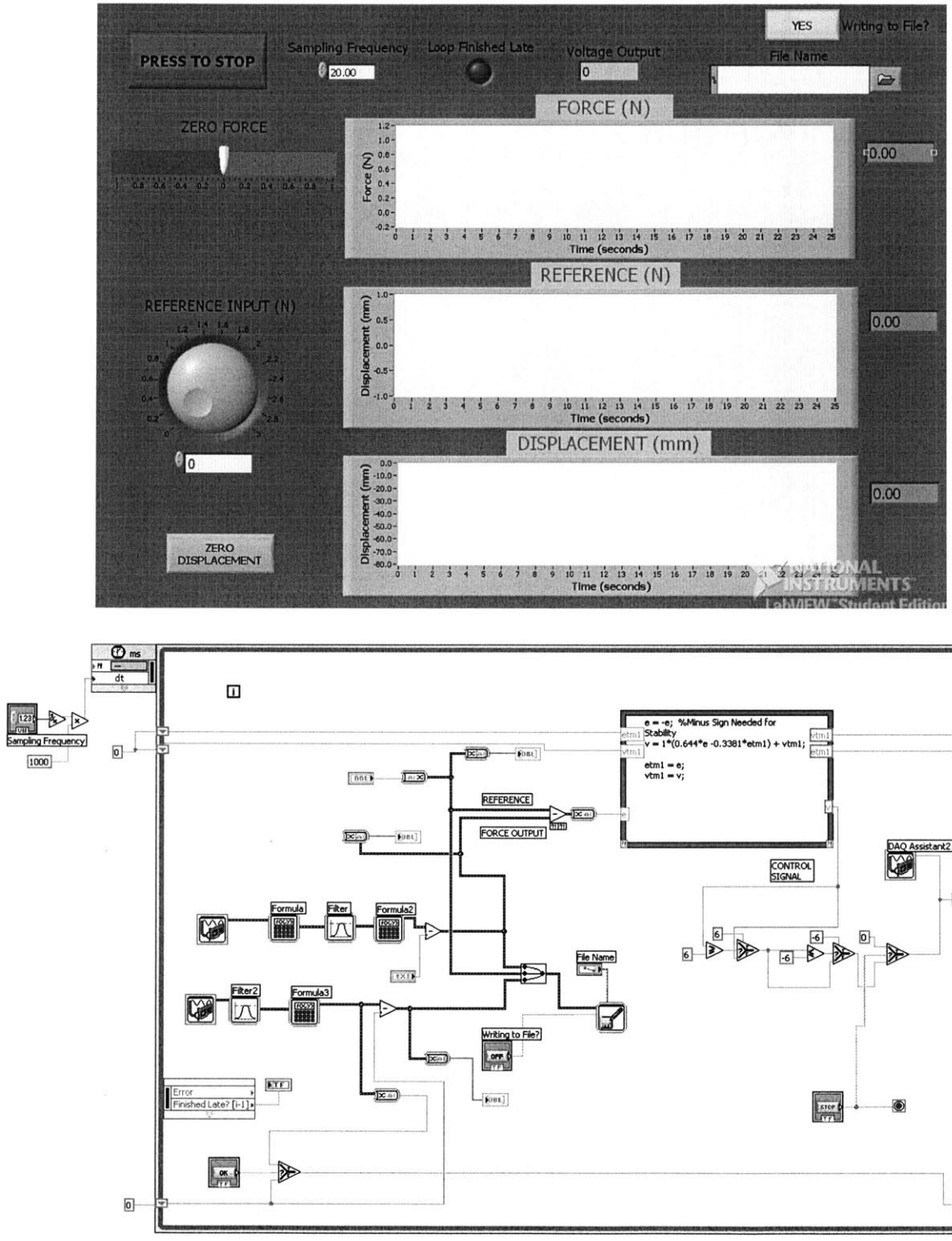

Figure B2: LabVIEW VI Used for Gathering Mechanical Data

B2: Monitoring and Preventing Actuator Degradation

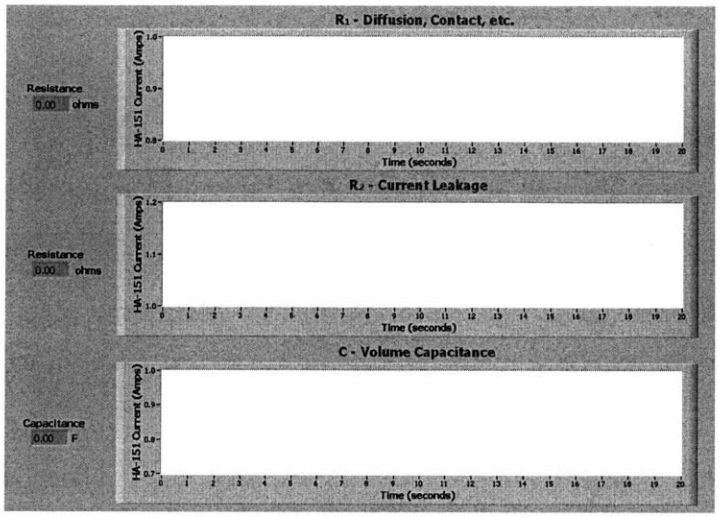

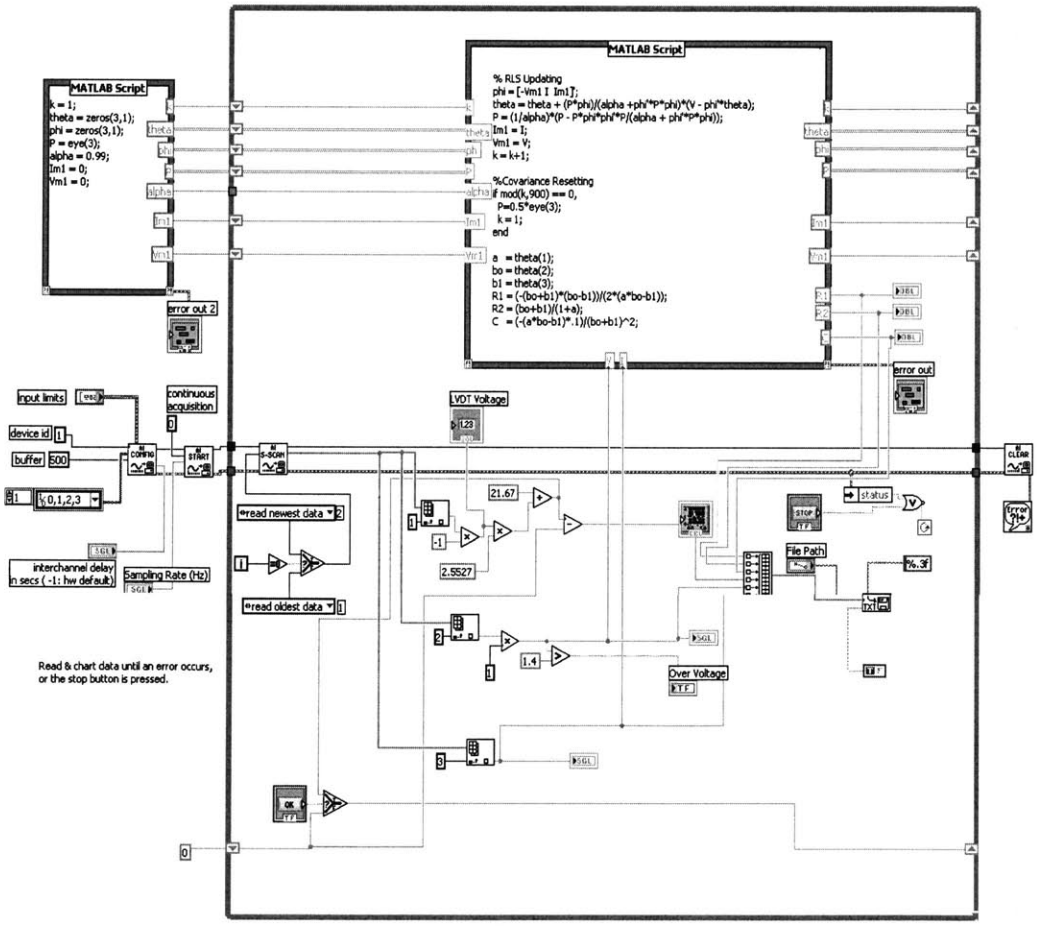

Figure B3: LabVIEW VI Used for Implementing RLS Algorithm

Appendix C
Human Foot Anatomy

C1: Skeletal Anatomy

This appendix summarizes the anatomy of the human foot relevant to Chapter 5. The content presented here is based on the references [1] and [2]. These references may be consulted for a more extensive treatment of human foot anatomy.

In total there are 26 bones in the foot. The basic bones are shown in Figure C1.

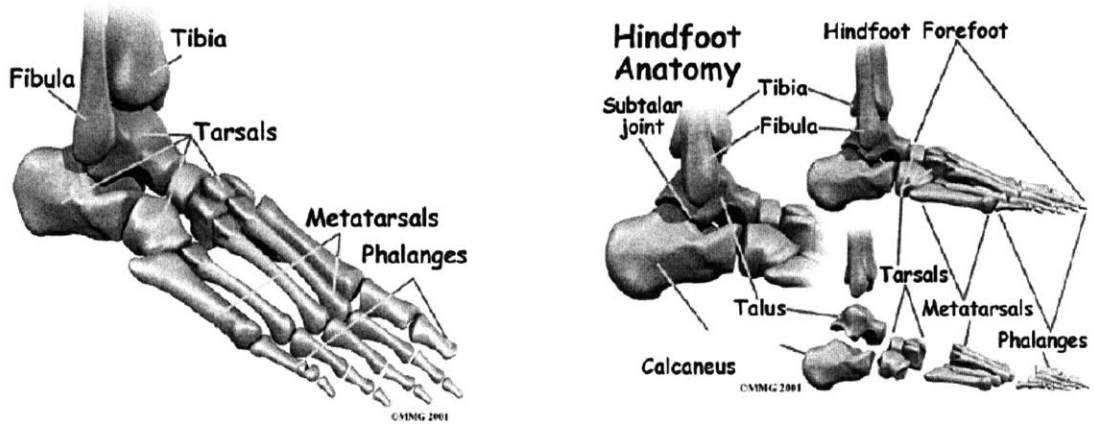

Figure C1: Bone Structure of the Human Foot [1]

There are three main groups of bones in the foot: *tarsals*, *metatarsals*, and *phalanges*. Of the 7 tarsals, the *calcaneous* and the *talus* are the most important. Several muscles of the calf attach to the calcaneus. The talus rests on top of the calcaneous, situated between the malleoli of the tibia and fibula. In its location, the talus receives the entire body weight and distributes it to the other tarsals. The remaining 5 tarsals not yet discussed are firmly connected to the metatarsals through the tarsal and metarsal joints.

The metatarsals and phalanges have a similar structure to their counterparts in the hand and they do not require extensive explanation. However, note that the metatarsal-phalangeal (MTP) joints form the ball of the foot, and movement of these joints is critical

for normal gait. Furthermore, the joint at the big toe (MTP_1 joint) is the most important for walking. Minimal relative motion occurs among the other joints of the phalanges.

The last elements of the skeletal anatomy are the three arches of the foot. Two arches run longitudinally from the metatarsals to the calcaneous and one arch runs transversely from across the bases of the metatasals. The arches are a critical element in the elastic energy storage properties of the foot.

C2: Muscular Anatomy

In this section, the anatomy of skeletal muscles, tendons and ligaments in the foot will be discussed. The muscle structure in the foot extensive; however, the important information is distilled and displayed in Figure C2.

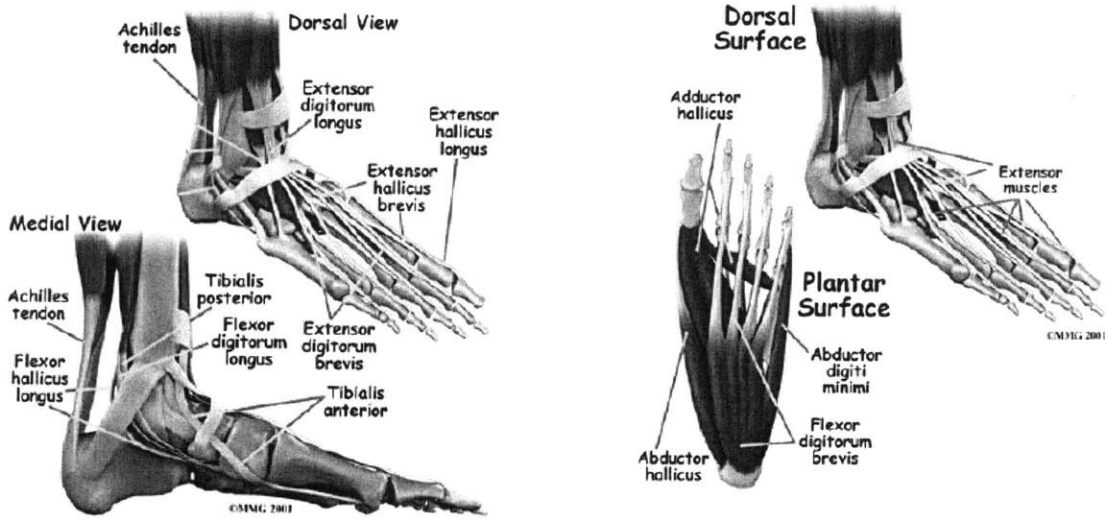

Figure C2: Muscles, Tendons, and Ligaments of the Human Foot [1]

Most muscles that act on the foot and toes are located in the leg. They are grouped into the anterior compartment (dorsiflex ankle and extend toes), posterior compartment (plantar flex foot and flex toes down), and lateral compartment (plantar flex and evert foot). The tendons associated with these muscle groups extend down into the foot and attach at various locations.

Some notable tendons are as follows. The Achilles tendon attaches to the calcaneus and is the most important tendon for walking, running, and jumping. The posterior tibial tendon attaches some smaller muscles in the calf to the underside of the foot and helps support the arch. Shortening of this tendon also helps turn the foot inward. There are tendons attached on the top of the toes that extend the toes and tendons attached on the bottom that bend the toes downward. Two tendons run behind the outer bump of the ankle (lateral malleolus) and attach to the outside edge of the foot. These tendons help turn the foot outward.

The foot also has intrinsic muscles. There is one muscle on the top of the foot that extends the first through fourth toes. There are four layers of muscles on the bottom of the foot. They act to move the toes outward and flex the toes downward.

C3: References

[1] http://www.allaboutmydoc.com/surgeonweb/surgeonId.2729/clinicId.1432/theme.theme3/country.US/language.en/page.article/docId.31167

[2] Spence A.P. *Basic Human Anatomy*, 3rd Ed., Redwood City, CA: Benjamin/Cummins, 1990.